Analysis of Flow Pattern in a Gasoline Particulate Filter using CFD

Ileana Magdalena Vega Mesquida

A thesis submitted in partial fulfillment of the requirements for the dregree of

Master of Science

in

Chemical Engineering

Chemical and Materials Engineering

University of Alberta

Abstract

The rise in motor vehicle ownership has become not only an environmental issue, but also a public health threat as pollutants emitted negatively affect human health (Deng et al., 2017). One such pollutant is particulate matter, which has been regulated by a variety of countries because it aggravates respiratory diseases such as chronic obstructive disease (Ling and van Eeden, 2009). Therefore, the automotive industry has implemented particulate filters in their products in an effort to capture these particles. This thesis analyzes flow characteristics within a representative element of a gasoline particulate filter that consists of one inlet channel, surrounded by outlet channels. The analysis considers a flow without particles that enters the inlet channel, crosses the porous walls and reaches the filter exit through outlet channels. The flow pattern is analyzed in two-dimensional and three-dimensional domains. To complete such analysis, computer fluid dynamics (ANSYS-Fluent) is applied using laminar, k-ε, k-ω and SST-transition models. Further, experimental data is compared with numerical pressure drop to determine which model best describes the flow pattern within a gasoline particulate filter. Additionally, the impact of including an inlet and outlet zone to quantify the effects of contraction and expansion is evaluated.

This work concludes the possible existence of turbulence in the channels of a gasoline particulate monolith. Although two-dimensional and three dimensional domains are solved using different parameters, both k-ε and SST-transition models prognosticate turbulence in the channels for Reynolds number above 220 in the channel. Nevertheless, the SST-transition model predicts turbulence at the end of the inlet channel in both domains, whereas the k-ε model only does so in 3D when the Reynolds number of the channel is equal to 2317. In contrast, the k-ω viscous model does not appear to describe flow pattern within the monolith. Moreover, the velocity profile is almost linear in 2D, whereas in 3D, the flow tends to cross

the porous wall at the end of the filter. Further, unlike the turbulent models, the laminar model demonstrates high dependency on inflow conditions.

The integration of an inlet and outlet zone increases the need for computer resources as well as increasing the difficulty in obtaining a converged solution. However, the modification of the domain does not significantly affect the numerical pressure drop. Finally, this investigation demonstrates that although the assumption of laminar flow is most accepted, it may not be the most accurate method of analyzing gasoline particulate filter. To the best of the author's knowledge, there are no known published works that have yielded the same conclusion.

Acknowledgements

First and foremost, I would like to express my gratitude to my supervisor Dr. Robert Hayes, for not only giving me the opportunity to be a part of this exciting project, but for also guiding and believing in me. The stories he shared with me, his recommendations, his explanations and his calmness were invaluable to my professional development. I would also like to give special thanks to my co-supervisor Dr. Petr Nikrityuk, who also aided me through the completion of my thesis, gave me advice and encouraged me to maintain my calm. To Martin Votsmeier for the professional discussions we engaged in and for having confidence in my work. To Kerry Chen for providing me valuable access to the experimental data, which greatly enhanced the results of my investigation.

I am grateful to Ivan Cornejo who was always available for every question I had. For his help, his patience and for the time spent repeating concepts until I comprehended the material. Most importantly, for his complete support when I was sad, frustrated, lost and happy. To Jonathan Nees for the time spent trying to understand my project in the hopes of helping me. To Constanza Sadino for her recommendations, help and the time we spent working together.

I sincerely appreciate the love and support of my family, who have believed in me from the beginning of my academic journey. To my mom for supporting me during frustrating moments and for always pushing me to do what makes me happy. To my dad, for encouraging me to keep studying and challenge myself. To my sister who has shown me the importance of not being afraid of anything. To my brother, who does not really say that much, but

was always there when I needed him. Lastly, to my husband, who spent hours reading my drafts, listening to my presentation rehearsals, learning what a gasoline particulate is and supporting me when I had problems and frustrations during this journey.

Finally, I would like to acknowledge the financial support from the Natural Science and Engineering Research Council of Canada, as well as the Dean of the Faculty of Engineering at the University of Alberta, Dr. Forbes. I would like to also acknowledge Compute Canada for allowing me to use their computational resources.

Contents

List of Figures

List of Tables

Nomenclature

Symbols

$\overline{U_i' U_j'}$	Reynolds stresses
$\vec{A}_f$	Surface area vector
$\vec{U}$	Velocity vector
F	Porous medium source term
k	kinetic energy
U	Flow velocity
U_c	inlet channel velocity
U_x	Axial velocity
V	Volume cell
1D	One-dimension
2D	Two-dimension
3D	Three-dimension
D	Diameter
k*	Dimensionless TKE

P Upstream node

P^* Dimensionless pressure

Re Reynolds number

S Source per unit volume

Greeks Symbols

α Permeability

Γ Diffusion coefficient

γ Intermittency

μ Viscosity

ω Specific dissipation rate

ϕ Scalar quantity

ρ density

ε Dissipation rate

Subscripts

E Upstream node

e Node e

f Face cell

P Downstream node

c channel

d domain

Other symbols

μ_t Eddy viscosity

N_{faces} Number of faces enclosing cell

$Re_{\theta t}$ Transition momentum thickness

Acronyms

ARTEMIS	Assessment and Reliability of Transport Emission Models and Inventory Systems
CDS	Central Difference Scheme
CFD	Computational Fluid Dynamics
COPD	Chronic Obstructive Pulmonary Disease
CPSI	Cells per square inch
DES	Detached Eddie Simulation
DOC	Diesel Oxidation Catalyst
DPF	Diesel Particulate Filter
FV	Finite Volume
FVM	Finite Volume Method
GDI	Gasoline Direct Injection
GPF	Gasoline Particulate Filter
IBM	Image Based Meshing
LCTM	Local Correlation based Transition Model
LES	Large Eddy Simulation
MUSCL	Monotone Upstream-Centered Schemes for Conservation Laws
NEDC	New European Driving Cycles
NPP	Normalized Plug Position
PF	Particulate Filter

PISO	Pressure Implicit with Splitting of Operators
PLS	Power Law
PM	Particulate Matter
PN	Particulate Number
PRESTO	PREssure STaggering Option
QUICK	Quadratic Upwind Interpolation for Convective Kinematics
RANS	Reynolds-Average-Navier-Stoke
SA	Simulated Annealing
SIMPLE	Semi-Implicit Method for Pressure-Linked Equations
SIMPLEC	SIMPLE-Consistent
SST	Shear Stress Transport
TKE	Turbulence Kinetic Energy
TVR	Turbulent Viscosity Ratio
TWC	Three Way Catalyst
WLTC	Worldwide harmonized Light vehicle Cycles

Introduction

Air pollution has consistently increased since the industrial revolution and has become a significant concern to public health. A leading contributor to this pollution are vehicles which emit various pollutants such as sulphur dioxide (SO_2), nitrogen oxides (NO_x) and particulate matter (PM) (Rao et al., 2012; Guarnieri and Balmes, 2014). PM are fine particles of varying sizes that accumulate differently when they are inhaled. For instance, PM with aerodynamic diameters between 2.5 to 10 μm deposit in large airways, while smaller PM particles sit in small airways and alveoli (Guarnieri and Balmes, 2014). This may cause, or intensify, respiratory diseases such as chronic obstructive disease (COPD), which is projected to be the third leading cause of mortality by 2020 (Ling and van Eeden, 2009). As a result, different countries have attempted to combat this issue by formulating increasingly stringent emission standards.

Car emission regulations led the automotive industry to research possible after-treatment technologies to reduce PM in fuel combustion, but the most promising so far are particulate filters. Experimental analysis of particulate filters provides a real scenario, but requires significant expenses in both time and equipment. Therefore, research is moving towards computer fluid dynamics, which facilitates the study of fluid parameters that are very difficult to observe otherwise. However, even though more powerful computers are available for researching this field, various uncertainties have yet to be solved. Yang et al. (2016) encourage the application of simulations to research particulate filters using few assumptions, therefore yielding results with higher accuracy and a deeper understanding of the interaction of con-

vection, diffusion and reaction in a particulate filter. One of the most important assumptions in the majority of publications is that the flow has a laminar behaviour. This holds true for fluids with a low Reynolds number and those flowing between solid walls without any other disturbances. However, in a particulate filter, the flow is in contact with porous walls so the flow regime may be altered (Beavers et al., 1970). In spite of extensive particulate filter research, there is still much contradiction among investigators in the field.

This thesis applies computer fluid dynamics to analyze flow behaviour within a gasoline particulate filter (GPF). The aim of this work is to demonstrate that although the assumption of laminar flow is most accepted, it may not be the most accurate method of analyzing GPF. This work is conducted to evaluate a particulate filter using a representative element of a GPF that to the best of the author's knowledge has not yet been attempted. This representative element consists of one inlet channel which is surrounded by outlet channels (Figure 1). The analysis uses flow without particles, while taking into account one-way coupling between the flow and particulates. Firstly, this thesis reviews previous particulate filter studies, and then proceeds into a two-dimensional domain flow analysis using different viscous models. This analysis is then repeated using a three-dimensional domain and is validated with experimental pressure drop data. Further, a geometry modification is attempted to analyze its impact on numerical static pressure drop.

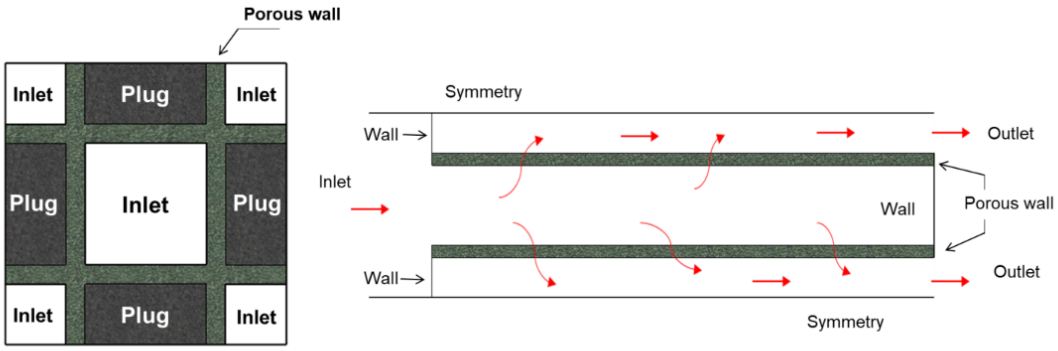

Figure 1: GPF domain utilize for this investigation.

Chapter 1

Literature review

The rise in motor vehicle ownership has become not only an environmental issue, but also a public health threat as pollutants emitted negatively affect human health (Deng et al., 2017). One such pollutant is particulate matter (PM), which is comprised of a complex physicochemical mixture of solid and volatile material. Studies have demonstrated the detrimental health effects that PM has on individuals who come into direct contact with it. Indeed, some organizations have concluded that these particles are most likely carcinogenic (Mamakos et al., 2011), and for this reason, many countries have implemented various regulations in the hopes of reducing PM emissions.

The first particulate emissions standards were established for diesel vehicles in 1992 and became more rigorous in 2005 (Euro 4 stage) (Mamakos et al., 2011). In 2009, the Euro 5 emission standard was put into effect for gasoline engines (Yang et al., 2016). Originally, the automotive regulations were limited to mass of PM, but were quickly shifted to particle number (PN) (Mamakos et al., 2011) as it accounts for smaller particles, which bears more significance on human health (Zinola et al., 2013). Further, this resulted in the introduction of a new standard in Europe called Euro 6, which restricts PN emission to 6×10^{11} per km by 2017 not only for diesel engines, but also for gasoline engines (Yang et al., 2016). These stringent regulations force auto manufactures to research and modify their reduction emission

technologies along with fuel efficiency.

PM is not an issue in pre-mixed combustion technology, however, fuel efficiency decreases due to the heat loss associated with this type of method (Arato and Takashima, 2015). Therefore, direct injection technology became prominent despite elevated levels of PM emissions. Within this technology, the use of either diesel or gasoline engines possess advantages and disadvantages. For instance, diesel engines provide better thermal and fuel efficiency than gasoline engines because they have a higher compression ratio. Alternatively, diesel engines produce higher particulate in mass distribution and NO_x emissions (Zhao et al., 1999; Yamamoto and Ohori, 2013) whereas gasoline engines release lower NO_x emissions but higher particulate in number distribution (Yang et al., 2016; Mamakos et al., 2013a; Karjalainen et al., 2014). Notwithstanding, recent studies show that gasoline direct injection (GDI) technology has the ability to improve fuel economy between 5% and 15% (Yang et al., 2016), providing higher thermal efficiency and more power output (Guan et al., 2015).

1.1 Gasoline direct injection (GDI)

An engine is a machine in which the chemical energy of a fuel is transformed into thermal energy, thus producing mechanical work. There are two types of engines: external combustion and internal combustion (Gupta, 2012), from which the latter is applied to motor vehicles (diesel and gasoline engines). In the GDI engine, pressurized fuel is injected into the combustion chamber via a common rail fuel line system and compressed gas and air ignite via a spark-plug (Yang et al., 2016). This mechanism is designed as either wall-guided, air-guided or spray-guided. In the first two designs, there is a long distance in between the injector and the spark-plug, whereas in the spray guided method, the arrangement between the injector and the spark-plug is closer, providing better response in between fuel preparation and ignition (Mamakos et al., 2011). Yang et al. (2016), mention that theoretically, spray-guided has the highest efficiency, albeit at the expense of higher level of PM and PN emissions.

Soot particulates are a result of the incomplete combustion of hydrocarbons. The amount of PM and PN released by different engines is based on their air-fuel ratio. In pre-mixed combustion technologies, the fuel is injected before entering the cylinder, allowing it to mix for a longer amount of time with air. In contrast, in a GDI engine, the fuel is directly injected in the cylinder, providing a limited time for the fuel and air to mix, thus causing poor mixture. Therefore, due to a rich mixture of fuel and air, the amount of PM emitted by pre-mixed combustion technologies are lower than GDI engines.

1.2 Particulate sizes in DPF and GPF

PM is a mixture of solid and condensed materials whose properties depend on the engine design, operating conditions, and type of fuel used. The sizes of PM can vary from nanometers to hundreds of nanometers depending on the fuel being combusted (Mamakos et al., 2011). As shown in Table 1.1 , PM is classified into five sizes of aerodynamic diameters. The nuclei mode is made of the smallest particles, which contributes considerably to the number distribution but very little to the mass distribution. Alternatively, larger particles in the accumulation mode significantly contribute to mass distribution rather than number distribution (Guan et al., 2015; Yang et al., 2016). According to Barone et al. (2012), in a diesel engine, the smaller particles are carbonaceous primary spheres while large particles are agglomerates. In GDI, it must be noted that a variety of studies have shown that exhaust gas presents ultra-fine and nano-particles which can be non-volatile or semi-volatile (Karjalainen et al., 2014).

Table 1.1: Classification of aerodynamic diameters.

Classification	**Particulate size**
Large particles	>10 μm
Coarse particles	2.5-10 μm
Fine particles	0.1-2.5μm
Ultra-fine-particles	50-100 nm
Nanoparticles	<50 nm

There has been much more research on diesel engines than on gasoline engines, yet the operation of these two technologies are very similar, and as a result, diesel studies are commonly applied to gasoline engines. For instance, to reduce particulate emissions in diesel engines, various combustion methods have been attempted but, until recently, the diesel particulate filter (DPF) has been the most promising technology in the reduction of particulate emissions due to its simplicity and effectiveness (Deng et al., 2017; Zinola et al., 2013). Therefore, it was possible to apply DPF to GDI, which later was called gasoline particulate filter (GPF).

Guan et al. (2015) as well as Mamakos et al. (2013b) affirm that the application of DPF in GDI technology becomes very effective in reducing PN. Although, since gasoline and diesel are different types of fuel, the PM generated might differ either in size or composition. Karjalainen et al. (2014) indicated that in a GDI, particles emitted during acceleration have mean mobility diameters around 10 nm and 70 nm, while during deceleration, emitted particles are smaller. In contrast, diesel particles usually behave similarly under the same driving conditions but with higher mean mobility diameters (larger particles) (Karjalainen et al., 2014). Therefore, the integration of DPF directly into GDI requires adjustment in the porous medium. Although, Kattouah et al. (2013) analyzed the adaptation of a GPF using new European driving cycles (NEDC) (at 25 °C and -7 °C), worldwide harmonized light vehicles cycles (WLTC), and common assessment and reliability of transport emission models and inventory systems (ARTEMIS) driving cycles up to 160 km/h (CADC160). The latter study confirmed that with the use of GPF, GDI technologies could meet Euro 6 standards at the expense of pressure drop efficiency. Consequently, to overcome pressure drop, GPF needs to be redesigned considering higher operating temperature particulate sizes, lower oxygen concentration and thermophoresis (Johnson and Joshi, 2018).

1.3 Particulate filter (PF)

Originally, car particulate emission regulations were applied to diesel exhaust gas, thus, the vehicle industry implemented PF as an aftertreatment technology in diesel engines to capture soot emitted. DPFs were constructed using fibrous filtration, but their efficiency reduced as PM adhered to the fibers. Therefore, researchers shifted their focus onto porous wall filters (Koltsakis et al., 2013). Hua et al. (2011) remark that DPFs are capable of removing anywhere from 50 to over 90 percent of PM from diesel exhaust gas. Furthermore, Guan et al. (2015) mention that this can be improved to 99 percent by using good mechanical and thermal durability.

A PF shares some similarities with a catalytic converter, which appears as a honeycomb shape with long channels. However, in a PF, alternate channels are blocked in the upstream and open in the downstream and vice versa. The fluid enters the square inlet channels flowing downstream, while some flow passes through the porous walls towards the adjacent outlet channels and hence, the fluid reaches the filter exit (Figure 1.1). The particulates are trapped in the porous walls which usually are made by ceramic, such as cordierite or silicon carbide (Di Sarli and Di Benedetto, 2015). Additionally, in the absence of any external energy source, the porous wall filtration efficiency relies on surface and volume diffusion, direct interception, and impaction (Zinola et al., 2013). As soot particles rise on the porous wall, a soot cake forms, which may improve filtration efficiency. Nevertheless, as the soot cake builds, so do the pressure drop and flow resistance. Thus, to avoid such effects, the filter is regenerated (Koltsakis et al., 2013).

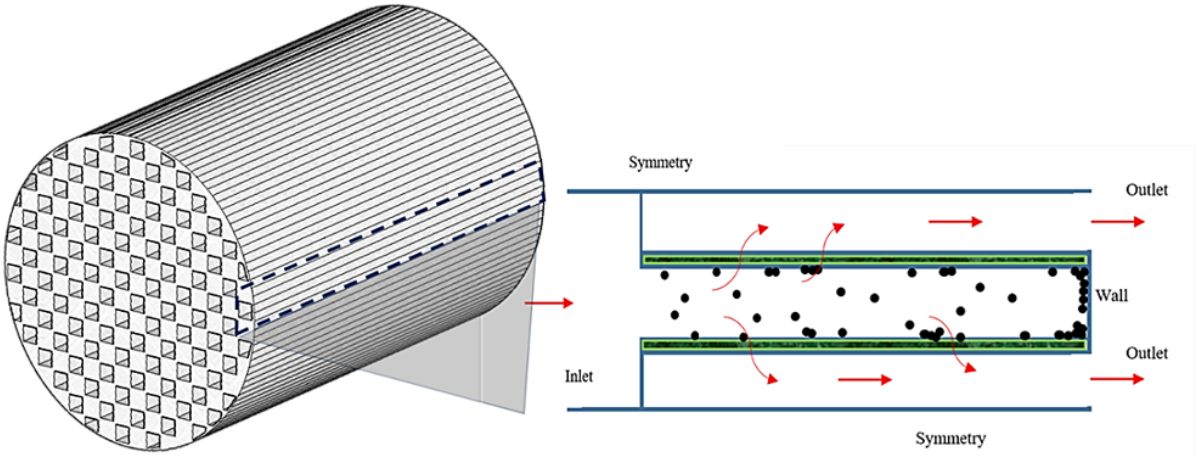

Figure 1.1: Automotive particulate filter and a close up on a particular channel.

Regeneration can be either active or passive. In active regeneration, the heat caused by the oxidation of post-injected fuel is used to burn soot in the filter. Whereas passive regeneration uses nitrogen dioxide as a soot oxidant. Furthermore, active regeneration occurs in long periods, since the requirement of energy is higher than that of passive regeneration (Acton, 2013). Active regeneration is used when a dense soot layer is present, and the temperature required for passive regeneration (250 °C) has not been reached (Koltsakis et al., 2013). Moreover, PFs are very likely to melt or crack if temperature gradients are not controlled (Guo and Zhang, 2006), and for this reason, regeneration becomes a challenge since soot loading is far from uniform (Koltsakis et al., 2013).

The activity of PM as exhaust passes through a DPF can be summarized in three stages. Firstly, the PM is captured on the porous wall by filtration. Secondly, regeneration occurs using either electric heating or fuel borne catalysts. Finally, ashes are rearranged within the DPF (Mokhri et al., 2012). To understand similarities in DPF and GPF application, Figure 1.2 illustrates the integration of a DPF and Figure 1.3 shows that of a GPF. As can be seen, a DPF is located after a diesel oxidation catalyst (DOC), while the GPF is positioned after a three-way catalyst (TWC). A DOC is a catalytic converter that usually contains platinum

(Pt) and palladium (Pd). These elements oxidize hydrocarbons (HC) and carbon monoxide (CO) (Guan et al., 2015). Similarly, the TWC contains Pt and rhodium (Rh) that reduce the nitrogen oxides (NO_x) to nitrogen (N_2) and oxidize CO and HC to carbon dioxide (CO_2) and water (H_2O) (Twigg, 2007; Alkemade and Schumann, 2006).

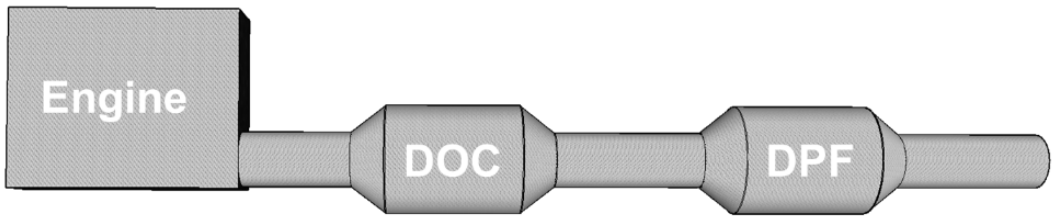

Figure 1.2: DPF location.

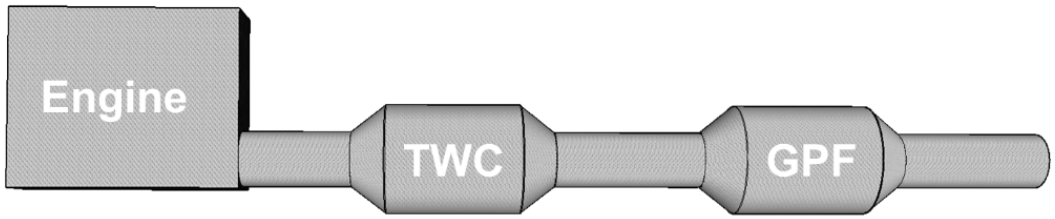

Figure 1.3: GPF location.

As previously mentioned, particulate filters are currently the most efficient technologies in the capture of PM. However, a major drawback is the pressure drop caused by particle loading and higher flow rates that negatively affects fuel consumption (Deuschle et al., 2008). Furthermore, one of the challenges in working with a GPF is that there is very little information about experimental and modeling studies on the dynamic filtration process. Therefore, the latter makes it difficult to understand microscopic and macroscopic filtration characteristics (Gong et al., 2017). Accordingly, further studies must be conducted to understand GPF flow dynamics and pressure drop. Lately, computational fluid dynamics (CFD) has been used to expand GPF knowledge by applying numerical solutions to understand the physics of fluids better.

1.4 Computational Fluid Dynamics (CFD) in DPF and GPF

The study of fluids using experimental approaches leads to a real scenario, however, it is more costly in terms of time consumption as well as materials and equipment used. CFD can be a powerful tool not only in the reduction of costs, but also in the illustration of physics within the fluids that would otherwise be very difficult to obtain experimentally. In fact, such a tool facilitates the access to sensitivity analysis on a variety of parameters that include fluid flows, heat transfer, as well as chemical reactions (Della Torre et al., 2015; Versteeg and Malalasekera, 2007). For this reason, the industry is moving towards a combination of CFD and experiments.

Automotive particulate filters are commonly studied, but soot loading and physical phenomena within porous walls have yet to overcome uncertainties. In an attempt to do so, Yang et al. (2016) suggest that further simulations could reduce assumptions and increase accuracy. Advanced computational tools are very helpful when examining different components of PFs, however, it can become very costly in terms of computer resources. Accordingly, PFs are analyzed on different scales: pore, porous wall, single channel, and monolith scale (Gong et al., 2017). Including all the scales in only one simulation increases not only costs, but also difficulty in problem solving, therefore, researchers focus on the study of PF scales separately.

1.4.1 Pore and porous wall scale

The primary goal of filtration walls is to enhance filtration without the expense of pressure drop. Porous wall simulations deal with extremely complex porous structures as a result of capturing very small particles. Therefore, computational resources are highly demanding in understanding soot deposition, cake formation, regeneration and ash rearrangement across and on the porous walls. To analyze porous media in CFD, the porous walls are

first constructed by different techniques of image based meshing (IBM) such as X-ray computed tomography (Micro-CT) and simulated annealing (SA), among others. For instance, Della Torre et al. (2015) used Mirco-CT to reconstruct three different porous substrates (A1 foam, SiC foam and cordierite) with different porosities and pore densities (95 % and 45 ppi, 87 % and 10 ppi, 50 % and 16 μm pore size), while Konstandopoulos et al. (2012) applied microflow simulation techniques to reconstruct porous walls (granular, foam, fibrous, cordierite, sintered metal and acicular). Moreover, the analysis of fluid dynamics, soot trajectories as well as heat transfer through these porous substrates is approximated by using different CFD approaches.

Finite volume method (FVM) is an approach that Della Torre et al. (2015) applied to understand fluid dynamics and heat transfer through the porous medium. The laminar and the low-Re k-ω SST models were used and it was concluded that turbulence does not have a significant effect on pressure drop. Moreover, Della Torre et al. (2015) also demonstrated that pressure drop is affected by heat transfer, which depends on the materials porosity as well as the conductivity. Therefore, Della Torre et al. (2015) proved that the cordierite material mainly operates in Darcy regime, while SiC and A1 foams operate from Darcy to Darcy-Forchheimer.

Lee and Lee (2013) also utilized the FVM, but in this case, to analyze soot deposition. They divided the porous wall into ten slabs to demonstrate that porosity in the first few slabs decreases as soot is trapped, whereas the porosity of the remaining slabs keep the same initial porosity value. This is in agreement with Gong et al. (2017), who divided a homogeneous porous substrate in three slabs. Gong et al. (2017) expanded the study to a heterogeneous porous substrate using a unit cell method, and ascertained that in a heterogeneous porous substrate the particulates tend to penetrate further affecting soot cake formation and pressure drop.

Moreover, pressure drop due to soot cake build up was explored by Yamamoto and Ohori (2013) using another CFD approach, called lattice Boltzmann method. They modelled one

small portion of a PF in three-dimensions and the domain consisted of three sections; the porous substrate, an inlet section, and an outlet section where no porous material was involved. Yamamoto and Ohori (2013) observed three soot stages in which soot deposits inside the pores, pore bridging and soot layer formation. During these stages, the pressure initially increases slightly, followed by a more abrupt increase. Although, Matte-Deschênes et al. (2016) determined that soot layer not only affects pressure drop, but also the regeneration process. They studied particle capture in a cordierite porous wall and observed that the soot deposition is significantly affected by the thermophoresis, and thereby the regeneration process.

In a GDI engine, high exhaust gas temperatures lead to a continuous regeneration, producing small soot particulates (Zinola et al., 2013). This is an issue when DPF is used without any modifications into a GDI engine due to bigger particulates emitted by diesel engines. Ultrafine particles coming from GDI exhaust gas affects soot cake formation, and therefore filtration efficiency. Zinola et al. (2013) implemented a GPF with a membrane to avoid ultrafine particles penetrating the porous medium. However, while this membrane improved filtration efficiency, it came at the expense of higher back pressure than in a GPF without a membrane. Therefore, other alternatives should be explored to improve filtration efficiency along with reducing pressure drop in a GPF.

1.4.2 Channel scale

Assuming inflow conditions are radially homogenous, an entire monolith can be extrapolated by choosing only two representative channels (Konstandopoulos et al., 2005, 2006). To further simplify the computational burden, these two representative channels can be modelled in two-dimensions (2D). For instance, when Di Sarli and Di Benedetto (2015) analyzed soot combustion in a 2D catalyzed DPF using the FVM, the model equations were discretized applying a uniform grid with 219,600 squared cells. They noticed that when using a catalyst, upper limit temperatures avoided fast regeneration. Furthermore, Deuschle et al. (2008)

studied filtration and regeneration effects without a catalytic wall using 2D geometry with rectangular elements. In this study, the Eulerian-Lagrangian approach coupled with user defined subroutines was utilized. They noticed that as temperature increases during regeneration, so does the pressure drop. On the other hand, Piscaglia et al. (2005) analyzed the velocity profile along both the inlet and outlet channels, as well as in the porous wall. To extend the investigation, they proposed including the Lagrangian approach to the KIVA-3V code to examine soot deposition. Piscaglia et al. (2005) concluded that soot deposition depends on the inlet velocity, permeability, and geometry of wall, in fact, they determined that the velocity in the porous medium is close to uniform for lower permeability.

Bensaid et al. (2009), unlike Piscaglia et al. (2005) and Deuschle et al. (2008), mention that to understand soot cake formation and regeneration, the Lagrangian approach is not easily applicable and uses more computer resources. For this reason, Bensaid et al. (2009) apply the Eulerian-Eulerian approach using a three-dimensional (3D) domain consisting in one inlet and one outlet channel (Figure 1.4). Bensaid et al. (2009) ascertain that inertial effects are neglected for particles smaller than 500 nm and that filtration efficiency increases as a soot layer is formed on the porous wall. Further, Bensaid et al. (2009) observed that initially, particles stick closer to the inlet as well as at the end section of the inlet channel. This is in contrast to Sbrizzai et al. (2005), who demonstrated that all particles follow the flow field and stick at the end section of the inlet channel. Regardless, Sbrizzai et al. (2005) utilized the Lagrangian approach.

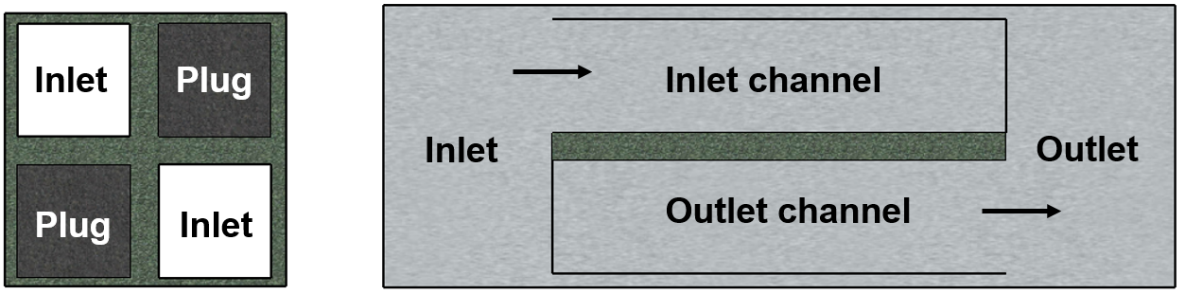

Figure 1.4: Four channels domain for CFD simulations to study a PF.

Lee and Lee (2013) also investigated the soot filtration in a 3D geometry using the domain as shown in Figure 1.5. Lee and Lee (2013) utilized the Eulerian-Eulerian approach and noticed, as opposed to Bensaid et al. (2009) and Sbrizzai et al. (2005), that the particle build-up is initially close to the inlet and later moves to the end part of the inlet channel. The particle build up mainly affects pressure drop within the monolith, however, if build up occurs in the inlet section, the pressure drop will present itself in the form of contraction losses. Konstandopoulos et al. (2001) examined contraction and expansion losses by including an extra section in the upstream and downstream. The problem was simulated using the FVM and a grid consisting of 145,443 hexahedral cells. This simulation predicted a smooth contraction and a wake in the expansion. In addition, it was observed that the higher the flow rate, the higher the inertial losses. Nonetheless, Konstandopoulos et al. (2001) demonstrated that contraction and expansion losses have the least impact over the total pressure drop along the filter, but they mention that contraction losses increase in accordance to the plug size. Furthermore, Lee and Lee (2013) investigated the plug location in the outlet channel to improve pressure drop along the filter. They applied a CFD code with user defined field functions to a polyhedral meshing with 784,957 cells. The channel plugs where located at 0.25 normalized plug position (NPP), 0.50 NPP and 0.75 NPP of the outlet channel. Lee and Lee (2013) concluded that during the main stage of filtration, 0.50 NPP position resulted in less pressure drop.

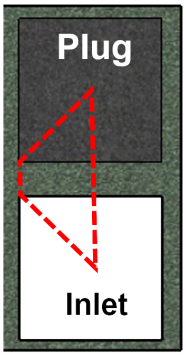

Figure 1.5: Triangle domain for CFD simulations to study a PF.

The aforementioned articles assumed laminar flow, however, Deng et al. (2017) studied continuous regeneration in 3D geometry (Figure 1.4) using the turbulence model k-ε-zeta-f and user defined subroutines. Deng et al. (2017) determined that as wall thickness increases, so does pressure drop. In addition, Deng et al. (2017) determined that pressure drop also increases as the filter diameter decreases and that the regeneration process improves as the channel diameter increases. This article utilized a turbulence model despite the fact that the majority of papers use a laminar approximation due to low Reynolds number in channels. Nevertheless, Konstandopoulos et al. (2001) specify that at higher inlet velocities, the simulations started becoming more unstable. Therefore, a further investigation in flow behaviour would increase credibility in CFD simulations to study automotive PFs.

1.4.3 Monolith scale

The use of two single channels to represent the entire monolith is an excellent simplification that helps increase filtration efficiency. Nevertheless, using a conic surface attached to a PF, Bensaid et al. (2009) demonstrated through experiments that cake formation differs in every monolith channel. The discrepancy was a result of non-uniform flow distribution that yielded unequal channel velocities. Zhang et al. (2005) modelled the upstream and downstream flow distribution and used the FVM and the standard k-ε turbulence model with standard wall function to solve the problem. Further, Zhang et al. (2005) concluded that maldistribution relies on inlet pipe geometry, for instance, the higher the inlet pipe length, the higher the flow uniformity. Moreover, Zhang et al. (2005) noticed that the inlet pipe angle might be beneficial in terms of flow uniformity, however, this depends on pipe length. Furthermore, Turner et al. (2011), utilizing the same numerical approach as Zhang et al. (2005) compared inflow distribution results with particle image velocimetry. They noticed some recirculation in the corners that Konstandopoulos et al. (2001) did not in a channel scale.

Modelling an entire monolith requires high amount of computational resources. For this reason, modelling the monolith as a continuum is a promising alternative to predicting flow

distribution, regeneration, and temperature gradients, among other aspects in a PF (Konstandopoulos et al., 2006). For instance, Zhang et al. (2005) modelled the monolith as a porous substrate and enforced laminar flow therein. Furthermore, Konstandopoulos et al. (2005) built a continuum that retained relevant microstructure to describe soot mass profile in the monolith. The problem was performed in a CFD simulation based on the FVM with some subroutines. Konstandopoulos et al. (2005) used a bent 45 degree inlet pipe and noticed that the face velocity leans to a homogeneous distribution, whereas the soot distribution does not. Further research into soot deposition is important not only because of the effect on pressure drop, but also because particulate loading results in higher temperature gradients making it more susceptible to melt or crack (Guo and Zhang, 2006).

Chapter 2

Flow pattern in a representative element of a GPF in 2D

Exhaust gas is comprised of particles made of a mixture of elemental carbon and volatile organic compounds (Johnson and Joshi, 2018). These particles are trapped using after treatment technology because of the damage to human health. Until now, particulate filters (PF) are the most promising technology in the efficient removal of particles. In modelling, most publications assume laminar motion within the channels of a PF according to low Reynolds number (Re), however, as exhaust flow rate increases so does flow instability. With typical Re before and after a monolith (about 10^4), Cornejo et al. (2018a) showed the presence of small eddies inside the channels of an automotive catalytic converter which decay as the flow moves forward. A PF, unlike a converter monolith, has alternate closed channels in the upstream and open channels in the downstream and vice versa. Moreover, in a PF the channels are surrounded by a porous medium that affects velocity profile since the velocity at the boundary with the porous medium is non-zero (Beavers and Joseph, 1967). This slip velocity affected by the flowrate also changes depending on channel height (Beavers et al., 1974). Carotenuto and Minale (2011) studied the interface between a fluid and a porous medium using a non-slip approach. They noticed that the rougher the porous medium, the

higher the interfacial velocity and the shear rate. Similarly, Wang and Wang (2007) demonstrated that in microchannels with rough walls, the velocity profile deviates from that of Posieuille flow closer to walls. Wang and Wang (2007) also mention that as wall roughness increases, so do disturbances. Furthermore, Beavers et al. (1970) confirm that when flow is in contact with a porous medium, the flow regime between laminar and transition breaks at lower transition Re. Therefore, despite the fact that Re within PF channels are low, there is a chance that laminar flow becomes transitional flow. Moreover, with a Péclet number in the order of 10^4 (for particles with a diameter greater than 5 nm and fluid velocities higher than 0.1 m/s) convective transport dominates the soot trajectory. Accordingly, formed eddies can change soot trajectory affecting soot deposition that influences not only the velocity inside the channels, (Piscaglia et al., 2005) but also the temperature, which could result in a melted filter (Yu et al., 2013).

The inlet pipe geometry of a PF modifies the gas velocity approaching the monolith; however, as flowrate increases so does soot deposition in channels placed in the centre of the monolith (Ranalli et al., 2002). Bensaid et al. (2009) demonstrates that at the same axial location, the centre of the monolith contains soot cake almost twice as thick as the lateral channels. This statement agrees with Ranalli et al. (2002) who mentions that higher temperatures appears in centre of the monolith due to soot loading. For this reason, assuming radially homogeneous entrance into a PF could lead to inaccurate results, mostly affecting thermal stresses within the monolith. Nevertheless, considering modelling thousands of channels will increase the cost significantly (Oxarango et al., 2003). To simplify some difficulty in modelling, Haralampous et al. (2003) proposed a two dimensional multichannel model to study regeneration when all channels in the monolith have the same behaviour. Nonetheless, to reduce further the use of computational resources to calculate loading, regeneration and rearrangement effects, various studies assume homogeneous inlet flow and examine two characteristic channels (inlet and outlet) (Deuschle et al., 2008; Konstandopoulos et al., 2005) modelling them in different dimensions.

2.1 Turbulent models

Turbulence is a complicated phenomenon that has been studied throughout several decades and yet laborious mathematical approximations are still far from accurate (Wilcox, 2006). Currently, there are three different approaches to predict turbulent flow: statistical, deterministic and structural. The statistical approach assumes that turbulence is a random phenomenon while in the deterministic approach, turbulence is considered chaotic and random. The structural approach describes turbulence as a coherent structure flow, however, this approach is considered weak in theory. Furthermore, there are two more methods, which solve the dynamics of large eddies and model small-scale eddies: Large Eddy Simulation (LES), and Detached Eddy Simulation (DES) (Tabatabaian, 2015). The LES employs subgrid-scale models assuming that small eddies are separated from large eddies while DES solves turbulent flow using LES in fully turbulent region and Reynolds average Navier-Stokes (RANS) models near the wall region (Feng et al., 2014).

Within the statistical approach, RANS models are currently the most practical in terms of computational cost (Tabatabaian, 2015). RANS models cover the time-average equations that describe fluid motion within the domain and calculate the eddy-viscosity to compute the Reynolds stresses (Ansys, 2017). These models emerged at the end of the nineteenth century, and since then, one-equation, two-equation and stress-transport models have been developed. Kolmogorov established the first complete turbulence model (k-ω model) and added the term ω, which stands for specific rate of dissipation of energy. Afterwards, Launder and Spalding elaborated the model k-ε, known as the mixing length model (Wilcox, 2006). This last model has been widely used since it obtains robust, economical and reasonable results for many engineering flows (Feng et al., 2014). Then, Menter devised a new version of the k-ω model, which accounts for the transport of the shear stresses in adverse pressure gradient boundary layers. This model was originally called the SST model (Menter, 1993), but later took the name SST k-ω. The latter incorporates both, k-ε and k-ω models to overcome their weaknesses (Ansys, 2017). Nevertheless, it is complicated for RANS models to predict

transitional flow because transitional flows are composed of linear and non-linear effects and RANS models eliminates linear disturbance growth (Menter et al., 2006a).

When the laminar flow undergoes an adverse pressure gradient, free stream turbulence or rough walls (amongst others), the flow can pass from laminar to transition regime. The latter is a phenomenon that occurs in different engineering applications and goes through different paths: bypass transition, natural transition, separated flow transition, wake induced transition and reverse transition. Bypass transition is the first three stages of natural transition, which occurs at high Re and low freestream turbulence. In the separated flow transition, the flow captures an adverse pressure gradient with very little disturbance (Genc et al., 2012). To overcome these flow paths, local correlation based transition model (LCTM) was developed (Menter et al., 2015).

Menter et al. (2006a) specifies that transitional models need to include stability analysis, correlation based models and low Re models. Based on the latter, Menter et al. (2006a) devised the LCTM, which is a combination of empirical correlations with two transport equations. This model was coupled with the SST k-ω turbulence model, extending to one equation for intermittency and one for transition onset correlation ($\mathrm{Re}_{\theta t}$). In the intermittency equation, the production term of the turbulence energy downstream of the transition point in the boundary layer was activated whereas the $\mathrm{Re}_{\theta t}$ captured the non-local turbulence intensity. These two equations together result in the SST model and cover transition caused by free stream turbulence intensity, pressure gradients and separation. A decade later, Menter et al. (2015) improved this model by reducing it to one equation (intermittency), expanding its application to more flow disturbances. Unfortunately, this model is still not available in the software ANSYS-Fluent 17.2 version.

2.2 Numerical methods

Fluid dynamics is governed by conservation of mass, momentum and energy equations. These equations do not have an analytical solution in most of the engineering problems; fortunately, numerical methods approach can overcome this issue (Ferziger and Peric, 2012). Numerical methods provide approximate answers at discrete points within the domain, which are referred to as grid points. To obtain numerical solution, the domain is discretized either in an integral or differential form. The latter is widely used in CFD, however, ANSYS-Fluent (software used in this work) uses the integral form and for this reason, this section will focus on finite volume method (FVM) (Anderson et al., 2013).

The integral formulation of conservation is the basis of FVM. This method is the simplest to understand and to implement. Nevertheless, when it comes to higher than second order accuracy, the solution is more difficult to obtain because of the interpolation, differentiation and integration carried out. FVM is a direct method in which the domain is divided into finite volumes enclosing grid points. Structure and unstructured grids are applicable in FVM to fix grid points in the geometry. The structure grid is very simple; it has four neighbours in two dimensions and six in three dimensions. The drawback about this grid is that it only applies to geometries with simple domains. In contrast, the unstructured grid is applicable for complex domains; however, it requires more computer resources. Such grids contain cells, which can be tetrahedral, hexahedral, triangles, or rectangles that contain nodes. The partial equations are applied to determine the variables at these nodes and therefore, the higher the nodes the higher the accuracy at the expense of computational cost (Anderson et al., 2013; Ferziger and Peric, 2012).

In numerical solutions, there are three different errors called modelling, discretization and iteration. The modelling error refers to the difference between the flow and the exact solution of the mathematical error (turbulence model's error tends to be high). In the case of discretization, the error focuses on the difference between the exact solution of the conservation equations and the exact solution of the algebraic system (finer grid will reduce

this error). Finally, the iteration or convergence error is based on the difference between the iterative solution and the algebraic equations system (solution converges when this error is very small) (Ferziger and Peric, 2012), which are originated by the discretization process.

To approximate linear system of algebraic equations, different techniques are used based on the equation's type: linear or non-linear. For instance, in the non-linear case, an iterative technique is applied that guess a solution and linearize the equations involved (Ferziger and Peric, 2012). A few examples of these iterative techniques include, Jacobi, Gauss-Seidel and successive-over-relaxation (Hoffman and Frankel, 2001). ANSYS-Fluent software uses the Gauss-Seidel method to resolve the algebraic equations generated with a sparse matrix. Gauss-Seidel requires diagonal dominance for convergence and uses the most recent values in all computations (Hoffman and Frankel, 2001).

Furthermore, ANSYS-Fluent uses two strategies to solve mass conservation equations: pressure-based solver and density-based solver. Both methods calculate the velocity field by using momentum equations, however, the density-based solver obtains the density using the continuity equation and the equation of state to predict the pressure. In contrast, the pressure-based solver uses both continuity and momentum equations to compute pressure. This procedure is achieved by coupling pressure-velocity utilizing different schemes. ANSYS-Fluent selects SIMPLE as default; however, SIMPLEC improves convergence in cases with high mesh skewness by changing the value of the relaxation factor. Moreover, PISO scheme usually is applied to transient calculations and geometries with high degree of mesh distortion. For computing the velocity and pressure, PISO offers a higher efficiency over SIMPLE and SIMPLEC by adding a neighbour and skewness correction. In addition, by applying the coupled algorithm, steady state flows get a more robust and efficient single face implementation. Therefore, this algorithm provides good performance for transient flows with poor mesh (Ansys, 2017).

The software ANSYS-Fluent uses the integral form of conservation law (Eq. 2.1) discretized as shown in Eq. 2.2 (the definitions of the parameters in Equations 2.1 and 2.2

are defined in Ansys (2017)). This latter equation is applied to every control volume and the scalar ϕ_f is interpolated. The second term on the left of the equation is the convection while the first term on the right is the diffusion. The diffusive term is approximated using central difference scheme (CDS), while the convective term uses upwind scheme. The CDS estimates the value of ϕ at cell "e" (Figure 2.1) using linear interpolation (Eq. 2.3), while the upwind scheme uses the upstream node of "e" to interpolate depending on the direction of the flow. This last scheme will never undergo to oscillatory solutions because it satisfies the boundedness criterion (Ferziger and Peric, 2012).

$$\int_V \frac{\partial \rho\phi}{\partial \mathrm{t}} \mathrm{d}V + \oint \rho\phi\vec{U} \cdot \mathrm{d}\vec{A} = \oint \Gamma_\phi \nabla\phi \cdot \mathrm{d}\vec{A} + \int_V \mathrm{S}_\phi \mathrm{d}V \tag{2.1}$$

$$\frac{\partial \rho\phi V}{\partial t} + \sum_f^{N_{faces}} \rho_f \phi_f \vec{U_f} \vec{A_f} = \sum_f^{N_f} \Gamma_\phi \nabla\phi_f \vec{A_f} + S_\phi V \tag{2.2}$$

$$\phi_e = \frac{1}{2}(\phi_E + \phi_P) \tag{2.3}$$

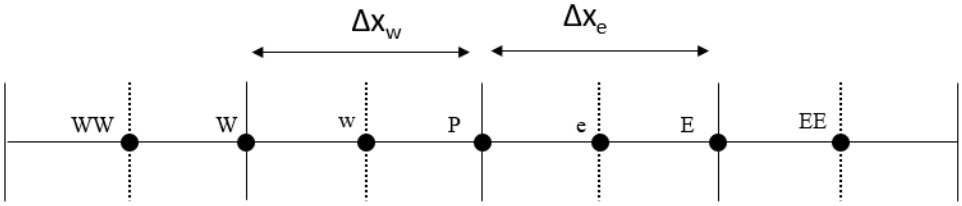

Figure 2.1: Cartesian grid for upwind scheme.

Different upwind schemes are offered by ANSYS-Fluent software like first order upwind, second order upwind, power law (PLS), quadratic upwind interpolation for convective kinematics (QUICK) and the third order monotone upstream-centered schemes for conservation laws (MUSCL), among others. The first order upwind uses only one upstream point while the second order uses two. Between these two schemes, the second order upwind has higher accu-

racy, however, it can produce unbounded solutions and takes longer to converge (Ferziger and Peric, 2012). The QUICK scheme has higher order of accuracy than the last two schemes since it makes the numerical diffusion negligible by using three upstream points. QUICK scheme is more accurate on structured meshes, whereas the third order MUSCL in unstructured meshes by bringing the CDS and second order upwind scheme together and reducing numerical diffusion significantly. Finally, the PLS is not an expensive scheme in terms of computational sources. It interpolates the face value of ϕ by balancing convection and diffusion in the direction of the stream (Ansys, 2017), nonetheless, this is a first order scheme.

Furthermore, for computing secondary diffusion terms, scalar and velocity gradients, ANSYS-Fluent uses three different approaches: Green-Gauss cell based, Green-Gauss node based and least squared cell based. The Green-Gauss theorem in general approximates the gradient of a scalar by the surface integral of the product of the scalar with a unit normal vector over some control volume. This theorem was discretized from the finite-element method (Blazek, 2015). In the Green-Gauss cell based, the arithmetic average was approximated using the values of the neighboring cell centres whereas the Green-Gauss node based uses the nodal values on the face. This last approach provides higher accuracy (second order) and works better for mixed or unstructured meshes (Ansys, 2017). Furthermore, the least squared approach uses the first order Taylor series for each centre point cell around the evaluation point (Blazek, 2015). This approach has first order accuracy and is suitable for mixed grids. Its accuracy is similar to Green-Gauss node based; however, least-squared approach has lower computational costs (Ansys, 2017).

Additionally, the aforementioned discretization schemes cannot approximate the pressure gradient since the pressure field is not priori known. ANSYS-Fluent uses a formulation to calculate this term by interpolating the pressure value. This interpolation is computed by different approaches. The standard schemes is the default selection by the software and applies for problems where pressure variation between cells is smooth. For other types of problems such as, the linear, the second order, the body force weighted and the pressure

staggering option (PRESTO), schemes can be chosen. In the linear scheme, the face pressure is calculated by averaging the pressure values of the adjacent cells. The second order scheme has some improvements over the standard and linear scheme, although, having a low quality mesh might affect convergence. Ansys (2017) mentions that for systems with a porous medium involved, this scheme is not applicable. Furthermore, the body force weighted scheme assumes that the normal gradient of the difference between pressure and body forces is constant. In addition, the PRESTO scheme is recommended for use with flows containing high swirl and Rayleigh number, high speed rotating flows, flows involving porous media and strongly curved domains (Ansys, 2017).

2.3 Description of domain

This study applies a numerical analysis by investigating velocity profile and turbulence in a representative element of a GPF in two-dimensions (2D). This representative element assumes that the flow across the monolith face is evenly distributed and includes one inlet channel, surrounded by outlet channels. The inlet channel measures 154.4 mm $\times$ 1.3 mm $\times$ 1.3 mm and contains a plug at the end section whereas, in the outlet channel, the plug is situated on the upstream face. Including the channels surrounding the inlet channel gives the final domain measurements as shown in Figure 2.2. The total size of the inlet domain is 2.94 mm square and the porous medium wall has a thickness of 0.17 mm. The analysis adopts a flow without particles that enters the inlet channel, crosses the porous walls and reaches the filter exit through outlet channels.

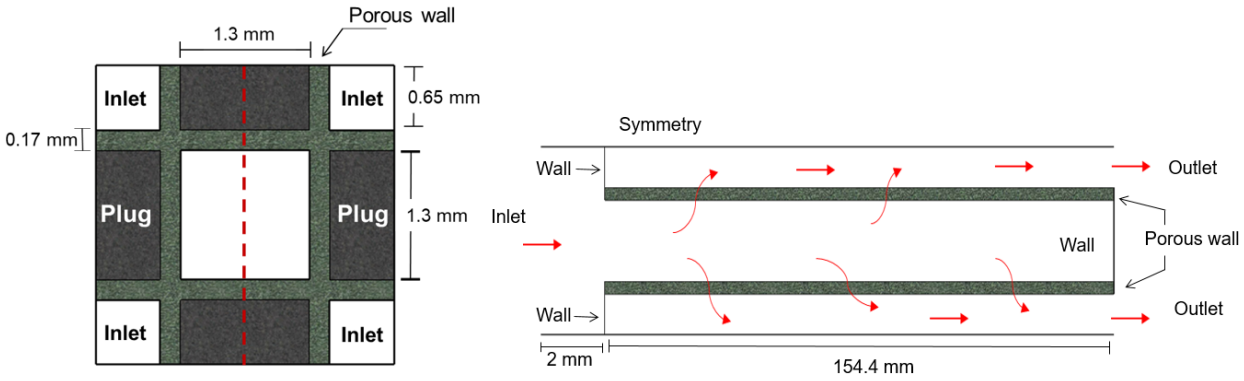

Figure 2.2: 2D schematic utilized to model a representative element of a wall particulate filter channel.

2.4 Numerical solution

This system performed steady state simulations using the computational fluid dynamics (CFD) software, ANSYS-Fluent. Different viscous models such as laminar, k-ε, k-ω and SST-transition models were use to analyze the flow pattern in a GPF (Table 2.1). The discretization and specifications of the previously mentioned viscous models are given in Tables 2.2 and 2.3. The convergence criterion was to reach a value for the scaled residuals in the order of 10^{-6} for the transport variables as well as having a stable value for the volume average of turbulent kinetic energy (TKE), turbulent viscosity ratio (TVR) and mean velocity.

Table 2.1: Viscous models specifications.

Viscous model	**Specifications**
Laminar	Governed by the Navier-Stokes equations (Ansys, 2017)
	Flow is laminar (for pipe flow: Re $<$ 1000) (Ansys, 2017)
	Energy transfer is accomplished by molecular interaction (Ansys, 2017)
k–ε	Is suitable for fully turbulent flows (Tabatabaian, 2015)
	The drawback for this model is the low accuracy for systems that present adverse pressure gradients and boundary layer separation (Ansys, 2017)
	Depends on near-wall functions (Lodefier et al., 2003)
	Not able to capture turbulent boundary layer up to separation (Menter et al., 2003)
k–ω	This model solves the shortcoming from k-ε model; applicable for separated flows, jet flow, and flows with adverse pressure gradient analysis (Tabatabaian, 2015)
	Good for predicting near-wall region (Menter et al., 2003)
	Fails for pressure induce separation (Menter et al., 2003)
	Strongly depend on free stream values (Menter, 1993)
SST-transition	Accuracy of this model increases for near-wall and free stream systems (Tabatabaian, 2015)
	Accounts for transition (Menter et al., 2006a)
	Separation induced transition
	Free stream turbulence
	Pressure gradients
	Not effective in predicting cross flow

Table 2.2: Discretization of viscous models used in 2D domain.

Discretization	**Laminar**	**k − ε**	**k − ω**	**SST-transition**
Scheme	Simple	Simple	Simple	Simple
Specific dissipation rate	N/A	N/A	QUICK*	QUICK*
Turbulent dissipation rate	N/A	QUICK	N/A	N/A
Turbulent kinetic energy	N/A	QUICK	QUICK	QUICK
Momentum	QUICK	QUICK	QUICK	QUICK
Pressure	Standard	Standard	Standard	Standard
Gradient	Green Gauss Cell Based	Green Gauss Cell Based	Green Gauss Cell Based	Green Gauss Cell Based
Momentum thickness Re	N/A	N/A	N/A	QUICK
Intermittency	N/A	N/A	N/A	QUICK

Table 2.3: Viscous models specifications.

Viscous model	**Specifications**
Laminar	N/A
k–ε	Standard
	Standard wall functions
k–ω	Standard
	Shear flow correction
	Production limiter
SST-transition	Production Kato-Launder
	Production limiter
	Intermittency: 1

This problem was solved by using continuity equation (Eq.2.4) for both the laminar and RANS models. The momentum equation for the laminar model is described by Eq. 2.5 and the RANS models is decribed by Eq. 2.6. The k-ε and the k-ω models are categorized as first order and two equation models. One equation solves for the kinetic energy and the second equation for the dissipation rate of energy (Tabatabaian, 2015). The SST model uses two more extra equations one for the intermittency and one for the oncet transition. These transport equations are describe in equations 2.7-2.12. Further, Darcy Law was used to

capture pressure drop within the porous wall (Eq. 2.13). The Forchheimer correction factor was neglected since the velocities in the porous medium are very low.

Continuity equation:

$$\frac{\partial \rho U_i}{\partial x_i} = 0 \tag{2.4}$$

Momentum equations:

$$\frac{\partial \rho U_i U_j}{\partial x_j} = -\frac{\partial P}{\partial x_j} + \frac{\partial}{\partial x_j}\left[\mu\left(\frac{\partial U_i}{\partial x_j} + \frac{\partial U_j}{\partial x_i} - \frac{2}{3}\frac{\partial U_l}{\partial x_l}\delta_{ij}\right)\right] + F \tag{2.5}$$

$$\frac{\partial \rho U_i U_j}{\partial x_j} = -\frac{\partial P}{\partial x_j} + \frac{\partial}{\partial x_j}\left[\mu\left(\frac{\partial U_i}{\partial x_j} + \frac{\partial U_j}{\partial x_i} - \frac{2}{3}\frac{\partial U_l}{\partial x_l}\delta_{ij}\right)\right] + \frac{\partial}{\partial x_j}\left(-\overline{U_i' U_j'}\right) + F \tag{2.6}$$

where ρ is the density of air, U is the flow velocity, P is the system pressure, F is the porous media source and $\overline{U_i' U_j'}$ are the Reynolds stresses .

Transport equations for the k-ε model:

$$\frac{\partial \rho k U_i}{\partial x_i} = \frac{\partial}{\partial x_j}\left[\left(\mu + \frac{\mu_t}{\sigma_k}\right)\frac{\partial k}{\partial x_j}\right] + G_k - \rho\varepsilon \tag{2.7}$$

$$\frac{\partial \rho \varepsilon U_i}{\partial x_i} = \frac{\partial}{\partial x_j}\left[\left(\mu + \frac{\mu_t}{\sigma_\varepsilon}\right)\frac{\partial \varepsilon}{\partial x_j}\right] + C_{1_\varepsilon} G_k - C_{2\varepsilon}\rho\frac{\varepsilon^2}{k} \tag{2.8}$$

where k is the kinetic energy, ε is the rate of dissipation, μ is the flow viscosity, G_k is the generation of turbulent kinetic energy. Further, $C_{1\varepsilon}$ and $C_{2\varepsilon}$ are constants, α_k and α_ε are the turbulent Prandtl numbers for k and ε respectively, and the μ_t is defined in (Ansys, 2017).

Transport equations for the k-ω model:

$$\frac{\partial \rho k U_i}{\partial x_i} = \frac{\partial}{\partial x_j}\left[\Gamma_k \frac{\partial k}{\partial x_i}\right] + G_k - Y_k \tag{2.9}$$

$$\frac{\partial \rho \omega U_i}{\partial x_i} = \frac{\partial}{\partial x_j}\left[\Gamma_\omega \frac{\partial \omega}{\partial x_j}\right] + G_\omega - Y_\omega \tag{2.10}$$

where ω is the specific dissipation rate, G_ω is the generation of $_\omega$, Γ_k and Γ_ω are the effective diffusivity and, Y_k and Y_ω is the dissipation of k and ω due to turbulence; these terms are defined in Ansys (2017).

Transport equations for the SST model include Equations 2.9 - 2.12:

$$\frac{\partial \rho U_j \gamma}{\partial x_j} = P_{\gamma 1} - E_{\gamma 1} + P_{\gamma 2} - E_{\gamma 2} + \frac{\partial}{\partial x_j}\left[\left(\mu + \frac{\mu_t}{\sigma_\gamma}\right)\frac{\partial \gamma}{\partial x_j}\right] \tag{2.11}$$

$$\frac{\partial \rho U_j Re_{\theta t}}{\partial x_j} = P_{\theta t} + \frac{\partial}{\partial x_j}\left[\sigma_{\theta t}(\mu + \mu_t)\frac{\partial Re_{\theta t}}{\partial x_j}\right] \tag{2.12}$$

where γ is the intermittency and $Re_{\theta t}$ is the transition momentum thickness Reynolds number. The rest of the parameters are defined in (Ansys, 2017).

For porous medium:

$$\frac{\partial p}{\partial x_i} = -\frac{\mu}{\alpha}\frac{\partial U_i}{\partial x_i} \tag{2.13}$$

where α is the permeability.

The porous medium was modelled as a fluid with a permeability of 2×10^{-14} m^2 . Additionally, in the porous wall, turbulent kinetic energy was set to zero for turbulent models. The system was performed isothermally at 290 K and 1 atm. At these conditions, the air density and molecular viscosity are 1.225 kg/m^3 and 1.789×10^{-5} Pa-s respectively. The simulations are completed under laminar and turbulent conditions as the gas has distinct inlet velocities (U_{in}) from 0.1 m/s to 10 m/s (Table 2.4) and turbulence conditions equally to 50 % of intensity and turbulent viscosity ratio of 1 and 10.

Table 2.4: Inflow velocities used to analyze flow pattern in a 2D GPF.

$\mathbf{U_{in}(m/s)}$	**Re upstream ($\mathbf{Re_d}$)**	**Re within channel ($\mathbf{Re_c}$)**
0.1	20	23
1	201	228
5	1007	1138
9	1811	2049
10	2013	2276

Furthermore, a grid analysis was performed with the purpose of obtaining independent mesh results. The grid analysis was based on the mean velocity, TVR, and TKE numerical values throughout the channel. Three different uniform structured grid were executed: 70,380, 281,520 and 1.3 million cells. Consequently, this grid analysis yielded to a mesh of 281,520 quadrilaterals.

2.5 Discussion of results

The flow pattern along the representative element was predicted similarly by all the viscous models used. The numerical solution demonstrated that higher velocities are developed in the upstream of the inlet channels as well as the downstream of the outlet channels due to the change of cross section area. Figure 2.3, shows that the laminar model is highly dependent on inflow condition when $Re_c \geq 1138$. Further, for Re_c=228, the SST-transition model predicted significantly different mean velocity from the other viscous models (Figure 2.4), however, this pattern changes when Re increases (Figure 2.5). For instance, at Re_c=1138, the laminar model showed higher velocities along the channels as opposed to the k-ε. The latter is supported by Figure 2.6 so that when Re_c is 23, the numerical absolute velocity is not significantly different utilizing different approaches, although, remarkable differences are shown when Re_c increases to 1138.

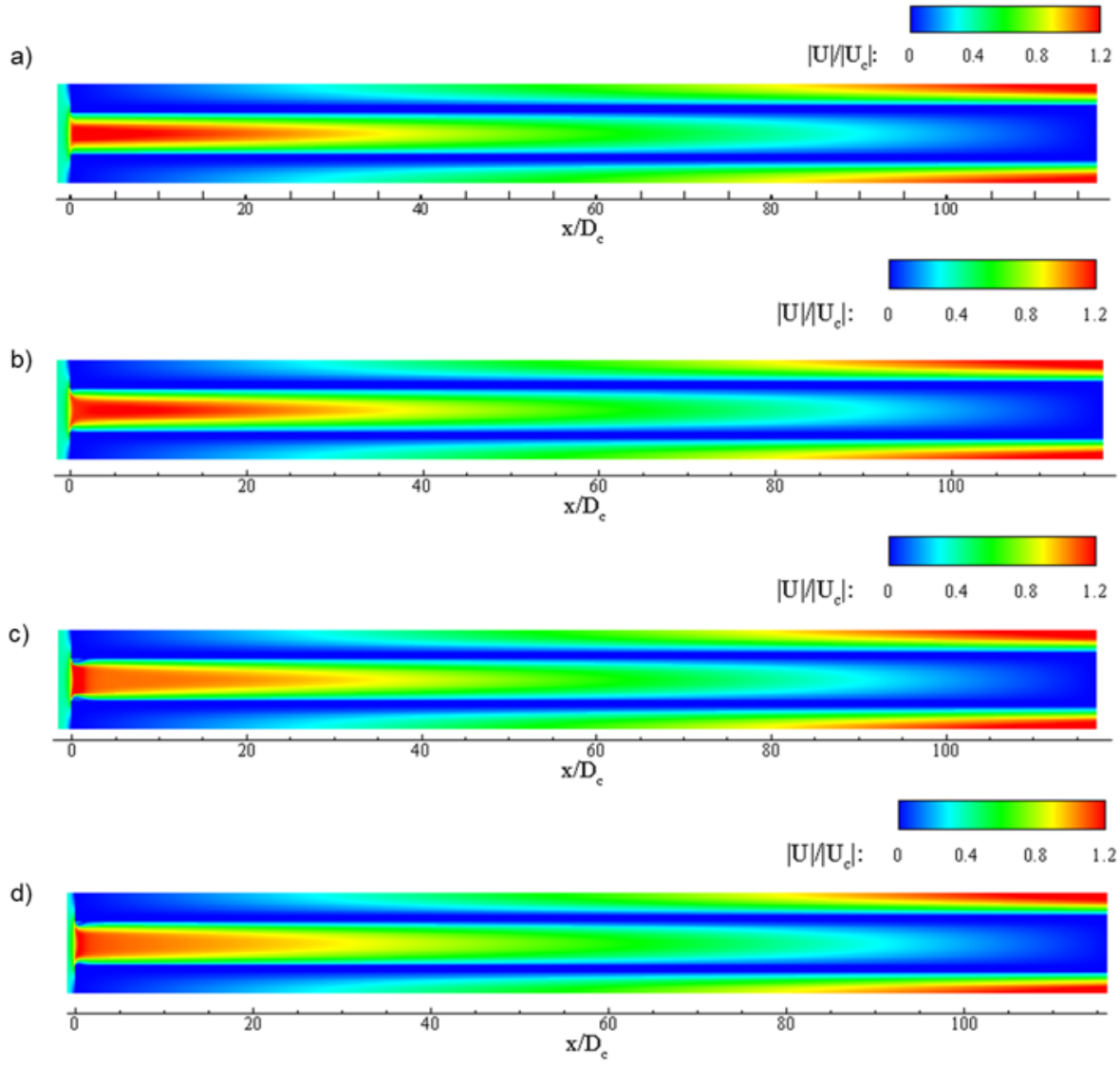

Figure 2.3: Absolute velocity along the channels using the laminar model. a)Re_c=23, b)Re_c=228, c)Re_c=1138, and d)Re_c=2276.

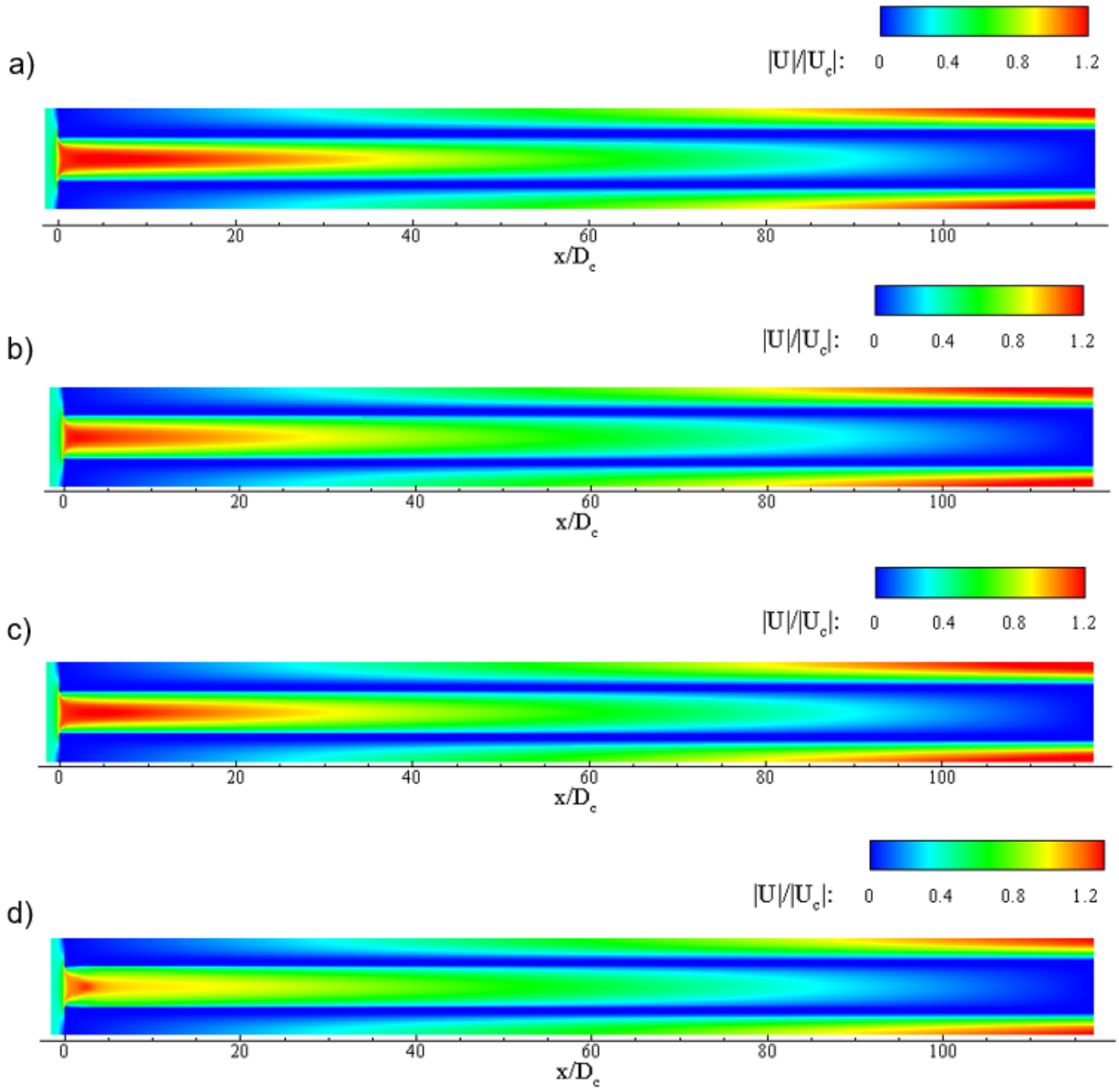

Figure 2.4: Absolute velocity along the channels using different viscous models with Re_c=228 (for turbulent models, TVR = 1). a)laminar, b)k-ε, c)k-ω, and d)SST-transition.

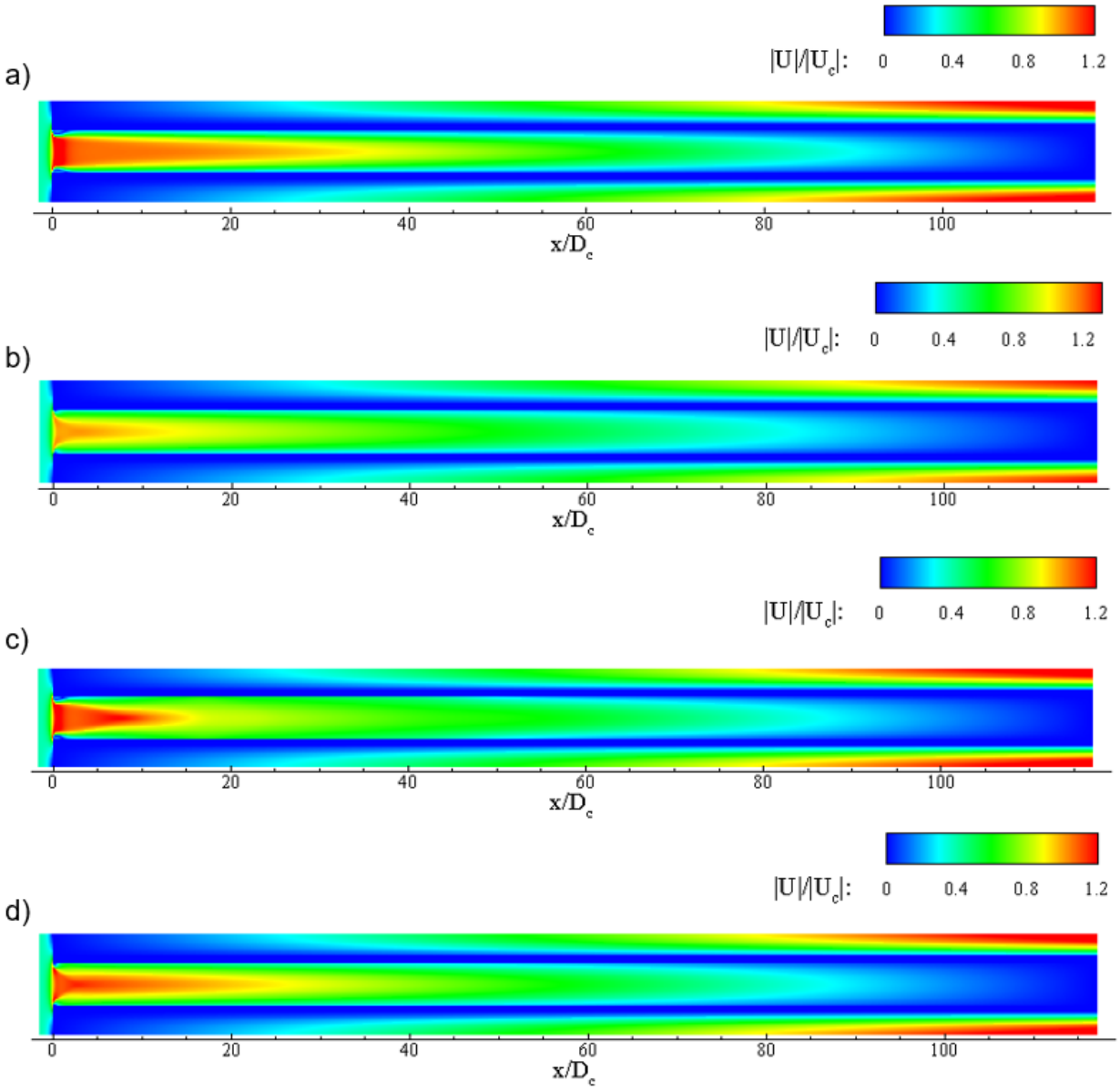

Figure 2.5: Absolute velocity along the channels using different viscous models with Re_c=1138 (for turbulent models, TVR = 1). a)laminar, b)k-ε, c)k-ω, and d)SST-transition.

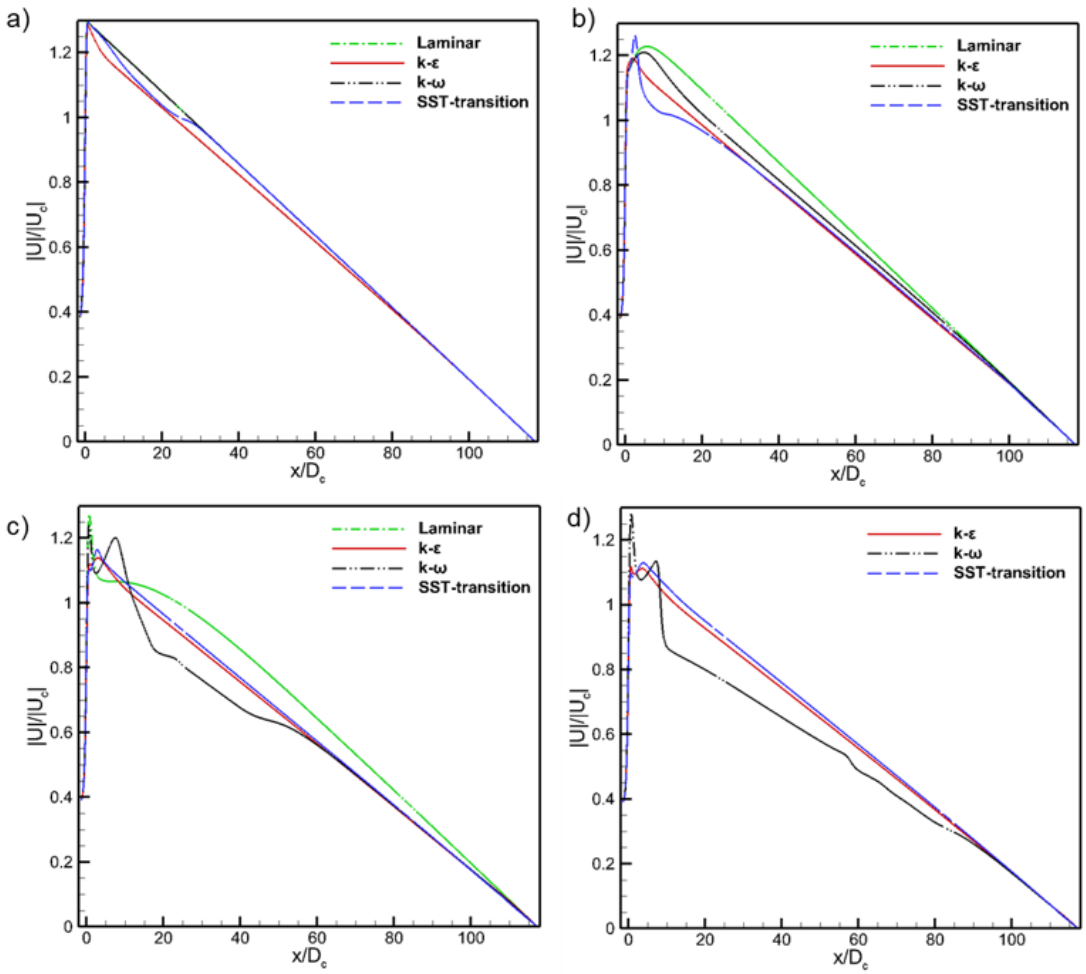

Figure 2.6: Absolute velocity in the middle of the inlet channel using different viscous models. a)Re_c=23, b)Re_c=228, c)Re_c=1138, and d)Re_c=2276.

Although it is well known that turbulent flow occurs when high Reynolds number is large (Wilcox, 2006), Cornejo et al. (2018a) indicate that small eddies prior to a catalytic converter monolith may enter to inlet channels provoking some turbulence that decays as flow moves downstream. Turbulence is a complicated phenomenon with many definitions and researchers often describe it as an eddying motion (Wilcox, 2006). TVR is the ratio of a turbulent viscosity, defined as the momentum transfer by turbulent eddies and the molecular dynamic viscosity which transfers momentum by molecular diffusion. Therefore, when using RANS models, if TVR has a value more than one, it means that some turbulence may be developed in the system. Figures 2.7 and 2.8, illustrate that turbulence may exist within

the inlet channels when $Re_c \geq 228$. These results also confirm turbulence damping for k-ε model unlike the model SST-transition which presents a turbulence increase at end of the channel for Re_c of 1138, due to a possible adverse pressure gradient. In contrast, the k-ω model estimates an increase in turbulence a bit after the inlet channel entrance which may be far from the reality. Furthermore, Figures 2.9 and 2.10 demonstrate that unsteadiness is proportional to Re_c. The k-ω model predicts unsteadiness a bit after the entrance while k-ε and SST-transition in the entrance of the inlet channel, which then damps downstream.

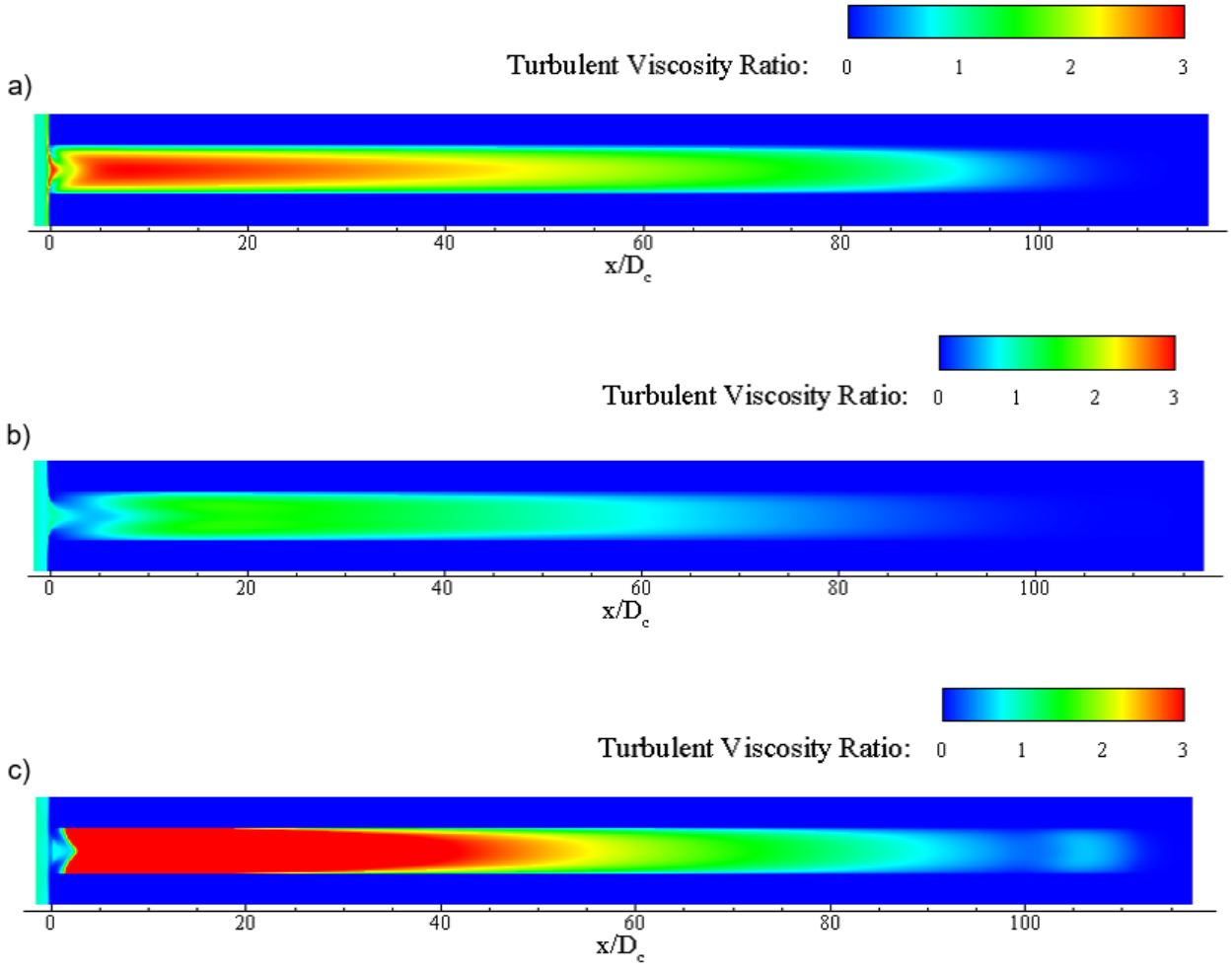

Figure 2.7: TVR along the channels using different RANS models with Re_c=228 and TVR=1. a)k-ε, b)k-ω, and c)SST-transition.

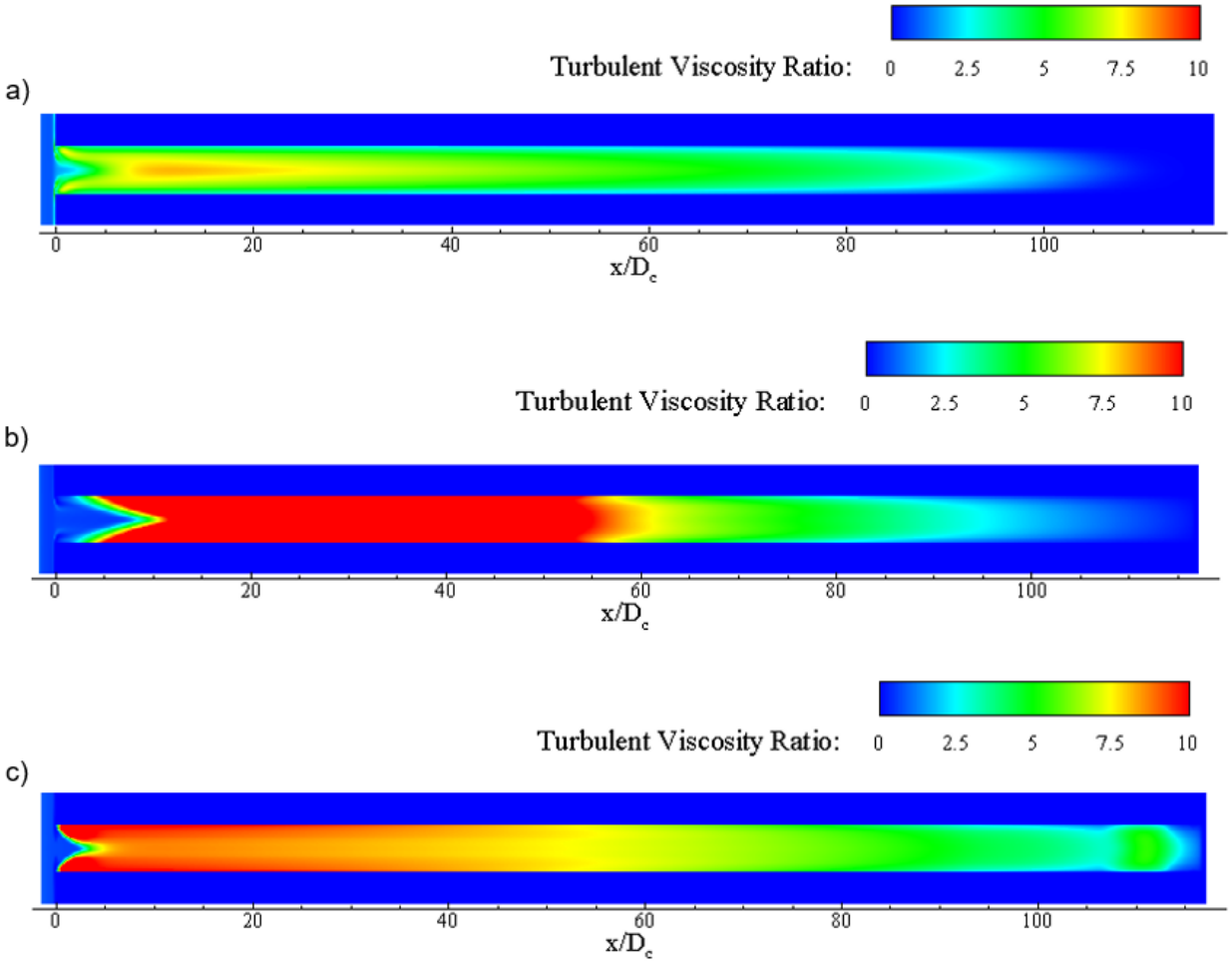

Figure 2.8: TVR along the channels using different RANS models with Re_c=1138 and TVR=1. a)k-ε, b)k-ω, and c)SST-transition.

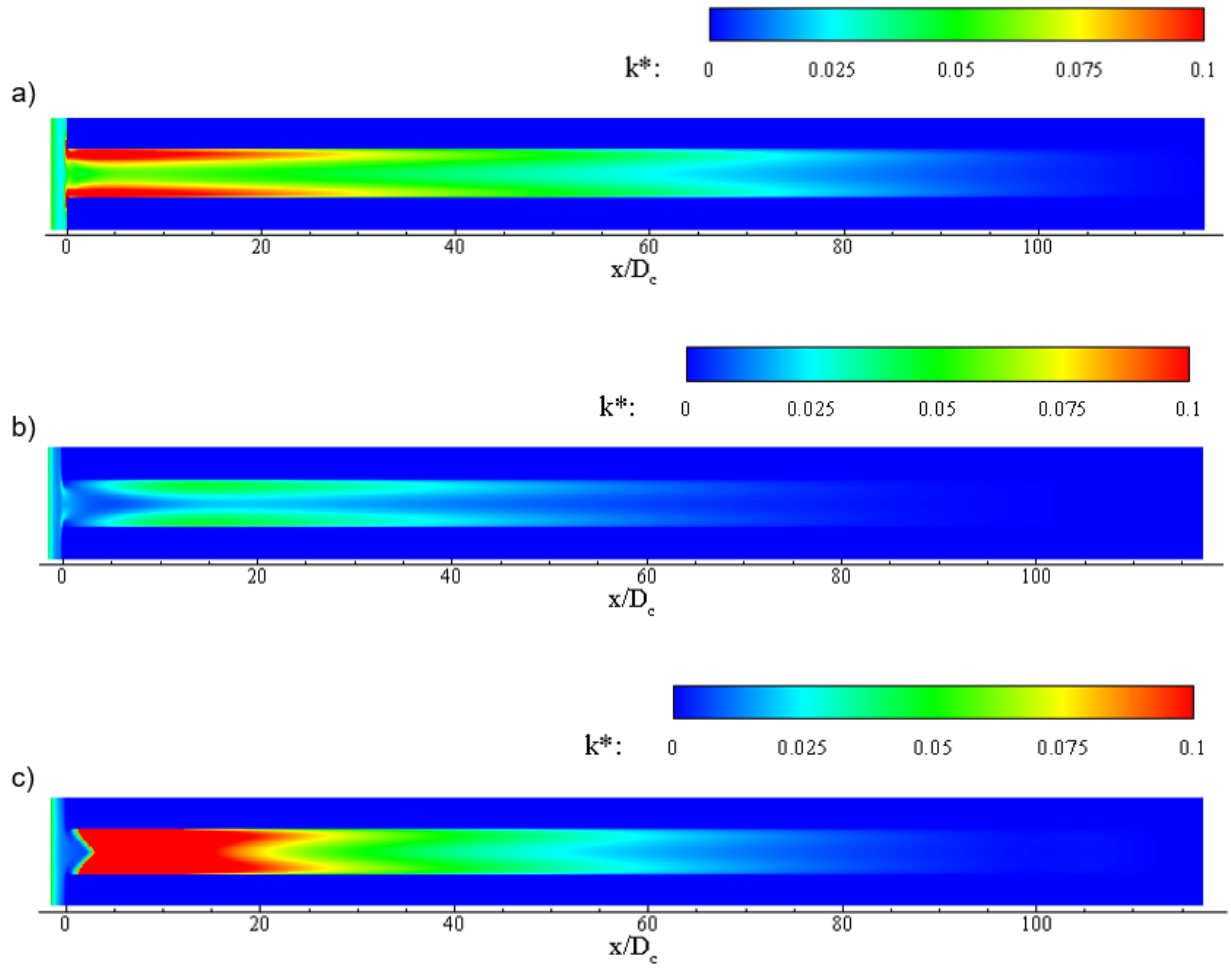

Figure 2.9: TKE along the channels using different RANS models with a Re_c=228 and TVR=1. a)k-ε, b)k-ω, and c)SST-transition (k^*=TKE/U_c^2).

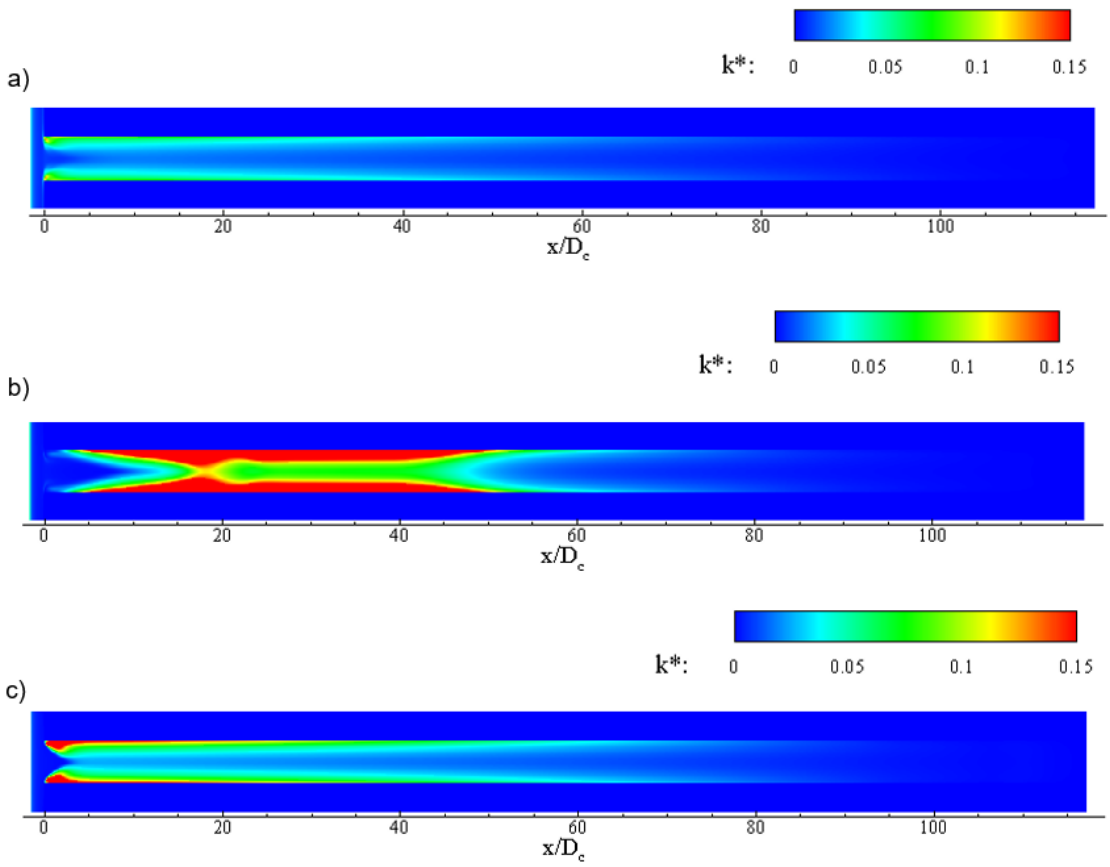

Figure 2.10: TVR along the channels using different RANS models with a Re_c=1138 and TVR=1. a)k-ε, b)k-ω, and c)SST-transition (k*=TKE/U_c^2).

The following figures exhibit the evolution of TVR and TKE as Re_c increases using different RANS models. In Figure 2.11, it is noticeable that none of the RANS models predicts turbulence for Re_c=23. However, k-ε and SST-transition models estimated turbulence at the entrance of the inlet channel for $Re_c \geq$68 while the k-ω showed it for $Re_c \geq$228. Notwithstanding, the latter model implied TVR drastically different from the other RANS models when $Re_c \geq$1138 (Figure 2.12). This discrepancy may be due the inaccuracy of the k-ω model at solving equations close to non-solid walls. Moreover, for $Re_c \geq$228, the SST model exhibited an increase of TVR at the end section of the inlet channel as observed in Figure 2.8. Additionally, in Figures 2.11 and 2.12, show that the TKE, which is the transfer of mean kinetic energy from larger to small eddies (Wilcox, 2006), behave very similar to TVR.

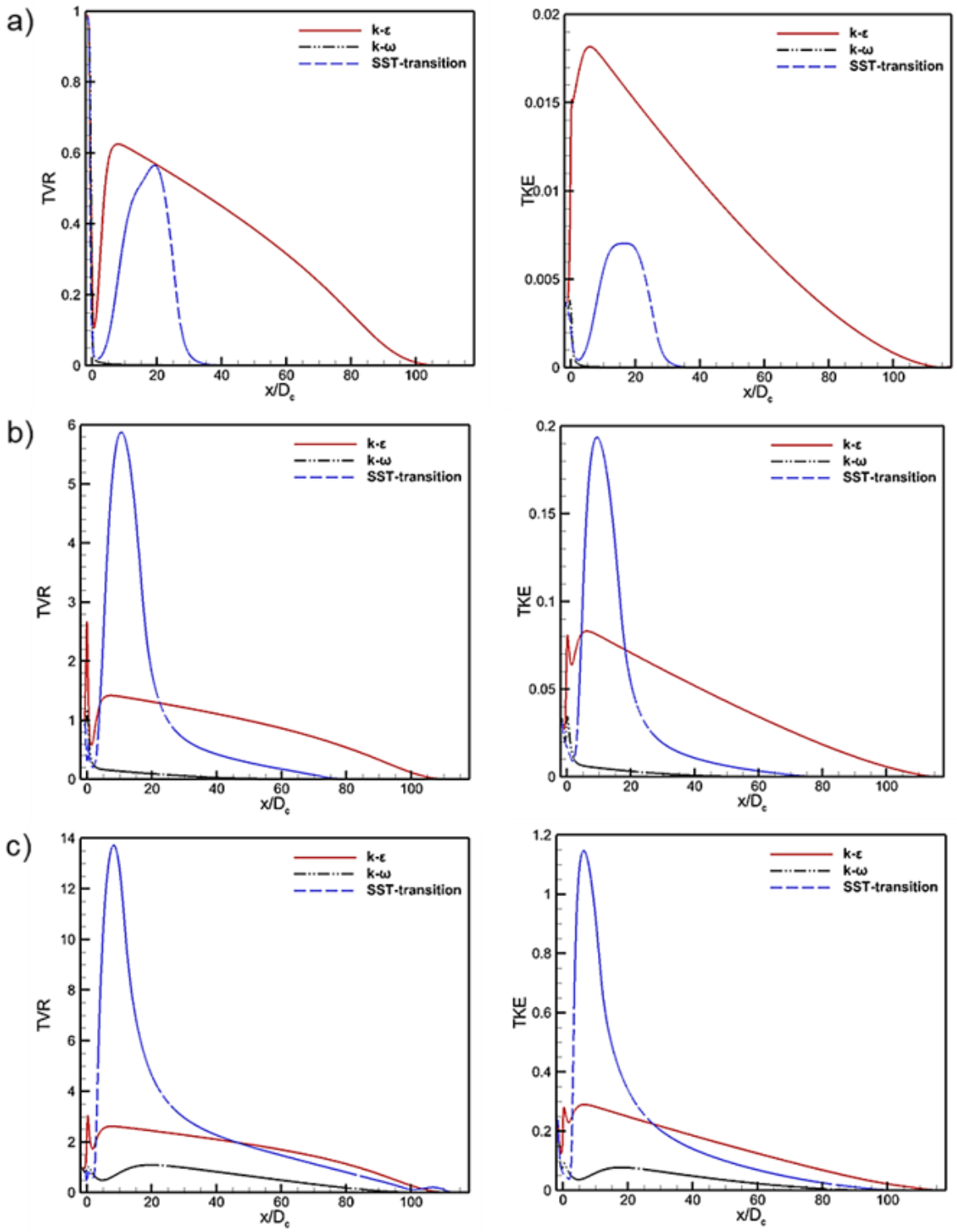

Figure 2.11: TVR and TKE along the channel for inlet TVR=1 and a)Re_c=23, b)Re_c=68, c)Re_c=182.

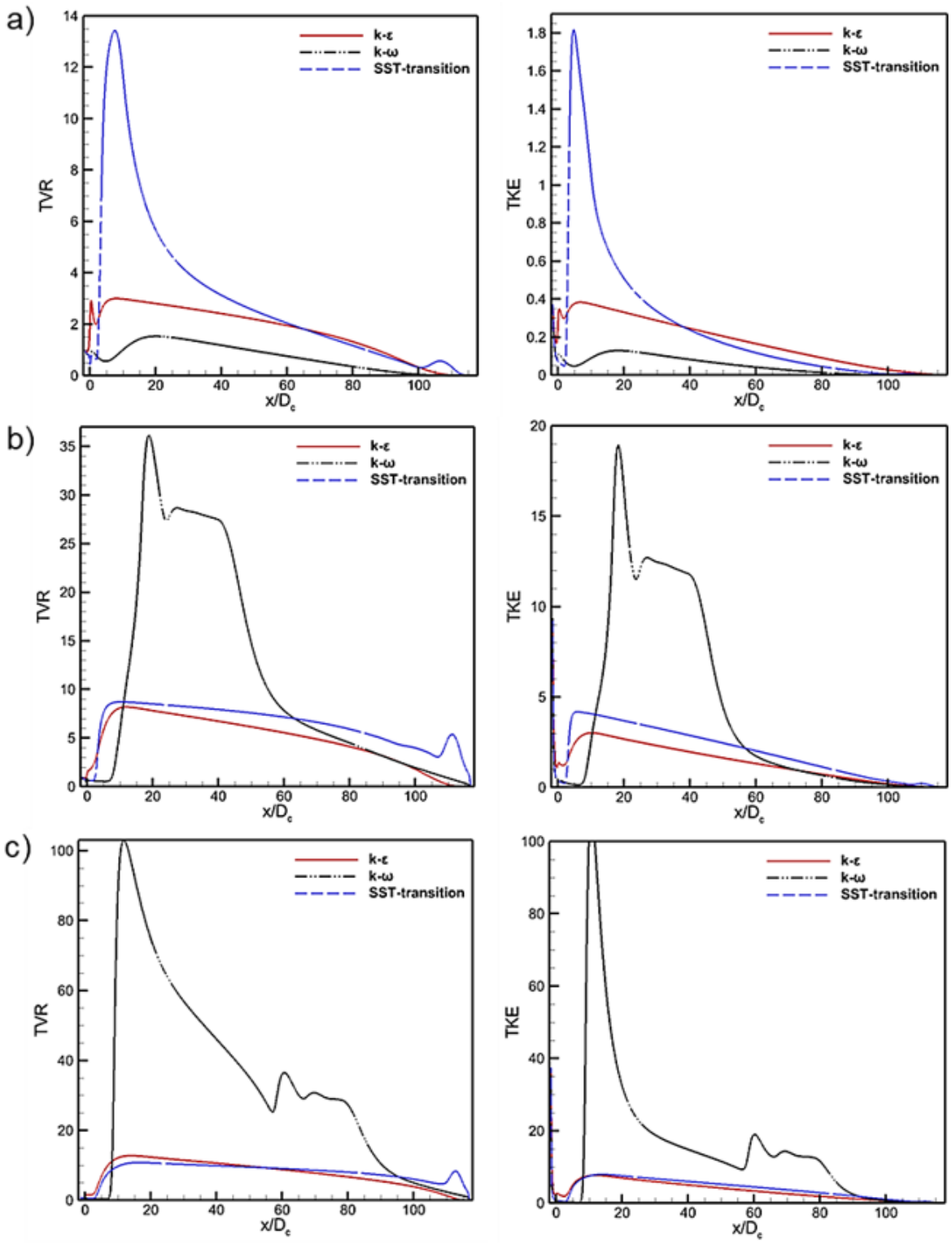

Figure 2.12: TVR and TKE along the channel for inlet TVR=1 and a)Re_c=228, b)Re_c=1138, c)Re_c=2276.

The aforementioned analysis demonstrated fluid behaviour when inlet velocity conditions change. However, the influence of TVR has not been explained. Figure 2.13, shows that absolute velocity is independent on TVR inflow conditions. Nevertheless, Figure 2.14 illustrates that turbulence increases at the beginning of the inlet channel, but it quickly damps taking the same form as when using TVR 1. This behaviour is similar to that explained in Cornejo et al. (2018a).

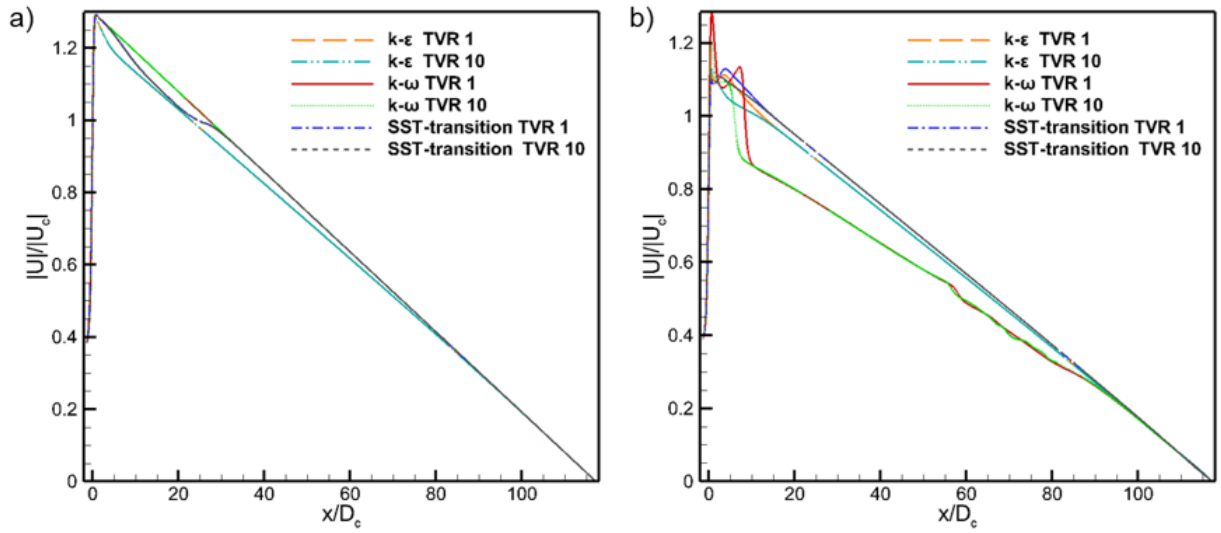

Figure 2.13: Absolute velocity in the middle of the inlet channel at different inlet TVRs: a)Re_c=23 and b)Re_c=2276.

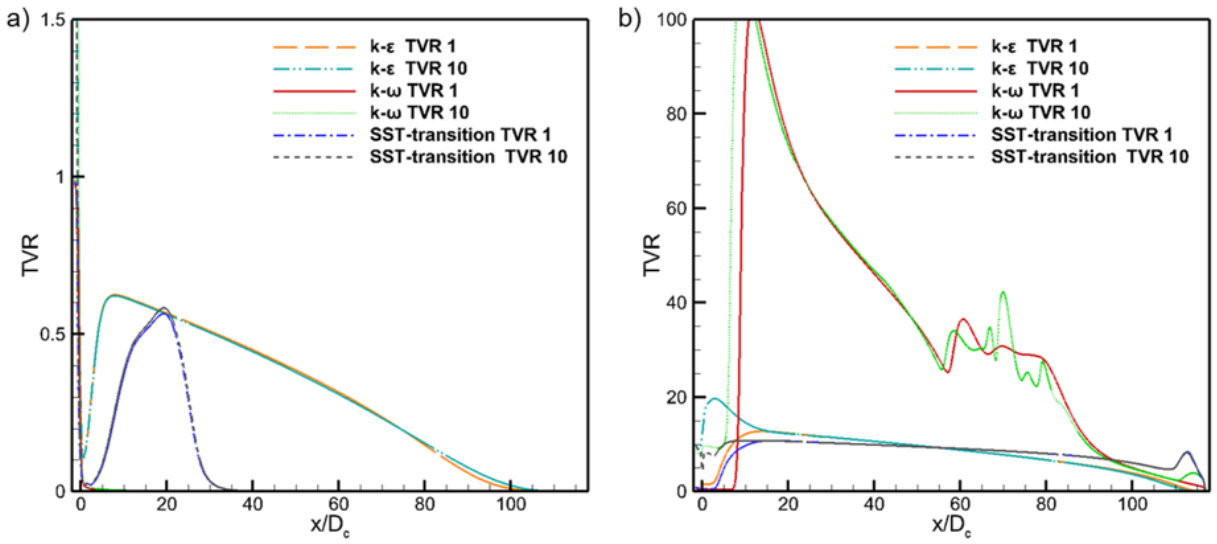

Figure 2.14: TVR in the middle of the inlet channel at different TVRs: a)Re_c=23 and b)Re_c=2276.

This study corroborates the fact that when using different viscous models with the same boundary conditions, the predicted data can differ from one another. Moreover, the resulting values vary drastically by changing inflow conditions as inlet velocities, but not inlet TVR. In addition, these results confirmed that turbulence may exist within the filter channel for $Re_c \geq 228$. Nevertheless, these results requires validation since RANS models are forced to work in laminar and transition regime same as the laminar, which is force to solve the problem in transition regime.

Chapter 3

Flow pattern in a representative element of a GPF in 3D

Laminar flow has been most commonly assumed when analyzing automotive particulate filters (PF). When the flow passes through small channels, it tends to be in the laminar regime but when disturbed, the flow may change into either transition or turbulent flow. The Reynolds number (Re) where transition occurs varies between 2000-2300, whereas for turbulent flow it is around 4000 (Tennekes et al., 1972; Landau and Lifshitz, 1987). In the transition regime, the flow may become unsteady but it remains laminar (James, 1994), however, as the velocity fluctuates in smaller regions, the flow pattern becomes more complicated until it reaches the turbulent regime (Landau and Lifshitz, 1987). Although turbulence is a complex phenomenon, transition is much less understood and poses a bigger challenge to engineers. Transition flow is initiated by instabilities that produce motion in three dimensions (Tennekes et al., 1972), and in a PF, these instabilities can be initiated by the increase of speed of the flow, the adjacent contact of flow with the porous mediums or by the crossflow initiated when the flow crosses the porous walls.

When modelling in different dimensions (one-dimension (1D), two-dimension (2D), and three-dimension (3D)) different results are usually obtained due to varying factors such as

mesh quality, turbulence therein, geometry and flow simplifications, among others. Turbulence flow patterns are inherently three dimensional in nature. Ekambara et al. (2005) simulated a bubble column reactor and compared the numerical predictions using three different dimensions (1D, 2D and 3D). They noticed that the axial liquid velocity was predicted similarly between the three geometries, however, the eddy viscosity and the Reynolds stresses exhibited larger differences. The 1D model predicted the largest Reynolds stresses followed by the 2D model and then the 3D model. They concluded that the latter discrepancy was as a result of simplifying the turbulent transport equation. Clearly, the 3D model provided a better approximation due to its proximity to the experimental data.

In a PF, the flow experiences friction in four porous walls and crosses them in four directions, leading to a more tortuous flow pattern that can induce vortices which can only be described using a 3D geometry. Therefore, this section focuses on the examination of flow behaviour within a 3D representative element of a gasoline particulate filter (GPF). The analysis reports velocity profiles, turbulent kinetic energy (TKE) and turbulent viscosity ratio (TVR) to understand the possible emergence of turbulence. Further model validation is addressed by comparing experimental data and numerical pressure drop using several flow and turbulence conditions.

3.1 Description of domain

The representative element of the GPF assumes that the flow across the monolith face is evenly distributed, and therefore the filter can be represented by one inlet channel and the surrounding outlet channels. The inlet channel measures 127 mm $\times$ 1.26 mm $\times$ 1.26 mm and contains a plug at the end section whereas, in the outlet channel, the plug is situated on the upstream face. Including the channels surrounding the inlet channel gives the final domain measurements as shown in 3.1. The total size of the inlet domain is 2.92 mm square and the porous medium wall has a thickness of 0.20 mm. The fluid enters the inlet channel, while

some flow passes through the porous walls towards the adjacent outlet channels and hence, the fluid reaches the filter exit. This domain does not include a section after the substrate since expansion effects are not covered in this part of the investigation.

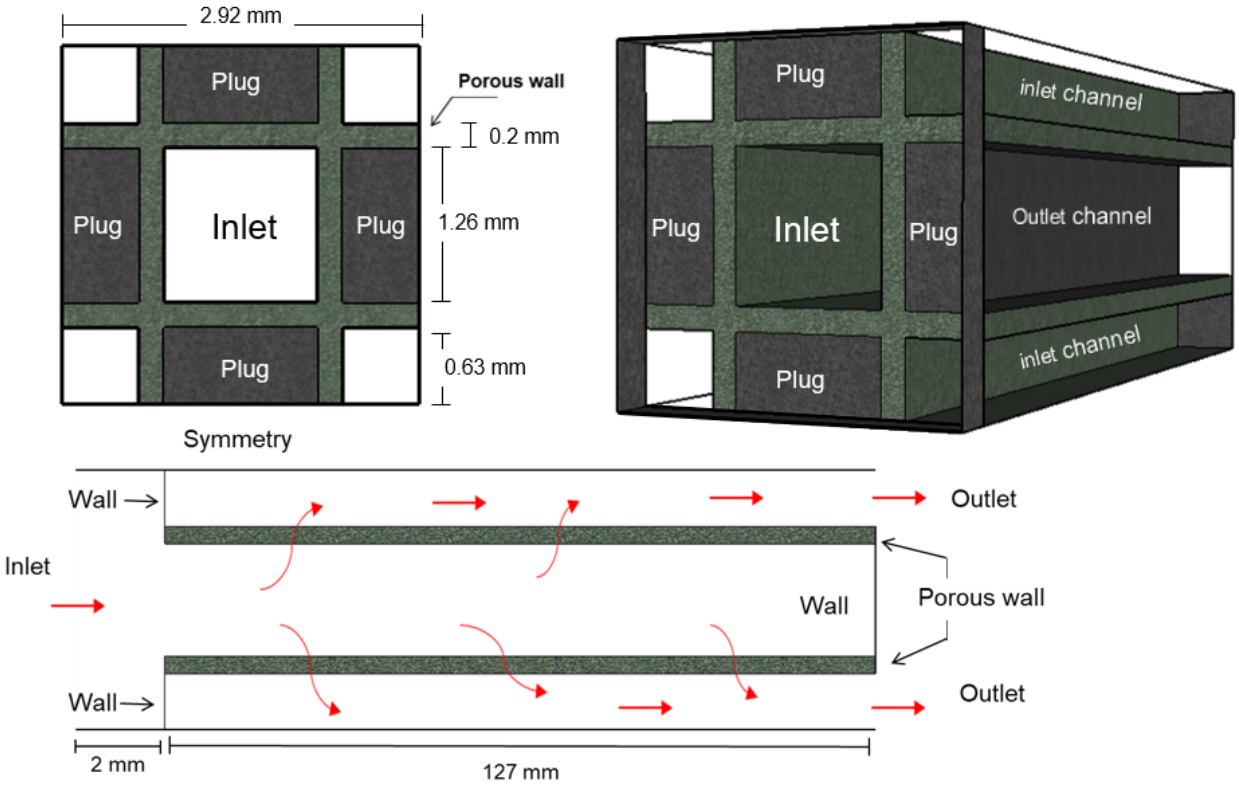

Figure 3.1: Representative element of a gasoline particulate filter.

The system is solved using Equations 2.4-2.8 and 2.11-2.13 given in Chapter 2. The porous medium was modelled as a fluid with a permeability of 1.13×10^{-11} m^2 . Additionally, in the porous wall, the turbulent kinetic energy was set equals to zero. The system was set to perform isothermally at 290 K and 1 atm. At these conditions, the air density and molecular viscosity are 1.225 kg/m^3 and 1.789×10^{-5} Pa-s respectively. The simulations are completed under laminar and turbulent conditions as the gas has distinct inlet velocities (U_{in}) from 1 m/s to 10 m/s (Table 3.1) and turbulence conditions equally to 60 % of intensity and turbulent viscosity ratio of 10.

Table 3.1: Inlets velocities used to analyze flow in a GPF.

$\mathbf{U_{in}(m/s)}$	**Re upstream** ($\mathbf{Re_d}$)	**Re within channel** ($\mathbf{Re_c}$)
1	200	232
3	600	695
5	1000	1158
7	1400	1622
10	2000	2317

3.2 Experimental approach

The experimental data were obtained using a flow system described in Figure 3.2. The GPF was a 300 CPSI monolith with a channel diameter and a length of 1.26 mm and 127 mm respectively, as shown in Figure 3.1. The pressure and temperature were measured upstream the GPF, which were 92 kPa and 21 °C. The flow was free of particulates and the pressure drop lecture was registered using a series of Honeywell piezoelectric pressure sensors (part number RSCDRRI002NDSE3) for 12 flowrates from 0.05 m^3/hr to 268 m^3/hr (see Figure 3.2). Further, the volumetric flowrate was set using a variable frequency drive that controls the regenerative blower so that generates centrifugal airflow.

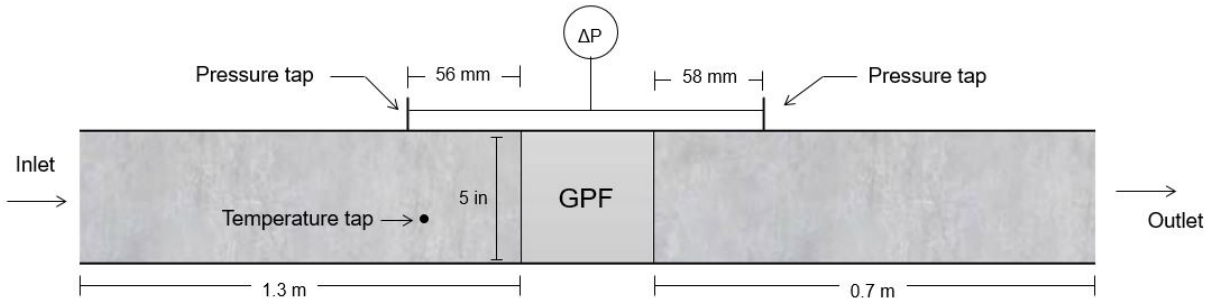

Figure 3.2: Schematic of equipment used to obtain experimental pressure drop in GPF.

3.3 Numerical solution

This system performed steady state simulations using the computational fluid dynamics (CFD) software, ANSYS-Fluent. Different viscous models such as laminar, k-ε, k-ω and SST-transition models where use to analyze the flow in a GPF. The discretization and specifications of the previously mentioned viscous models are given in Tables 3.2 and 3.3. The convergence criterion was to reach a value for the scaled residuals in the order of 10^{-6} for the transport variables as well as having a stable value for the total pressure drop, volume average of TKE, TVR and mean velocity.

Table 3.2: Viscous models discretization.

Discretization	**Laminar**	**k − ε**	**k − ω**	**SST-transition**
Scheme	Simple	Simple	Simple	Simple
Specific dissipation rate	N/A	N/A	2^{nd} order Upwind	2^{nd} order Upwind
Turbulent dissipation rate	N/A	2^{nd} order Upwind	N/A	N/A
Turbulent kinetic energy	N/A	2^{nd} order Upwind	2^{nd} order Upwind	2^{nd} order Upwind
Momentum	2^{nd} order Upwind	2^{nd} order Upwind	2^{nd} order Upwind	2^{nd} order Upwind
Pressure	Standard	Standard	Standard	Standard
Gradient	Green Gauss Cell Based	Green Gauss Cell Based	Green Gauss Cell Based	Green Gauss Cell Based
Momentum thickness Re	N/A	N/A	N/A	2^{nd} order Upwind
Intermittency	N/A	N/A	N/A	2^{nd} order Upwind

Table 3.3: Viscous models specifications.

Viscous model	**Specifications**
Laminar	N/A
k–ε	Standard
	Standard wall functions
k–ω	Standard
	Shear flow correction
	Production limiter
SST-transition	Production Kato-Launder
	Production limiter
	Intermittency: 1

A grid analysis was completed using different meshes as illustrated in Figure 3.3. Clearly, despite good grid quality, a smoothly refined grid only at the inlet, centre or outlet do not provide mesh independent results. Therefore a uniform grid was adopted as it yielded better predicted values as a result of the reduction of numerical diffusion. This grid consisted of 3.3 million fully orthogonal hexahedral cells, thus, independent grid results are provided in this work. Additionally, to prevent the transition onset location from moving upstream in the Reynolds-average-Navier-Stokes models, the grid had $y^+ < 5$ (Menter et al., 2006b).

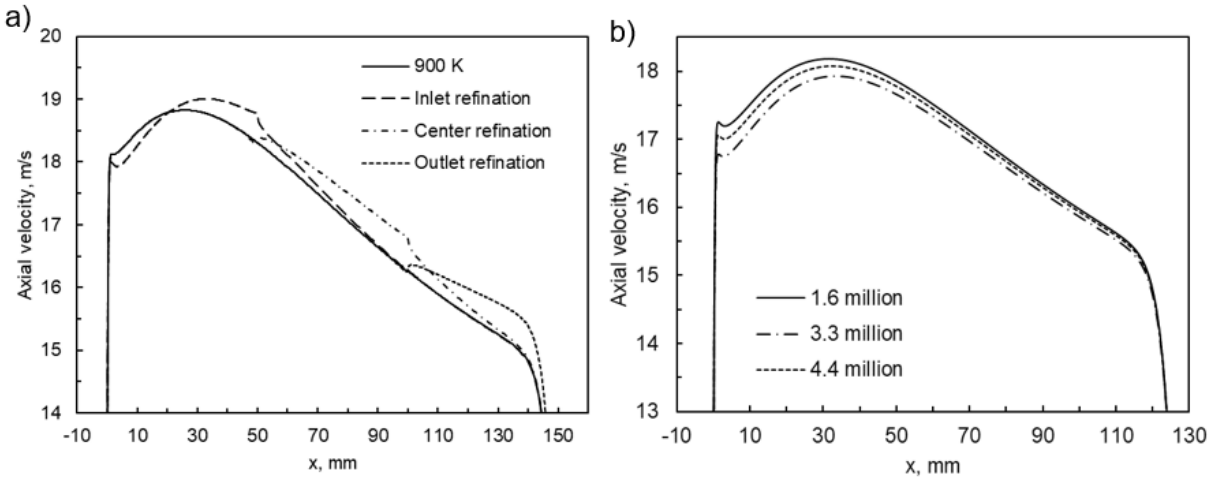

Figure 3.3: Grid analysis: a) grid refinement in different sections of the GPF and using a b) uniform grid.

3.4 Discussion of results

In Chapter 2, the RANS model, k-ω, predicted data significantly different between the laminar, k-ε and the SST-transition. In this study, the model k-ω did not converge as a steady state system. This was not an unusual response since this model is only effective when it is applied to flows bounded by solid walls (Wilcox, 2006) and here, the fluid is enclosed by four porous walls. Consequently, the investigation of flow behaviour within a GPF continued with the laminar, k-ε and SST-transition model.

Flow direction within the substrate of a GPF changes due to different factors that the fluid is subjected to. For instance, as the gas approaches the inlet channel, the flow contracts and undergoes the vena contracta effect. Furthermore, the fluid moves towards the end of the channel, facing a plug normal to the flow that also affects flow direction (Figure 3.4). Nevertheless, the use of a 2D or 3D geometry is less important in the middle of the channel as the flow direction points forward. However, the latter is only true when using the k-ε and the SST-transition models since the velocity profile is plain in the middle section as shown in Figure 3.5.

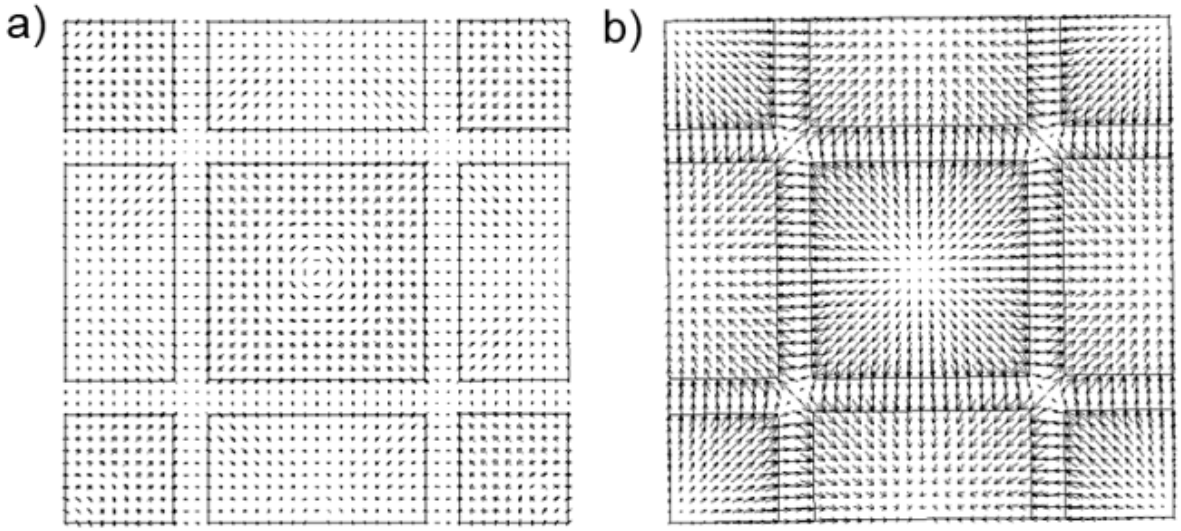

Figure 3.4: Flow direction in the monolith's a) upstream and b) downstream using the SST-transition model (Re_c=1158).

Figure 3.5, shows that k-ε and SST-transition models predict the mean absolute velocity (|U|) similarly, as opposed to the laminar model, which estimates absolute velocity significantly higher than RANS models. Moreover, Figure 3.5 also demonstrates that as Re_c increases, the ratio between |U| and the mean absolute inlet channel velocity ($|U_c|$) of the turbulent models change very little, while the gap in the laminar model increases notably. The turbulent models' velocity profile is very similar to that of a microchannel with rough walls studied by Wang and Wang (2007). Nevertheless, Piscaglia et al. (2005) supports the laminar behaviour, commenting that as the inlet velocity increases, the inertial forces stand out and therefore the fluid crosses the wall at the end of the channel, notwithstanding, that the analysis was done assuming laminar flow.

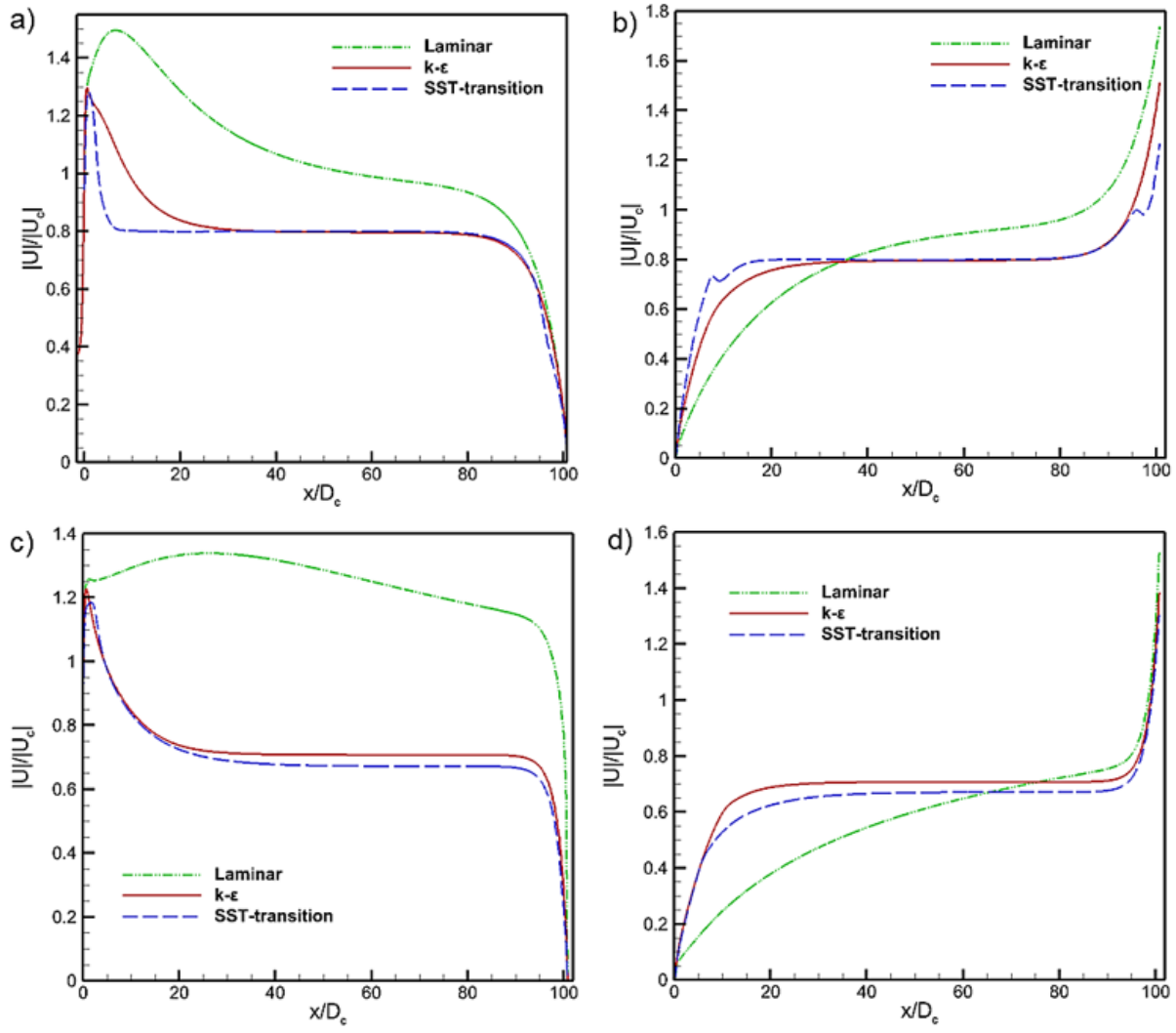

Figure 3.5: Absolute velocity ratio in the middle of the inlet (a and c) and outlet (b and d) channels using different numerical models in a 3D geometry: Re_c=232 (a and b) and Re_c = 1158 (c and d).

The turbulent models estimated that the flow mainly crosses the porous medium at the end of the channel similar to the laminar model with high Re_c. This is corroborated by Figure 3.6, where is noticeable that as Re_c increases, so does the ratio $|U|/|U_c|$ at the end of the porous wall, as Haralampous et al. (2004) observed using a 1D model. Therefore, the velocity within the porous wall is far from being considered uniform, as Oxarango et al. (2004) proposed.

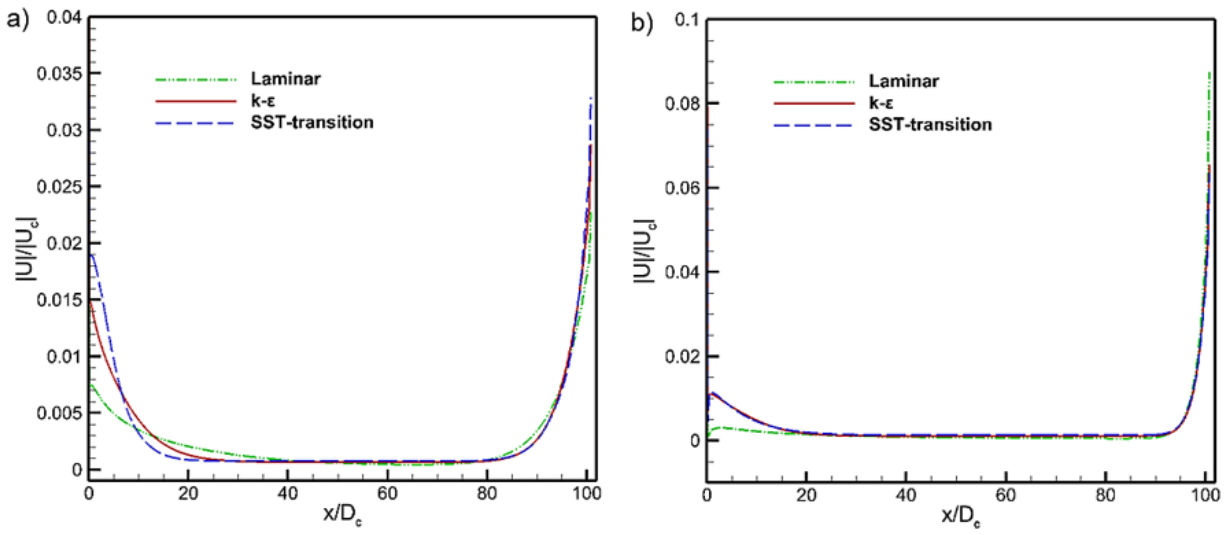

Figure 3.6: Porous wall velocity ratio using a) Re_c=232 and b) Re_c=1158.

TVR is the ratio of turbulent viscosity, defined as the momentum transfer by turbulent eddies and the molecular dynamic viscosity, which transfers momentum by molecular diffusion. Therefore, when TVR is more than one, the model implies turbulence in the system. Figure 3.7, exhibits that turbulence predicted by k-ε and SST-transition models rapidly decays in the first section of the inlet channel for $Re_c \geq$232. Further, the SST-transition model shows a second peak at the end section, similar to the results in Chapter 2, whereas the k-ε model exhibits it when Re_c=2317. This is due to the wall plug, which increases the pressure gradient forcing the fluid to cross the porous media and affecting the velocity profile (Figure 3.8). Additionally, since the velocity through the porous wall is not uniform, the injection of flow to the outlet channels may create tortuous flow inducing turbulence. Figure 3.7 illustrates the turbulence predicted by the k-ε and the SST-transition models, which shows that as Re_c increases so does the turbulence in the channels.

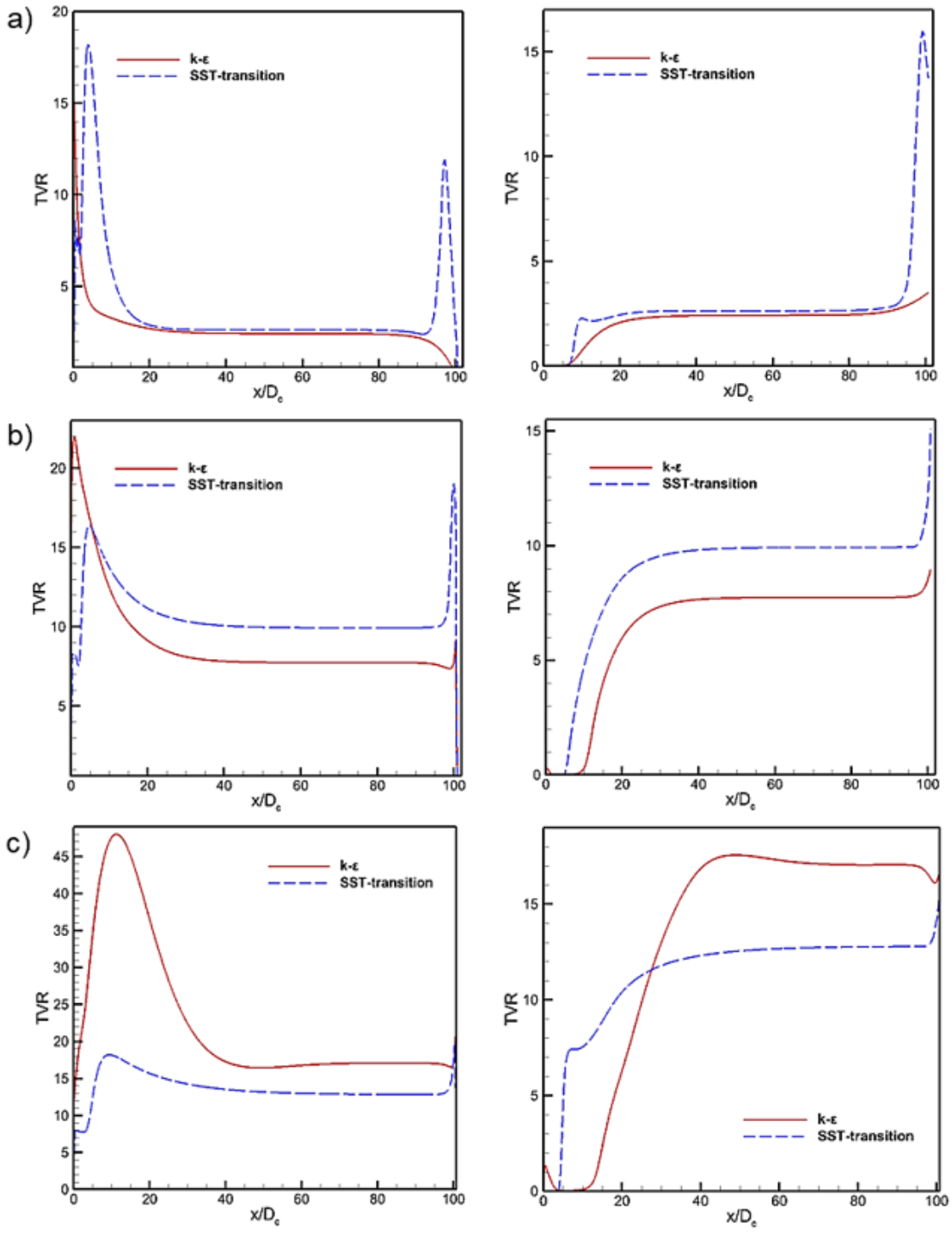

Figure 3.7: TVR in the middle of the inlet (left) and outlet (right) channels using different RANS models in a 3D geometry: a)Re_c=232, b)Re_c = 1158 and c)2317.

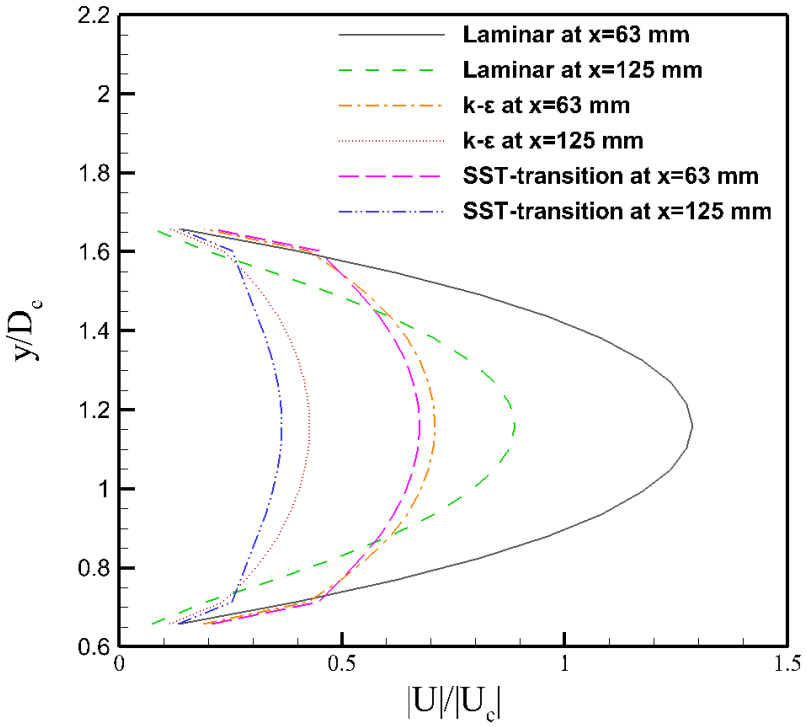

Figure 3.8: Velocity profile using different viscous models at different inlet channel sections.

At the entrance of the inlet channel, the Vena contracta phenomena affects the velocity profile (Figure 3.9). The k-ε model does not predicts acceleration close to the corners for Re_c <1158 as opposed to both the laminar and the SST-transition models, which demonstrate this acceleration from Re_c ≥232. This contraction effect may result in some vortices inducing unsteadiness.

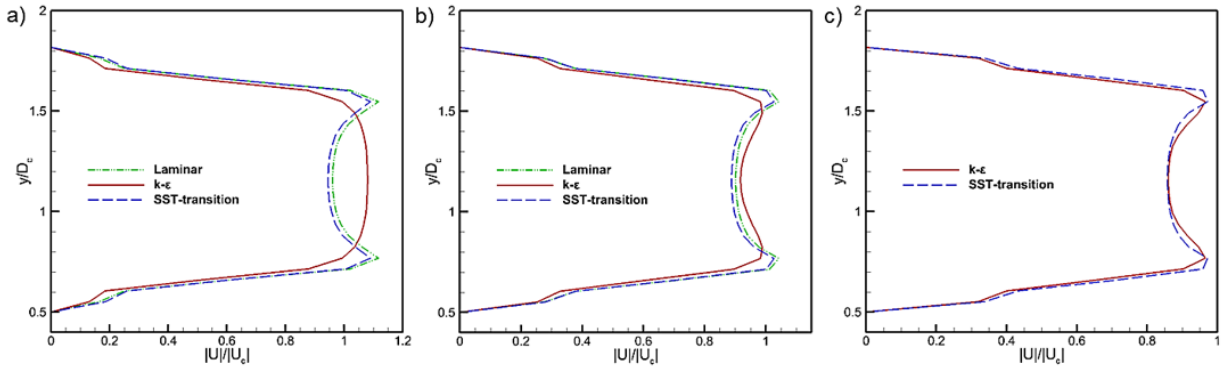

Figure 3.9: Velocity profile using different viscous models at the entrance of the inlet channel. a) Re_c=232, b) Re_c=1158 and c) Re_c=2317

Figures 3.10 and 3.11 illustrate that thek-ε and SST-transition models predict similar absolute velocity range along the channels, however, the SST-transition model estimates fully developed velocity for the most part of the channels. Furthermore, the k-ε model estimates lower turbulence and kinetic energy along the channels than the SST-transitional model, nonetheless, this latter model estimates higher turbulence at the end of the inlet channel. This corroborates a possible adverse pressure drop that previously was observable in Figure 3.7. Additionally, both models, the k-ε and the SST-transition show possible unsteadiness at the entrance of the inlet channel and at the exit of the outlet channel.

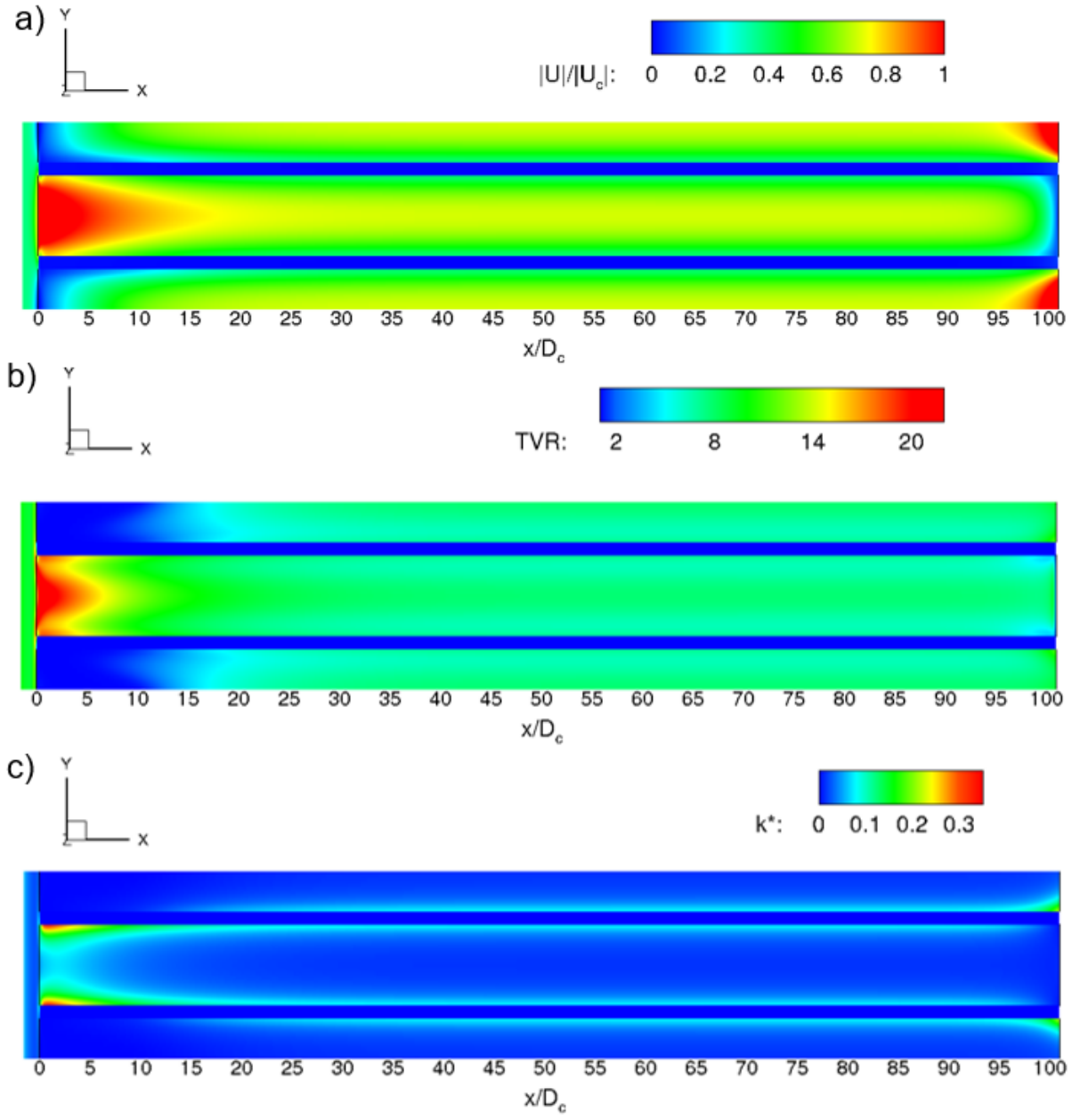

Figure 3.10: a)Absolute velocity, b)TVR and c)turbulent kinetic energy, k*=TKE/U_c^2 for Rec=1158 using the k-ε model.

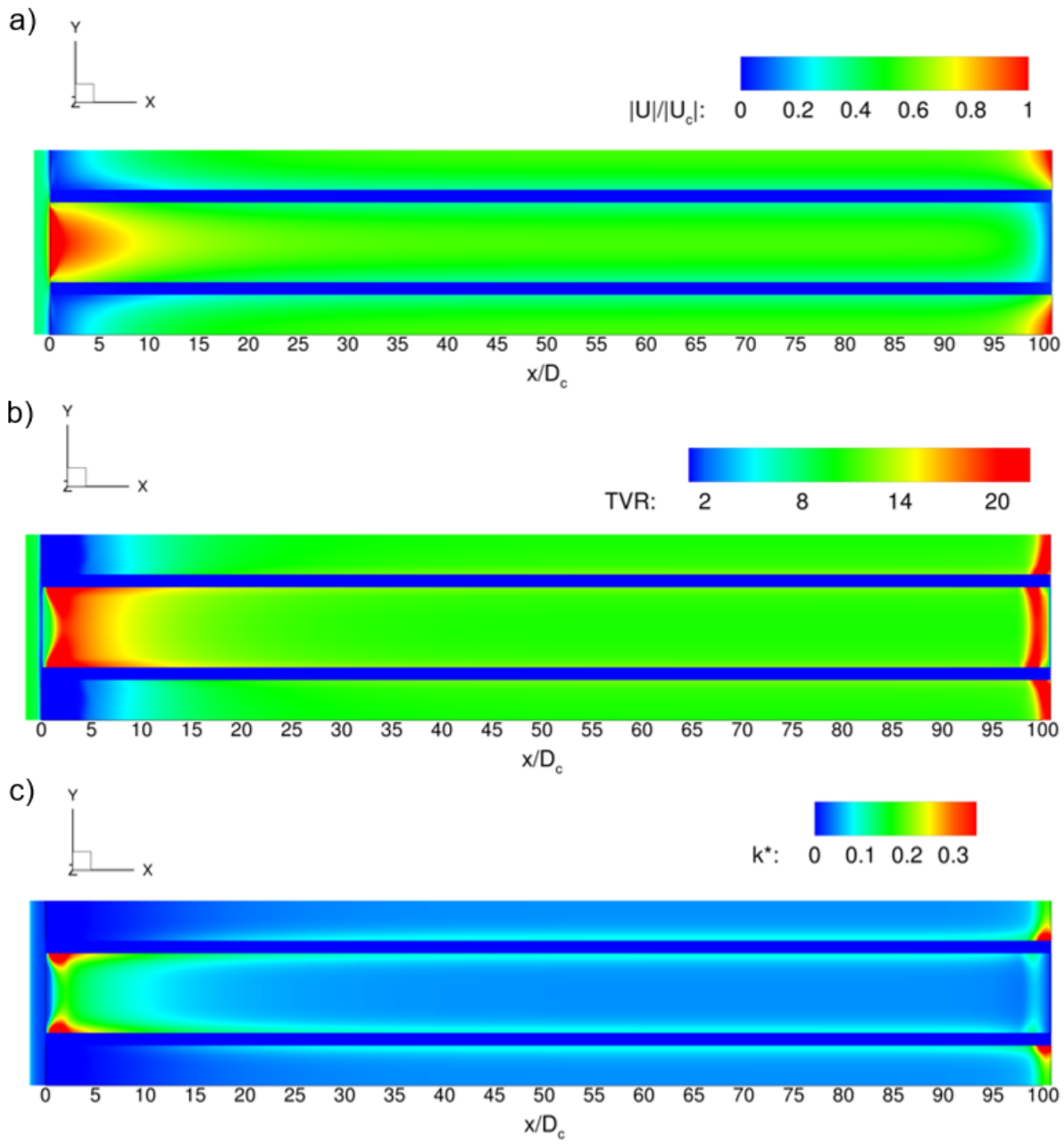

Figure 3.11: a)Absolute velocity, b)TVR and c)turbulent kinetic energy, k*=TKE/U_c^2 for Re_c=1158 using the SST-transition model.

The aforementioned analysis demonstrates the possible existence of turbulence or unsteadiness within the channels of a GPF. However, in modelling, the presence of a mix of laminar, transition and turbulent flow may provide false solutions. For instance, laminar

models tend to give a bad flow prediction when it is forced to work in turbulent flow. Similarly, the RANS models tend to provide incorrect approximations when they are compelled to work in laminar flows (Lodefier et al., 2003). Turbulence is an important factor as the formation of eddies will redirect soot particle trajectories (Wilcox, 2006). Choosing the right viscous model will aid in understanding different aspects of GPF like soot deposition, temperature gradients or pressure drop. Adding validation with experimental data increases the value of modelling, nevertheless, flow trajectory is very difficult to obtain experimentally.

When attempting to meet stringent regulations, one of the issues faced by the automotive industry is the pressure drop caused by the particle loading, which is proportional to fuel consumption (Yu et al., 2013). For this reason, the automotive industry is interested in a computational model that could help predict pressure drop. Accordingly, experimental pressure drop data were compared with numerical pressure drop predicted by the viscous models used (Figure 3.12). The computed numerical pressure drop was between the inlet channel and the outlet channel, as the contraction and expansion effects cannot be read using the schematic in Figure 3.1. As Figures 3.12 and 3.13 illustrate, initially, all the viscous models are close to the experimental values, however, as Re_c increases, they begin to deviate considerably. The k-ε model predicted pressure drop values closer to the experiments with an error of about 30 % while the SST-transition presented an error between 40-60 % and the laminar model of around 40 %. However, as Re_c increases, the k-ε model slightly deviates, while the SST-transition gets closer to the experimental curve. The latter is due to inertial forces that lead the flow towards the end of the inlet channel increasing the pressure gradient caused by the plug. The k-ε model does not accurately estimate this pressure gradient due to its ineffectiveness in solving problems close to solid walls.

The similarities between the k-ε and the SST-transition models is because the latter model accounts for transition and is coupled with the k-ε and k-ω models. In this case, the channels are surrounded by non-solid walls where the k-ω is not able to capture flow behaviour. Nevertheless, the k-ε provides good solutions away from walls. Therefore, the

SST-transition model provides numerical solutions like those by the k-ε model. Still, the SST-transition model adds the transition effect and uses the k-ω model at the end of the channel to capture the pressure gradient.

In general, the approximations by the viscous models are still far from the experiments for high Re_c. The plotted experimental data does not consider contraction and expansion losses that may considerably affect the numerical solutions. It should be noted that some publications mention that this effect is not highly significant.

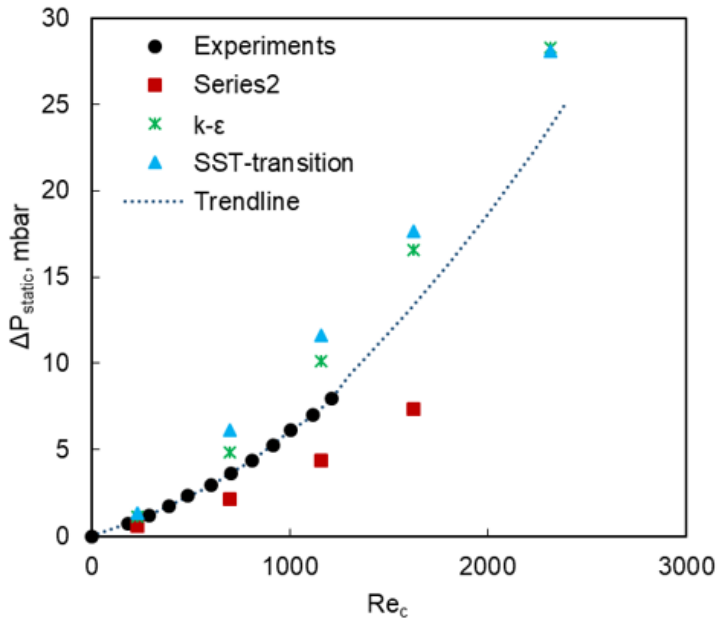

Figure 3.12: Static pressure drop within the channel using different numerical models and experiment values.

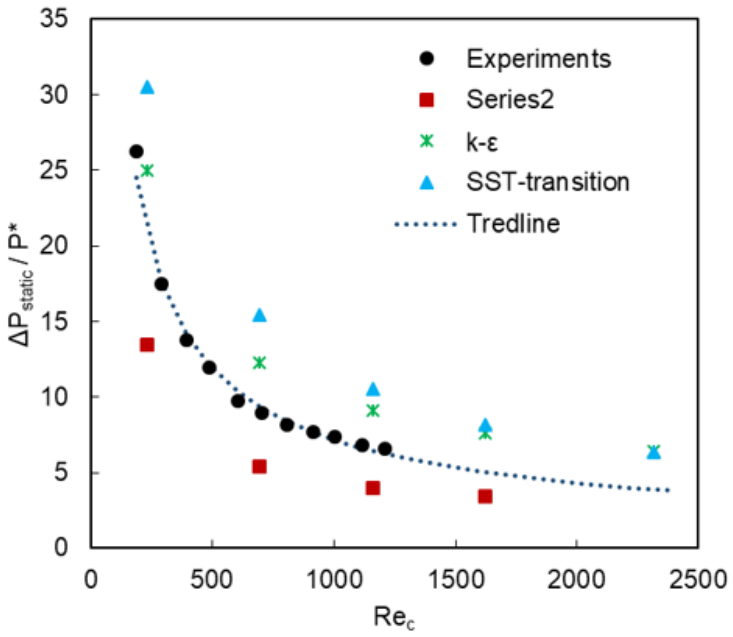

Figure 3.13: Ratio between the absolute static pressure and P* where $P^* = \frac{1}{2}U_c^2\rho$.

3.4.1 Comparison of 2D and 3D results

A 3D geometry is more realistic than 2D, however, the results between them are not necessarily significantly different. Often, 2D geometries provide higher velocities in the system than 3D domains, however, in this case, the results were the opposite (Figure 3.14). A possible reason is because in a 3D domain, the flow is in contact with four porous media with slip velocity that reduce the friction factor, thus, enhancing the velocity. In general, Figures 3.14 and 3.15 illustrate that when studying a GPF in distinct dimensions, the results are far from similar. For instance, the pressure drop predicted by the laminar model in 2D is 34 % lower than 3D, whereas for the RANS models this gap increases to 57 %. The gap between 2D and 3D domains is large enough that it cannot be neglected, nevertheless, there are a number of GPF studies published in 2D.

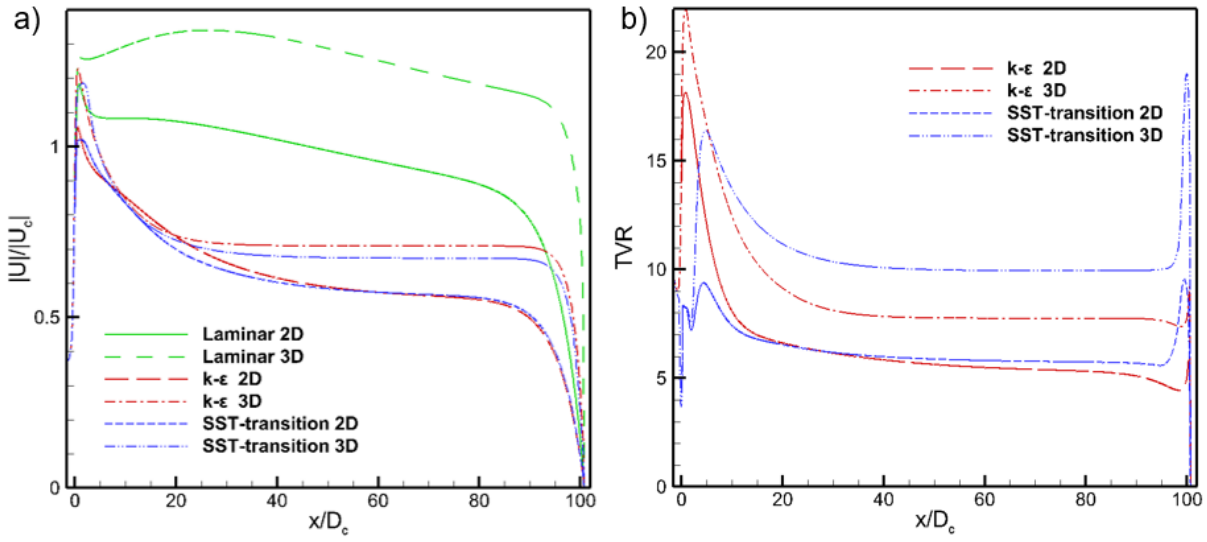

Figure 3.14: a) Absolute velocity and b) TVR in the middle of the inlet channel using Re_c=1158

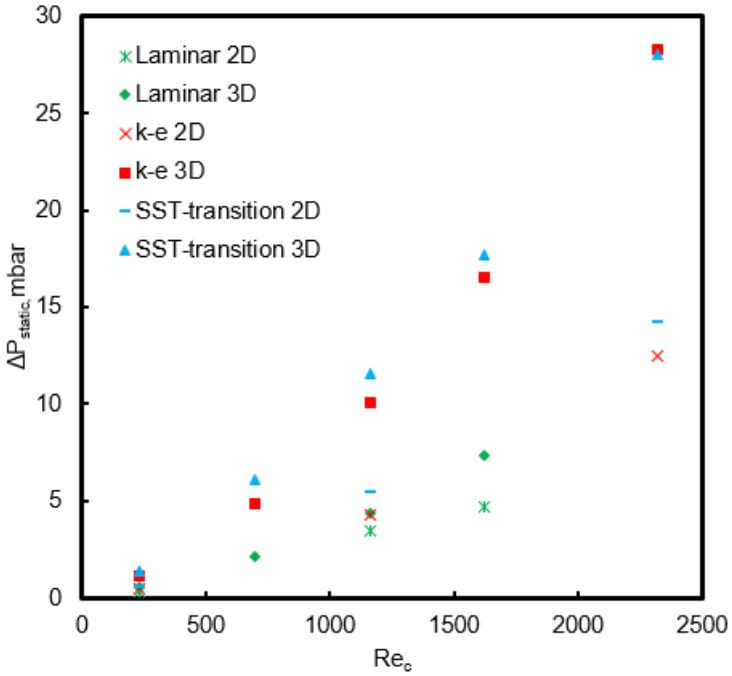

Figure 3.15: Numerical pressure drop using two different geometry dimensions and a Re_c=1158

Chapter 4

Contribution of contraction and expansion losses on the total pressure drop throughout a GPF

In literature, various investigations have demonstrated that when a fluid faces a sudden change in the cross section area, the friction factor increases (Ibrahim and Hashim, 1994). Lundgren et al. (1964) remark that pressure drop due to contraction is caused by the change in momentum and the wall friction of developed flow. Furthermore, when Cornejo et al. (2018b) studied the flow exiting a monolith in an automotive catalytic, they noticed that turbulence is generated under certain circumstances using the large eddy simulation. This flow pattern may exist in a GPF since its structure is very similar to that in an automotive catalytic converter.

This part of the investigation examines the importance of contraction and expansion losses in a GPF. The analysis uses different viscous models to approximate pressure drop using a long domain. This domain includes an inlet zone at the upstream and an outlet region at the downstream. Further, the numerical solutions are compared to experimental data to ascertain the viscous model that best describes a real GPF.

4.1 Description of the domain

The representative element of the GPF assumes that the flow across the monolith face is evenly distributed, and therefore the filter can be represented by one inlet channel and the surrounding outlet channels. The inlet channel measures 127 mm × 1.26 mm × 1.26 mm and contains a plug at the end section whereas, in the outlet channel, the plug is situated on the upstream face. Including an inlet zone, the channels surrounding the inlet channels and an outlet region, gives a final inlet domain measurements as shown in Figure 4.1. The total size of the inlet domain is 2.92 mm square and the porous wall has a thickness of 0.20 mm. The fluid flows through the inlet zone, and then enters the inlet channel, while some flow crosses the porous walls reaching the exit of the channels, and finally moves onwards to the outlet region. This domain will be called long domain since contraction and expansion effects are involved.

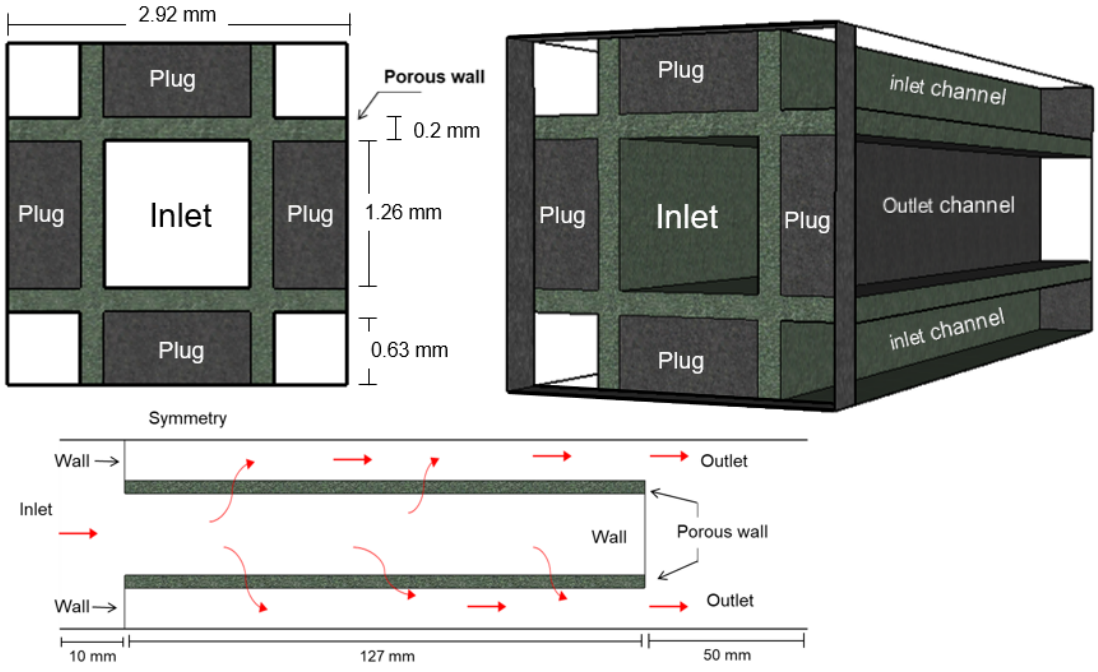

Figure 4.1: Schematic of the representative element of GPF in a long domain.

4.2 Governing equations and boundary conditions

The system is solved using Equations 2.4-2.8 and 2.11-2.13 given in Chapter 2. The porous medium was modelled as a fluid with a permeability of 1.13×10^{-11} m^2. Additionally, in the porous wall, the turbulent kinetic energy was set to zero. The system was isothermal at 290 K and 1 atm and at these conditions, the air density and molecular viscosity are 1.225 kg/m^3 and 1.789×10^{-5} Pa-s, respectively. The simulations were completed under laminar and turbulent conditions as the gas had a range of inlet velocities (U_{in}) from 0.1 m/s to 4 m/s (Table 4.1) and turbulence conditions equal to 60 % of intensity and turbulent viscosity ratio (TVR) of 1 and 10.

Table 4.1: Inlets velocities used to analyze flow in a GPF.

$\mathbf{U_{in}}$**(m/s)**	**Re upstream** ($\mathbf{Re_d}$)	**Re within channel** ($\mathbf{Re_c}$)
1	200	232
1.5	300	348
2	400	463
3	600	695
4	800	928

4.3 Numerical Solutions

This system performed steady state simulations using the computational fluid dynamics (CFD) software, $ANSYS - Fluent$. Different viscous models such as laminar, k-ε, and SST-transition models where used to analyze the flow in a GPF. The discretization and specifications of the previously mentioned viscous models are given in Tables 4.2 and 4.3. The convergence criterion was to reach a value for the scaled residuals in the order of 10^{-6} for all the transport variables as well as having a stable value for the total pressure drop, volume average of turbulent kinetic energy (TKE), TVR and mean velocity. Furthermore, a grid analysis was completed using different uniform meshes of 1.7, 4.7 and 13 million cells. Consequently, a uniform grid of 4.7 million fully orthogonal hexahedral cells was adopted with

y^+ <1 to prevent the transition onset location from moving upstream in turbulent models (Menter et al., 2006b).

Table 4.2: Viscous models discretization (long domain).

Discretization	**Laminar**	**k − ε**	**SST-transition**
Scheme	Simple	Simple	Simple
Specific dissipation rate	N/A	N/A	2^{nd} order Upwind
Turbulent dissipation rate	N/A	2^{nd} order Upwind	N/A
Turbulent kinetic energy	N/A	2^{nd} order Upwind	2^{nd} order Upwind
Momentum	2^{nd} order Upwind	2^{nd} order Upwind	2^{nd} order Upwind
Pressure	Standard	Standard	Standard
Gradient	Green Gauss Cell Based	Green Gauss Cell Based	Green Gauss Cell Based
Momentum thickness Re	N/A	N/A	2^{nd} order Upwind
Intermittency	N/A	N/A	2^{nd} order Upwind

Table 4.3: Viscous models specifications (long domain).

Viscous model	**Specifications**
Laminar	N/A
k–ε	Standard
	Standard wall functions
SST-transition	Production Kato-Launder
	Production limiter
	Intermittency: 1

4.4 Discussion of results

The addition of two zones at the upstream and downstream of the substrate makes modelling much more complicated. For instance, the convergence criterion becomes more difficult to obtain as was the case when using the k-ε model, where the problem did not converge. A

possible reason is that the k-ε model does not capture the turbulent boundary layer when the flow leaves the outlet channel, since a separation flow area is developed due to free shear layers. In contrast, the laminar model converged for U_{in} up to 2 m/s, whereas the SST-transition models for $U_{in} \leq 4$ m/s.

Fully developed flow is required where the pressure is quantified to avoid variations of mean velocities and turbulence quantities (Schetz and Fuhs, 1999) that may affect the pressure gradient. Figure 4.2, illustrates that when applying the laminar model with Re_c of 232, the long domain has a developed velocity profile at both, the upstream and the downstream face. Nonetheless, when Re_c increases to 463, the outlet zone is not long enough for the flow to reach developed velocity profile. Accordingly, the outlet zone was extended from 50 mm to 100 mm. Consequently, the new uniform grid resulted in 5.97 million fully orthogonal hexahedral cells. Figure 4.3, shows that the addition of 50 mm is sufficient to capture pressure drop for Re_c of 463. Notwithstanding, the numerical pressure drop implied by the laminar model yielded an insignificant difference of less than 1 %,when the length of the outlet zone was modified. Despite the small difference, the analysis proceeded with the larger outlet region due to complications with convergence.

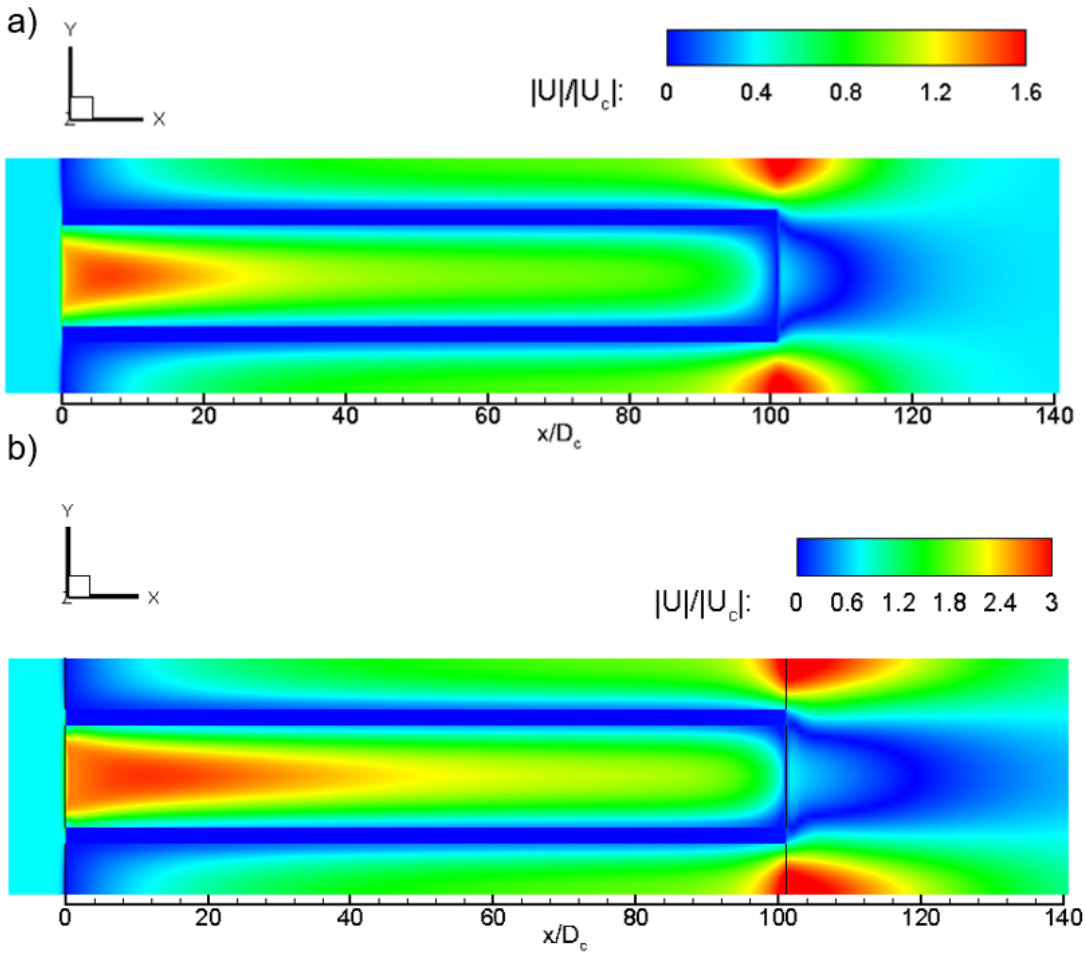

Figure 4.2: Numerical absolute velocity along the channel using the laminar model: a)Re_c=232 and b) Re_c=463.

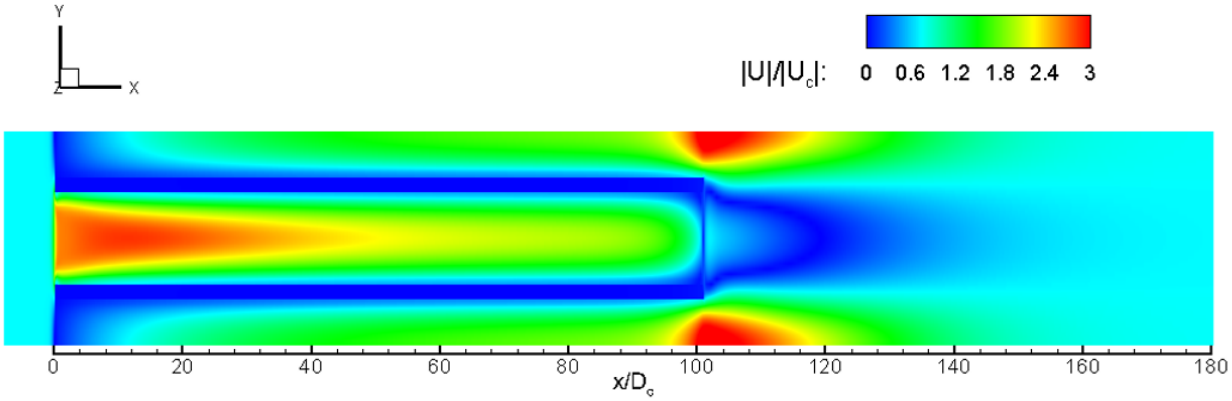

Figure 4.3: Numerical absolute velocity using the laminar model, 100 mm for the downstream section and a Re_c of 463.

When the flow leaves the outlet channel, it encounters a separation zone where free layers may cause the flow to roll up and form discrete vortices similar to a flow around a geometry as described by Bearman and Trueman (1972). In this study, the laminar model predicted a longer recirculation (separation bubble) than the SST-transition model. This separation bubble extends significantly as Re_c increases, only when using the laminar model (Figures 4.4 and 4.5). For instance, negative axial velocity is evident with a Re_c of 232 up to 18 mm after the monolith whereas for Re_c of 463 is noticeable until the flow reaches 30 mm, meaning that the recirculation increased by 66 %. This enlargement not only affects solution convergence, but also the friction loss since it is proportional to the bubble length (Fail et al., 1959).

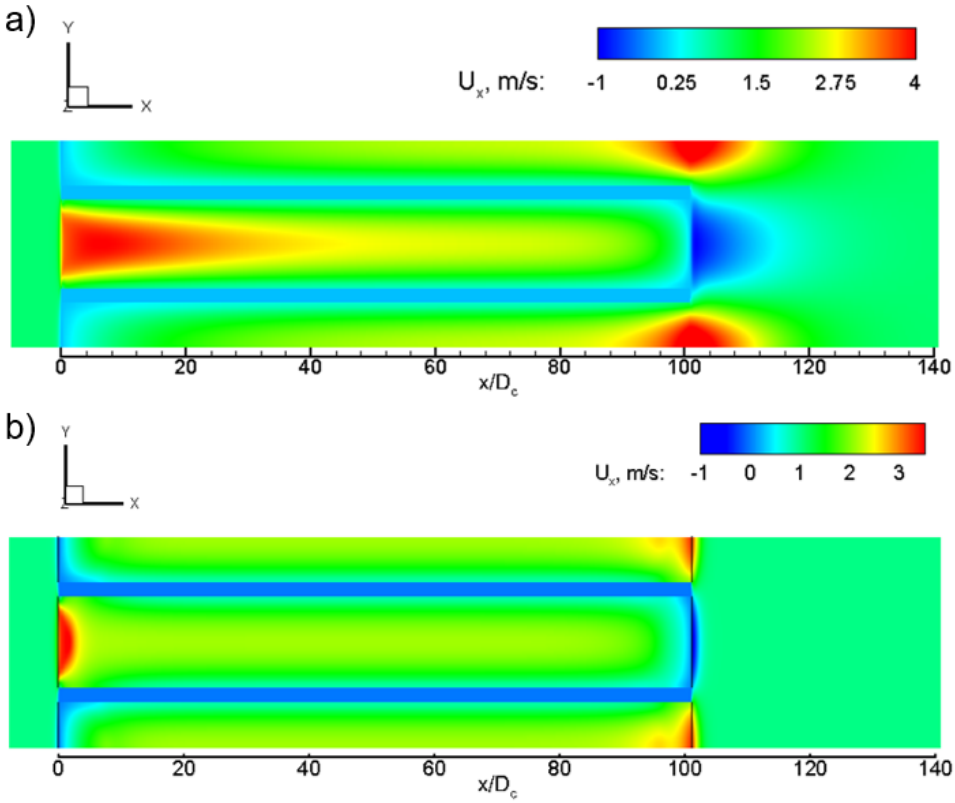

Figure 4.4: Axial velocity with Re_c of 232 and using both, the a)laminar and the b)SST-transition models (TVR=1).

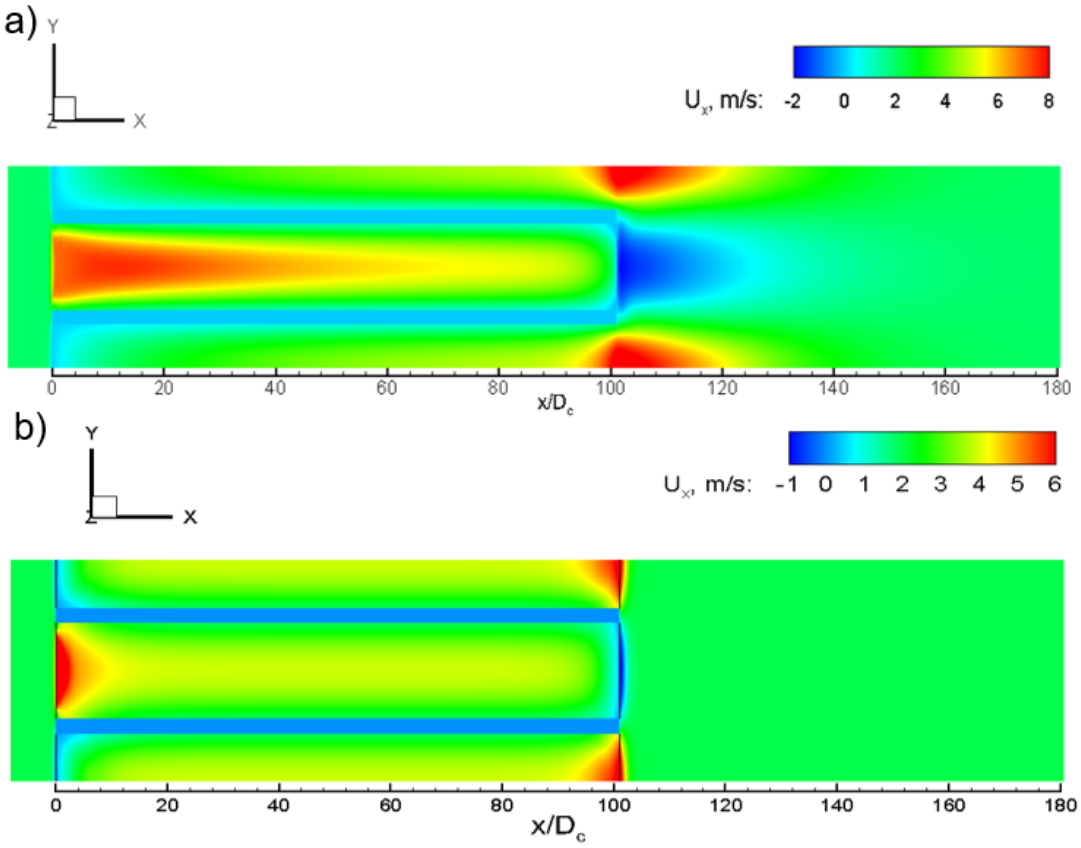

Figure 4.5: Axial velocity with Re_c of 463 and using both the a)laminar and the b)SST-transition models (TVR=1).

Figures 4.6 and 4.7 demonstrate that $|U|/|U_c|$ predicted by the SST-transition model is independent of Re_c as opposed to the laminar model. The mean absolute velocity estimated by the laminar model rises significantly, whereas in the SST-transition model, it rises in proportion to Re_c. Nevertheless, the TVR and k^* are dependent on Re_c, in fact, as Re_c increases, the SST-transition model calculates higher turbulence as much in the channels as in the downstream. Similarly, the TKE rises close to the entrance of the inlet channel as well as at the exit of the outlet channels, however, instability is not perceived in the outlet zone.

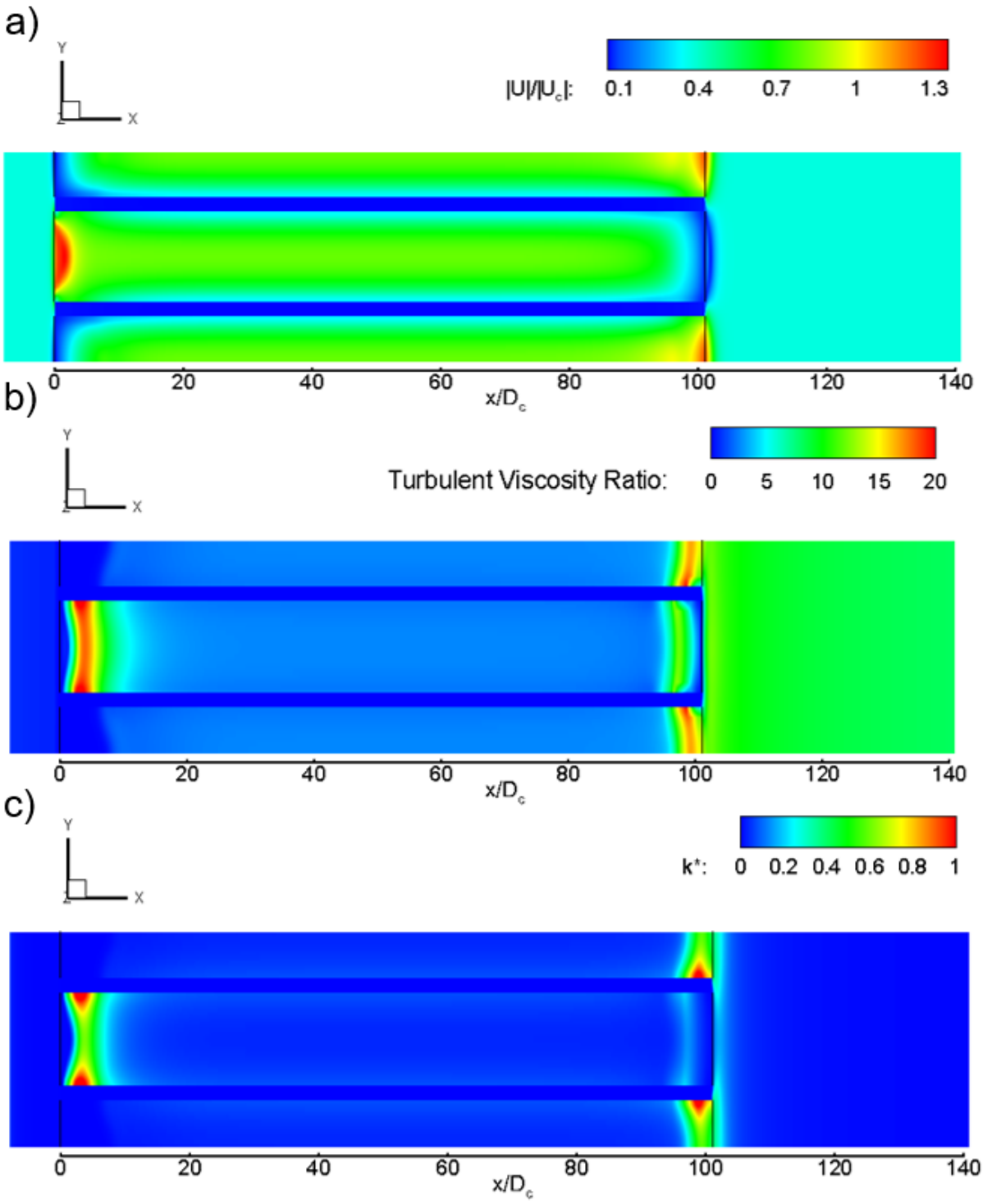

Figure 4.6: Numerical solution using the SST model with Re_c of 232 and TVR=1: a)absolute velocity, b)TVR and c)k^* where k^*=TKE/U_c^2.

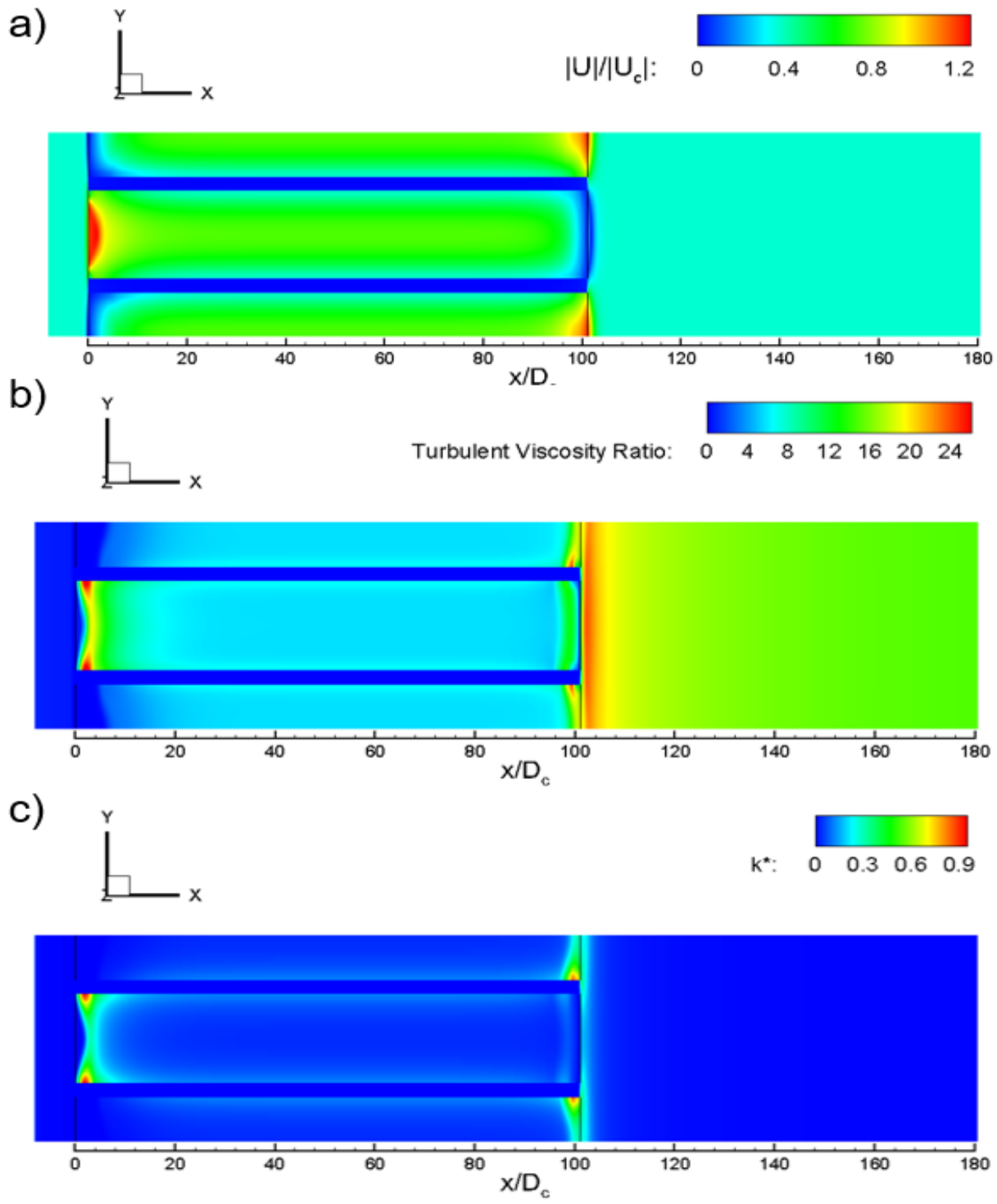

Figure 4.7: Numerical solution using the SST model with Re_c of 463 and TVR=1: a)absolute velocity, b)TVR and c)k^* where k^*=TKE/U_c^2.

The previous results were solved using TVR as a boundary condition equal to one. To simulate possible eddies at the upstream face, TVR was increased to 10. Figure 4.8 shows that TVR, as an inflow condition, does not affect pressure drop predicted by the SST-transition model and therefore, the analysis proceeded with numerical solutions using inlet TVR set as one. Figures 4.9, 4.10, 4.11 and 4.12 illustrate that the addition of expansion and contraction effects make a difference when using the laminar model, however, when using the SST-transition, it does not significantly modify what happens inside the substrate. Moreover, using the experimental data from Chapter 3, Figures 4.13 and 4.14 demonstrate that despite the laminar model predicting different mean velocities when using short or large domain, the contraction and expansion effects do not greatly impact numerical pressure drop. Therefore, a short domain (absence of contraction and expansion losses) is more likely to be used as the reduction of computational resources and convergence difficulties. Nonetheless, since the SST-transition model predicts turbulence in the downstream and as Re_c increases, the expansion effect becomes important, however, this section could be studied separately as Cornejo et al. (2018b) does.

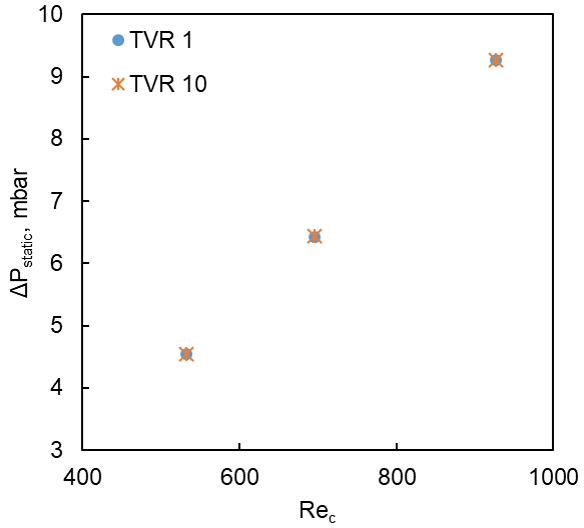

Figure 4.8: Absolute static pressure drop (long domain) using the SST-transition model with different TVRs.

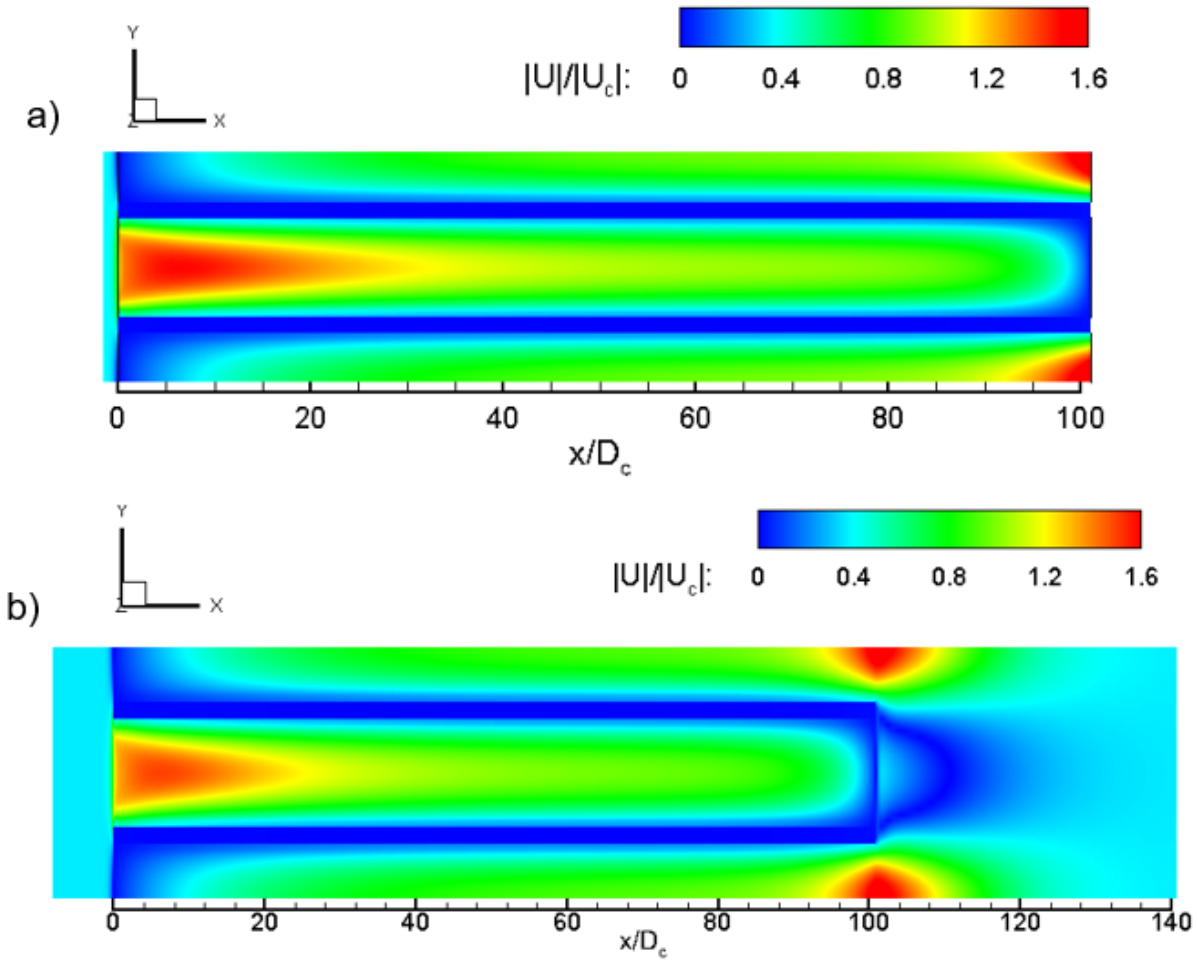

Figure 4.9: Absolute velocity estimated by the laminar model with Re_c of 232 and TVR=1: a)short domain and b)long domain.

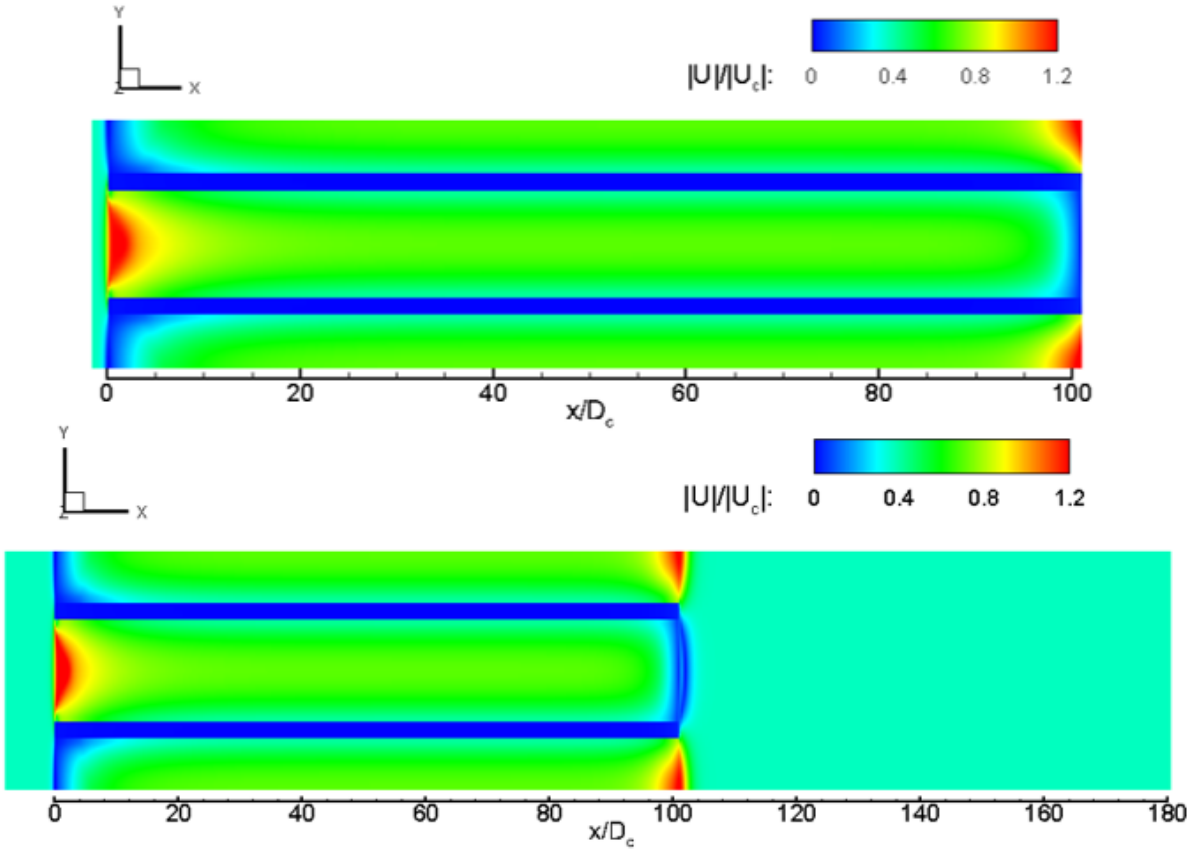

Figure 4.10: Absolute velocity estimated by the SST-transition model with Re_c of 695 and TVR=1: a)short domain and b)long domain.

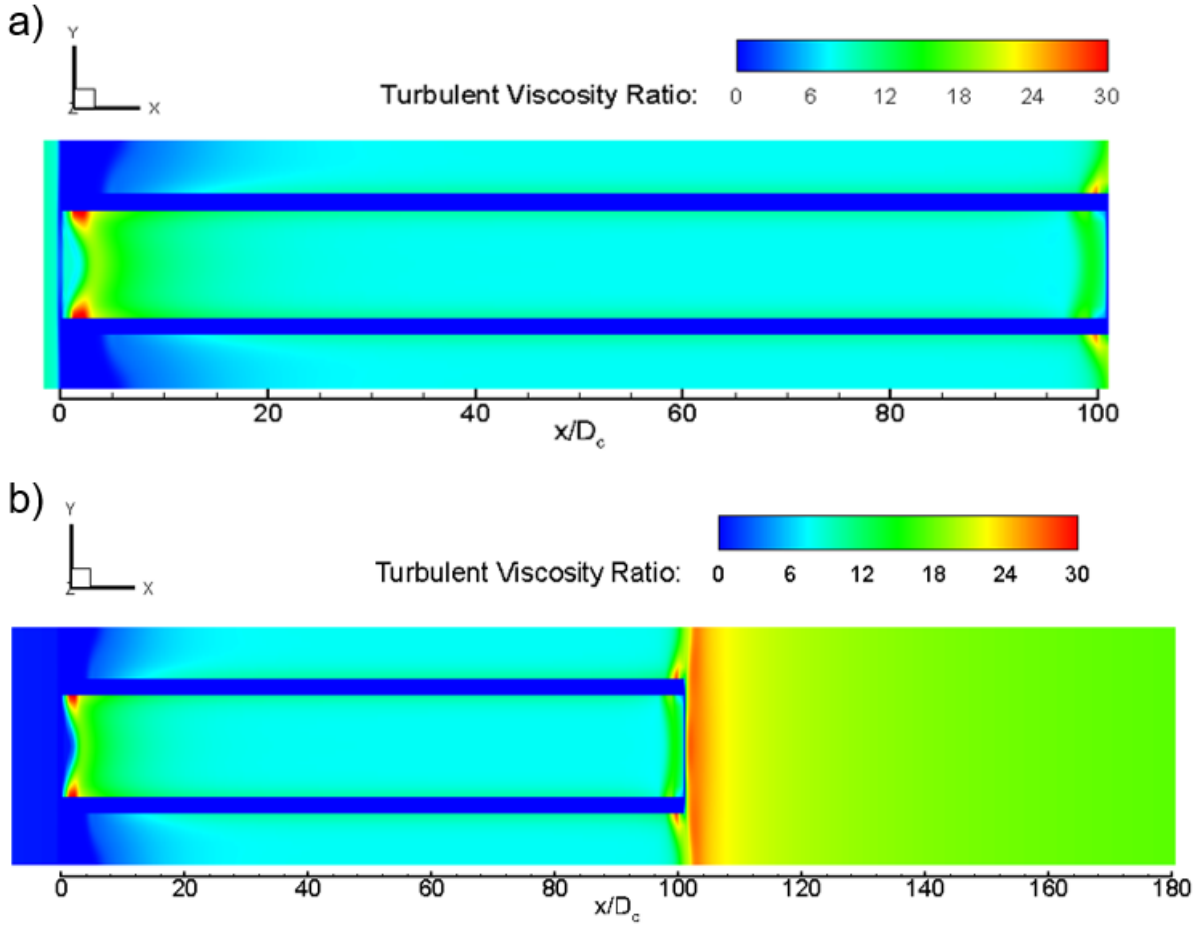

Figure 4.11: TVR estimated by the SST-transition model with Re_c of 695 and TVR=1: a)short domain and b)long domain.

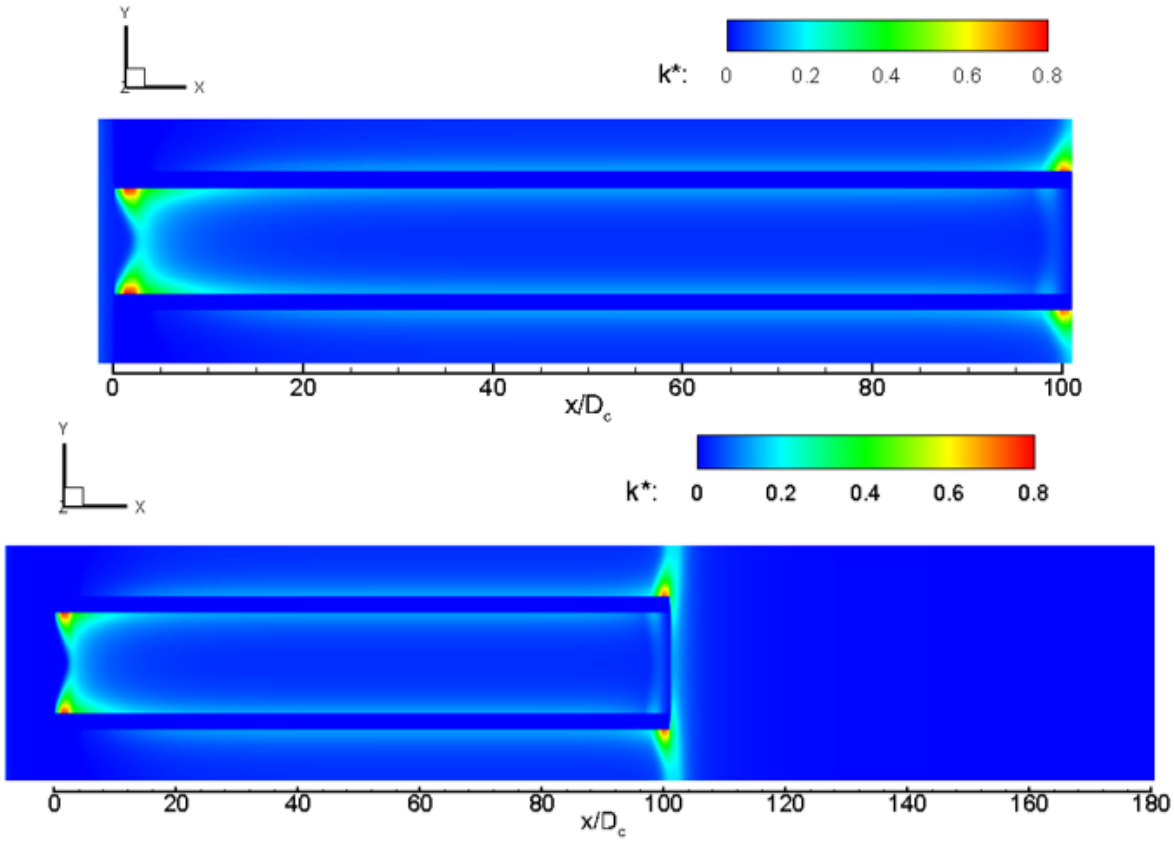

Figure 4.12: k* estimated by the SST-transition model with Re_c of 695 and TVR=1: a)short domain and b)long domain (k*=TKE/U_c^2).

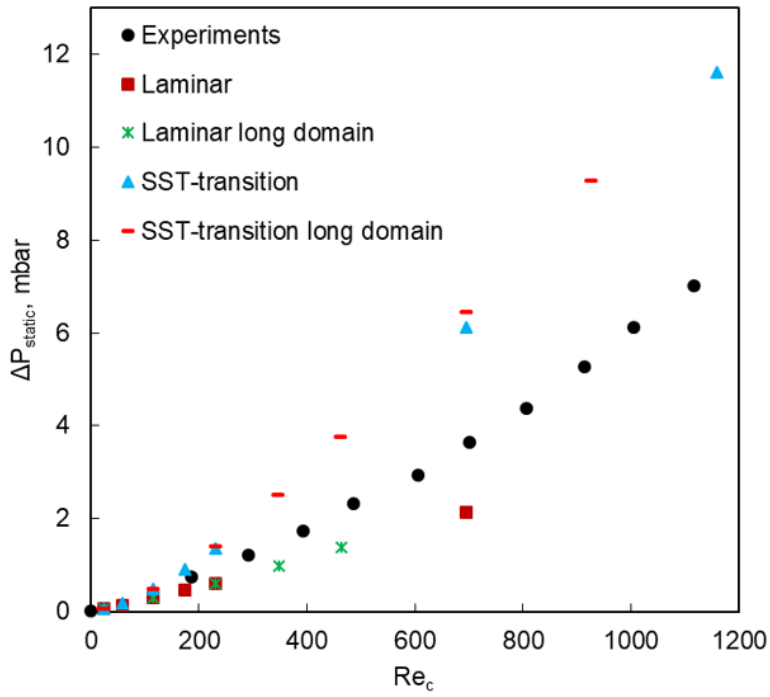

Figure 4.13: Absolute static pressure drop using the large domain and short domain.

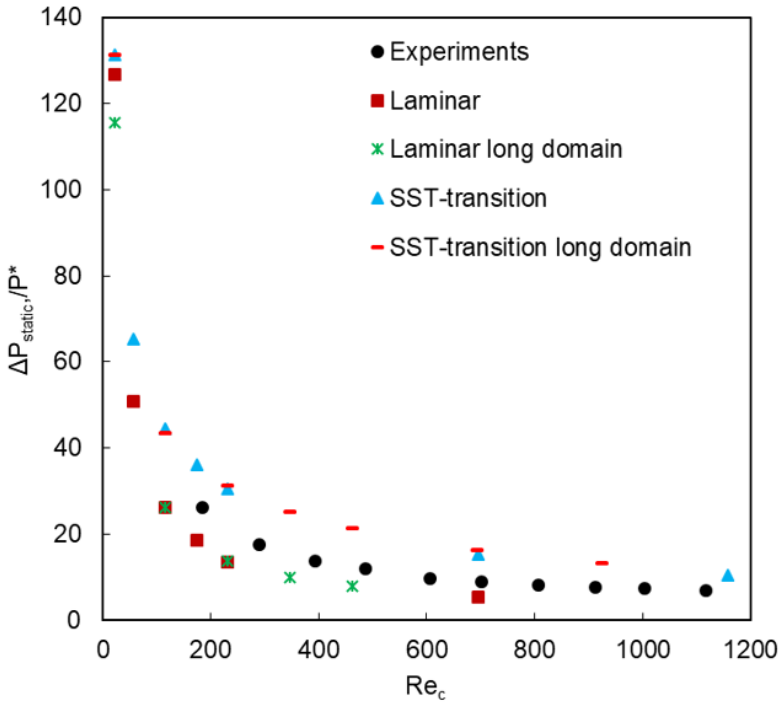

Figure 4.14: Static pressure drop using large domain and short domain, where $P^* = \frac{1}{2}U_c^2\rho$.

Conclusions

Flow behaviour in a GPF was analyzed using computational fluid dynamics in a representative element that consisted of one inlet channel surrounded by outlet channels. The investigation was carried out adopting both, two-dimensional (2D) and three-dimensional (3D) geometries, where a uniform grid resulted to be the most accurate in analyzing flow behaviour along the monolith. The study was completed applying different viscous models such as laminar, k-ε, k-ω and the SST-transition. Furthermore, numerical pressure drop solutions were compared with experimental data to determine whether or not laminar assumption in the study of automotive particulate filters is accurate.

Accuracy increases when using a 3D rather than a 2D geometry, albeit at the expense of computational costs. The analysis in 2D demonstrated that the k-ω model does not appear to describe the flow within a GPF monolith, while in a 3D domain, the k-ω model did not converge due to its inaccuracy when predicting near porous walls. Furthermore, absolute velocity profiles in 2D predicted by laminar, k-ε and the SST-transition was significantly different from 3D. For instance, in 2D, when $\mathrm{Re}_c \geq 220$ the absolute velocity profile was almost linear, while in the 3D, most flow crossed at the end of the filter. Therefore, assuming constant velocity in the porous wall may not be accurate. In addition, as Re_c increases, the mean absolute velocity estimated by the laminar model also significantly rises in both geometries. In contrast, in k-ε and SST-transition models, the mean absolute velocity rises in proportion to Re_c.

In regards to turbulence, both, k-ε and SST-transition models behaved similarly in 2D

and in 3D. Nevertheless, when $Re_c \geq 2000$, the gap between these two models, increased in 3D. Moreover, the SST-transition model showed turbulence at the end of the inlet channel in both dimensions, while the k-ε exhibited only in 3D for $Re_c \geq 2317$. This occurrence may be due to a possible adverse pressure provoked by the flow hitting the plug at the end of the inlet channel. Furthermore, in 2D both k-ε and SST-transition models only demonstrated unsteadiness at the beginning of the inlet channel. However, in 3D this unsteadiness is also observed at the exit of the outlet channels.

Generally, the SST-transition model predicted higher turbulence and turbulent kinetic energy within the monolith than the k-ε model. Although, both models demonstrated the presence of turbulence for $Re_c \geq 220$ in both dimensions. Nonetheless, the previous comparison between 2D and 3D cannot lead to definitive conclusions since the parameters that were applied to both cases differ. Therefore, the impact of channel dimensions (length and height) as well as the permeability in flow behavior through the substrate is questionable.

Furthermore, numerical static pressure drop deviated considerably from the experimental data for $Re_c \geq 300$. The addition of an inlet zone affected flow pattern only when using the laminar model. Nevertheless, the addition of the outlet zone impacted the SST-transition model because as Re_c increases, so does the turbulence in the outlet zone, which may affect pressure drop. The integration of an inlet and outlet zone increased the need for computer resources as well as increasing the difficulty in obtaining a converged solution, however, these modifications did not resulted in significant effects on numerical pressure drop. This analysis indicated that laminar flow may not be the best assumption to study a GPF due to the possible development of transition or turbulent flow within the monolith. Although, as different flow regimes are present, false solutions may have been obtained.

Further investigation is necessary to completely understand flow pattern within a gasoline particulate filter. It should be noted that this work is limited to the use of only a few RANS models, however, others may also be applied. Moreover, large eddy simulations are suggested to validate the existence of turbulence inside the channels. Furthermore, it is also

important to comprehend the effect of temperature on flow trajectory, since a gasoline particulate filter operates at high temperatures. Additionally, as soot cake builds, permeability changes within the monolith, therefore a flow behavior analysis with varying permeability is suggested. Finally, a comparison between 2D and 3D domains, using the same parameters and conditions, should be compared to analyze any differentiation.

Bibliography

Acton, Q. (2013). *Nitrogen Oxides—Advances in Research and Application: 2013 Edition*. ScholarlyEditions.

Alkemade, U. G. and Schumann, B. (2006). Engines and exhaust after treatment systems for future automotive applications. *Solid State Ionics*, 177(26-32):2291–2296.

Anderson, J. D., Degrez, G., Dick, E., and Grundmann, R. (2013). *Computational fluid dynamics: an introduction*. Springer Science & Business Media.

Ansys, A. F. (2017). 18.2 Theory Guide. *ANSYS inc*, 390:1.

Arato, K. and Takashima, T. (2015). A Study on Reduction of Heat Loss by Optimizing Combustion Chamber Shape. *SAE International Journal of Engines*, 8(2015-01-0786):596–608.

Barone, T. L., Storey, J. M., Youngquist, A. D., and Szybist, J. P. (2012). An analysis of direct-injection spark-ignition (DISI) soot morphology. *Atmospheric Environment*, 49:268–274.

Bearman, P. and Trueman, D. (1972). An investigation of the flow around rectangular cylinders. *The Aeronautical Quarterly*, 23(3):229–237.

Beavers, G., Sparrow, E., and Masha, B. (1974). Boundary condition at a porous surface which bounds a fluid flow. *AIChE Journal*, 20(3):596–597.

Beavers, G. S. and Joseph, D. D. (1967). Boundary conditions at a naturally permeable wall. *Journal of Fluid Mechanics*, 30(1):197–207.

Beavers, G. S., Sparrow, E. M., and Magnuson, R. A. (1970). Experiments on coupled parallel flows in a channel and a bounding porous medium. *Journal of Basic Engineering*, 92(4):843–848.

Bensaid, S., Marchisio, D., Fino, D., Saracco, G., and Specchia, V. (2009). Modelling of diesel particulate filtration in wall-flow traps. *Chemical Engineering Journal*, 154(1-3):211–218.

Blazek, J. (2015). *Computational fluid dynamics: principles and applications*. Butterworth-Heinemann.

Carotenuto, C. and Minale, M. (2011). Shear flow over a porous layer: Velocity in the real proximity of the interface via rheological tests. *Physics of Fluids*, 23(6):063101.

Cornejo, I., Nikrityuk, P., and Hayes, R. E. (2018a). Multiscale RANS-based modeling of the turbulence decay inside of an automotive catalytic converter. *Chemical Engineering Science*, 175:377–386.

Cornejo, I., Nikrityuk, P., and Hayes, R. E. (2018b). Turbulence generation after a monolith in automotive catalytic converters. *Chemical Engineering Science*, 187:107–116.

Della Torre, A., Montenegro, G., Onorati, A., and Tabor, G. (2015). CFD characterization of pressure drop and heat transfer inside porous substrates. *Energy Procedia*, 81:836–845.

Deng, Y., Zheng, W., Jiaqiang, E., Zhang, B., Zhao, X., Zuo, Q., Zhang, Z., and Han, D. (2017). Influence of geometric characteristics of a diesel particulate filter on its behavior in equilibrium state. *Applied Thermal Engineering*, 123:61–73.

Deuschle, T., Janoske, U., and Piesche, M. (2008). A CFD-model describing filtration, regeneration and deposit rearrangement effects in gas filter systems. *Chemical Engineering Journal*, 135(1-2):49–55.

Di Sarli, V. and Di Benedetto, A. (2015). Modeling and simulation of soot combustion dynamics in a catalytic diesel particulate filter. *Chemical Engineering Science*, 137:69–78.

Ekambara, K., Dhotre, M. T., and Joshi, J. B. (2005). CFD simulations of bubble column reactors: 1D, 2D and 3D approach. *Chemical Engineering Science*, 60(23):6733–6746.

Fail, R., Eyre, R., and Lawford, J. (1959). *Low-speed experiments on the wake characteristics of flat plates normal to an air stream*. HM Stationery Office.

Feng, Z., Long, Z., and Chen, Q. (2014). Assessment of various CFD models for predicting airflow and pressure drop through pleated filter system. *Building and Environment*, 75:132–141.

Ferziger, J. H. and Peric, M. (2012). *Computational methods for fluid dynamics*. Springer Science & Business Media.

Genc, M. S., Karasu, I., Açıkel, H. H., and Akpolat, M. T. (2012). Low Reynolds number flows and transition. In *Low Reynolds number aerodynamics and transition*. Intechopen.

Gong, J., Viswanathan, S., Rothamer, D. A., Foster, D. E., and Rutland, C. J. (2017). Dynamic heterogeneous multiscale filtration model: probing micro-and macroscopic filtration characteristics of gasoline particulate filters. *Environmental Science & Technology*, 51(19):11196–11204.

Guan, B., Zhan, R., Lin, H., and Huang, Z. (2015). Review of the state-of-the-art of exhaust particulate filter technology in internal combustion engines. *Journal of Environmental Management*, 154:225–258.

Guarnieri, M. and Balmes, J. R. (2014). Outdoor air pollution and asthma. *The Lancet*, 383(9928):1581–1592.

Guo, Z. and Zhang, Z. (2006). Multi-dimensional modeling and simulation of wall-flow diesel particulate filter during loading and regeneration. Technical report, SAE Technical Paper.

Gupta, H. N. (2012). *Fundamentals of internal combustion engines*. PHI Learning Pvt. Ltd.

Haralampous, O., Kandylas, I., Koltsakis, G., and Samaras, Z. (2004). Diesel particulate filter pressure drop part 1: Modelling and experimental validation. *International Journal of Engine Research*, 5(2):149–162.

Haralampous, O. C., Koltsakis, G. C., and Samaras, Z. C. (2003). Partial regenerations in diesel particulate filters. Technical report, SAE Technical paper.

Hoffman, J. D. and Frankel, S. (2001). *Numerical methods for engineers and scientists*. CRC press.

Hua, X., Liu, J., Herrin, D., and Elnady, T. (2011). Numerical simulation of diesel particulate filters in exhaust systems. Technical report, SAE Technical Paper.

Ibrahim, M. and Hashim, W. (1994). Oscillating flow in channels with a sudden change in cross section. *Computers & Fluids*, 23(1):211–224.

James, A. (1994). *Introduction to fluid mechanics*. Cambridge: MIT Press, MA.

Johnson, T. and Joshi, A. (2018). Review of vehicle engine efficiency and emissions. *SAE International Journal of Engines*, 11(2018-01-0329).

Karjalainen, P., Pirjola, L., Heikkilä, J., Lähde, T., Tzamkiozis, T., Ntziachristos, L., Keskinen, J., and Rönkkö, T. (2014). Exhaust particles of modern gasoline vehicles: A laboratory and an on-road study. *Atmospheric Environment*, 97:262–270.

Kattouah, P., Kato, K., Thier, D., Ohara, E., Vogt, C., Ito, Y., Aoki, T., Shimoda, T., Shibagaki, Y., Yuuki, K., et al. (2013). Latest Particulate Filter Technology to reduce Particle Emissions from Gasoline Engines. In *Zurich: ETH Conference on Combustion Generated Nanoparticles*.

Koltsakis, G., Haralampous, O., Depcik, C., and Ragone, J. C. (2013). Catalyzed diesel particulate filter modeling. *Reviews in Chemical Engineering*, 29(1):1–61.

Konstandopoulos, A., Kostoglou, M., Lorentzou, S., and Vlachos, N. (2012). Aspects of multifunctional diesel particulate filters and their efficient simulation. *Catalysis Today*, 188(1):2–13.

Konstandopoulos, A., Kostoglou, M., and Vlachos, N. (2006). The multiscale nature of diesel particulate filter simulation. *International Journal of Vehicle Design*, 41(1-4):256–284.

Konstandopoulos, A. G., Kostoglou, M., Vlachos, N., and Kladopoulou, E. (2005). Progress in diesel particulate filter simulation. Technical report, SAE Technical paper.

Konstandopoulos, A. G., Skaperdas, E., and Masoudi, M. (2001). Inertial contributions to the pressure drop of diesel particulate filters. Technical report, SAE Technical Paper.

Landau, L. and Lifshitz, E. (1987). Theoretical Physics, vol. 6, Fluid Mechanics.

Lee, H. and Lee, K. O. (2013). Development of a 3-D model for analyzing the effects of channel geometry on filtration characteristics in particulate filter system. Technical report, SAE Technical Paper.

Ling, S. H. and van Eeden, S. F. (2009). Particulate matter air pollution exposure: role in the development and exacerbation of chronic obstructive pulmonary disease. *International Journal of Chronic Obstructive Pulmonary Disease*, 4:233.

Lodefier, K., Merci, B., De Langhe, C., and Dick, E. (2003). Transition modelling with the SST turbulence model and an intermittency transport equation. In *ASME Turbo Expo 2003, collocated with the 2003 International Joint Power Generation Conference*, pages 771–777. American Society of Mechanical Engineers.

Lundgren, T., Sparrow, E., and Starr, J. (1964). Pressure drop due to the entrance region in ducts of arbitrary cross section. *Journal of Basic Engineering*, 86(3):620–626.

Mamakos, A., Martini, G., Dilara, P., and Drossinos, Y. (2011). Feasibility of introducing

particulate filters on gasoline direct injection vehicles. *A Cost Benefit Analysis. European Commission Joint Research Center*.

Mamakos, A., Martini, G., Marotta, A., and Manfredi, U. (2013a). Assessment of different technical options in reducing particle emissions from gasoline direct injection vehicles. *Journal of Aerosol Science*, 63:115–125.

Mamakos, A., Steininger, N., Martini, G., Dilara, P., and Drossinos, Y. (2013b). Cost effectiveness of particulate filter installation on Direct Injection Gasoline vehicles. *Atmospheric Environment*, 77:16–23.

Matte-Deschênes, G., Vidal, D., Bertrand, F., and Hayes, R. E. (2016). Numerical investigation of the impact of thermophoresis on the capture efficiency of diesel particulate filters. *The Canadian Journal of Chemical Engineering*, 94(2):291–303.

Menter, F. (1993). Zonal two equation kw turbulence models for aerodynamic flows. In *23rd fluid dynamics, plasmadynamics, and lasers conference*, page 2906.

Menter, F., Langtry, R., and Völker, S. (2006a). Transition modelling for general purpose CFD codes. *Flow, Turbulence and Combustion*, 77(1-4):277–303.

Menter, F. R., Kuntz, M., and Langtry, R. (2003). Ten years of industrial experience with the SST turbulence model. *Turbulence, Heat and Mass Transfer*, 4(1):625–632.

Menter, F. R., Langtry, R. B., Likki, S., Suzen, Y., Huang, P., and Völker, S. (2006b). A correlation-based transition model using local variables—part i: model formulation. *Journal of Turbomachinery*, 128(3):413–422.

Menter, F. R., Smirnov, P. E., Liu, T., and Avancha, R. (2015). A one-equation local correlation-based transition model. *Flow, Turbulence and Combustion*, 95(4):583–619.

Mokhri, M., Abdullah, N., Abdullah, S., Kasalong, S., and Mamat, R. (2012). Soot filtration

recent simulation analysis in diesel particulate filter (dpf). *Procedia Engineering*, 41:1750–1755.

Oxarango, L., Schmitz, P., and Quintard, M. (2004). Laminar flow in channels with wall suction or injection: a new model to study multi-channel filtration systems. *Chemical Engineering Science*, 59(5):1039–1051.

Oxarango, L., Schmitz, P., Quintard, M., and Bardon, S. (2003). 3D macroscopic model for fluid flow and soot deposit in wall flow honeycomb dpf. *SAE Transactions*, pages 545–557.

Piscaglia, F., Rutland, C. J., and Foster, D. E. (2005). Development of a CFD model to study the hydrodynamic characteristics and the soot deposition mechanism on the porous wall of a diesel particulate filter. Technical report, SAE Technical Paper.

Ranalli, M., Hossfeld, C., Kaiser, R., Schmidt, S., and Elfinger, G. (2002). Soot loading distribution as a key factor for a reliable DPF system: an innovative development methodology. Technical report, SAE Technical Paper.

Rao, S., Chirkov, V., Dentener, F., Van Dingenen, R., Pachauri, S., Purohit, P., Amann, M., Heyes, C., Kinney, P., Kolp, P., et al. (2012). Environmental modeling and methods for estimation of the global health impacts of air pollution. *Environmental Modeling & Assessment*, 17(6):613–622.

Sbrizzai, F., Faraldi, P., and Soldati, A. (2005). Appraisal of three-dimensional numerical simulation for sub-micron particle deposition in a micro-porous ceramic filter. *Chemical Engineering Science*, 60(23):6551–6563.

Schetz, J. A. and Fuhs, A. E. (1999). *Fundamentals of fluid mechanics*. John Wiley & Sons.

Tabatabaian, M. (2015). *CFD Module*. Stylus Publishing, LLC.

Tennekes, H., Lumley, J. L., Lumley, J., et al. (1972). *A first course in turbulence*. MIT press.

Turner, C., Thornhill, D., McCullough, G., and Patel, S. (2011). Comparison of experimental PIV data and CFD simulations for flow in a diesel particulate filter inlet diffuser. *SAE International Journal of Engines*, 4(1):1556–1570.

Twigg, M. V. (2007). Progress and future challenges in controlling automotive exhaust gas emissions. *Applied Catalysis B: Environmental*, 70(1-4):2–15.

Versteeg, H. and Malalasekera, W. (2007). *An Introduction to Computational Fluid Dynamics: The Finite Volume Method*. Pearson Education Limited.

Wang, H. and Wang, Y. (2007). Flow in microchannels with rough walls: flow pattern and pressure drop. *Journal of Micromechanics and Microengineering*, 17(3):586.

Wilcox, D. (2006). *Turbulence Modeling for CFD*. Number v. 1 in Turbulence Modeling for CFD. DCW Industries.

Yamamoto, K. and Ohori, S. (2013). Simulations on flow and soot deposition in diesel particulate filters. *International Journal of Engine Research*, 14(4):333–340.

Yang, S., Deng, C., Gao, Y., and He, Y. (2016). Diesel particulate filter design simulation: A review. *Advances in Mechanical Engineering*, 8(3):1–14.

Yu, M., Luss, D., and Balakotaiah, V. (2013). Regeneration modes and peak temperatures in a diesel particulate filter. *Chemical Engineering Journal*, 232:541–554.

Zhang, X., Romzek, M., Keck, M., and Kurz, F. (2005). Numerical optimization of flow uniformity inside diesel particular filters. Technical report, SAE Technical Paper.

Zhao, F., Lai, M.-C., and Harrington, D. L. (1999). Automotive spark-ignited direct-injection gasoline engines. *Progress in Energy and Combustion Science*, 25(5):437–562.

Zinola, S., Leblanc, M., Boréave, A., R'Mili, B., Cartoixa, B., Vernoux, P., and Raux, S. (2013). The particulate number emissions from GDI engines: Advanced characterization and reduction through a gasoline particulate filter with membrane technology. *SIA Paper*.